Stony Brook University

OFFICIAL COPY

The official electronic file of this thesis or dissertation is maintained by the University Libraries on behalf of The Graduate School at Stony Brook University.

© All Rights Reserved by Author.

Radiosynthesis and Bioimaging of Antibacterial Agents

A Dissertation Presented

by

Li Liu

to

The Graduate School

in Partial Fulfillment of the

Requirements

for the Degree of

Doctor of Philosophy

in

Chemistry

Stony Brook University

August 2012

Copyright by
Li Liu
2012

Stony Brook University

The Graduate School

Li Liu

We, the dissertation committee for the above candidate for the

Doctor of Philosophy degree, hereby recommend

acceptance of this dissertation.

Peter J. Tonge – Dissertation Advisor
Professor of Chemistry Department

Joanna S. Fowler - Chairperson of Defense
Professor of Chemistry Department

Iwao Ojima – Committee Member of Defense
Professor of Chemistry Department

David J. Schlyer – External Committee Member of Defense
Professor of Biomedical Engineering Department, Stony Brook University

This dissertation is accepted by the Graduate School

Charles Taber
Interim Dean of the Graduate School

Abstract of the Dissertation

Radiosynthesis and Bioimaging of Antibacterial Agents

by

Li Liu

Doctor of Philosophy

in

Chemistry

Stony Brook University

2012

The dose and duration of treatment of antibacterial agents is normally established using plasma pharmacokinetic (PK) data together with information on drug efficacy once treatment has been initiated. Although plasma drug concentration is an important guide for establishing treatment protocols, recent studies indicate that the distribution of antibiotics in tissues is a more critical determinant and predictive factor for their activity. This is because most drugs exert their bactericidal effects at the site of infection rather than in the plasma, and because drug equilibration between plasma and infection site cannot always be achieved

Therefore the tissue distribution of front-line TB drugs, including rifampicin (RIF), isoniazid (INH) and pyrazinamide (PZA), and enoyl-ACP reductase (FabI) inhibitors, PT-70 and PT-119, have been studied in healthy animals using PET and radiolabeled drugs. We find that their accumulations are consistent with the mechanism of excretion of each

drug. In addition, we also find that the ability of the drugs to penetrate the blood-brain barrier decreases in the order PZA > INH > RIF. Estimated concentrations of RIF, INH and PZA in the lungs are at least 10, 10 and 1-3 times higher, respectively, than the minimum inhibitory concentration (MIC) values for these drugs against *Mycobacterium tuberculosis* (Mtb). Estimates of drug concentrations in the brain suggest that the concentrations of RIF and INH are 3-4 and >10 times higher than their MIC values, while the concentration of PZA is similar to or slightly higher than its MIC values.

It is also estimated that the ability of PT-70 and their radiolabeled metabolites to penetrate the blood-brain barrier is similar to INH, while the ability of PT-119 is two times higher than INH. In addition, estimated $AUC_{0\text{-}90min}$/MIC values for PT-70 and PT-119 are 38% and 37% of the INH $AUC_{0\text{-}90min}$/MIC, respectively, which suggests that PT-70 and PT-119 have similar potential to treat CNS TB in non-human primates and humans. For pulmonary TB infection, it is estimated that the $AUC_{0\text{-}90min}$/MIC values for PT-70 and PT-119 are 51% and 14%, respectively, of the INH $AUC_{0\text{-}90min}$/MIC, which suggests that PT-70 is a better candidate than PT-119. For *S. aureus* infection, PT-119 demonstrates 10 times higher $AUC_{0\text{-}90min}$/MIC value than that for PT-70 in the brain, and it is clear that PT-119 is a superior candidate for the treatment of *S. aureus* meningitis, although both $AUC_{0\text{-}90min}$/MIC values are higher than calculated CSF $AUC_{0\text{-}90min}$/MIC of a commonly prescribed antibiotic, Vancomycin.. The estimated concentrations in heart and kidney are at least 20 times higher for PT-70 and 100 times higher for PT-119 than the MIC values against *S. aureus*. The $AUC_{0\text{-}90min}$/MIC for PT-119 is 16368 min and 51023 min for heart and kidney respectively, and both are ~3 times higher than the values for PT-70. The result suggested PT-119 is better candidate than PT-70 to treatment *S. aureus* infection in the heart and kidney.

Finally, studies of radiolabeled antibacterial agents have been extended to Mtb and *S. aureus* infected animals to evaluate their abilities to localize bacteria. 2-[^{18}F]F-INH has been imaged in Mtb infected mice in comparison with uninfected mice, and we have observed minor amplitude of signal (1:6:1 = infected : uninfected) at 1 hr post injection, although it may be partially contributing to a nonspecific inflammatory effect. [^{18}F]FDG has been utilized to image *S. aureus* infection in systemic infected mice, and a 2.5:1 signal has been observed within spleen, which is consistent with highest level of bacteria population. These studies will help us to validate novel diagnostics for infectious disease

Table of Contents

List of Figures

List of Tables

List of Schemes

List of Abbreviations

%ID/cc	% of injected dose per cubic centimeter
2-F-INH	2-Fluoro-isonicotinic acid hydrazide
AcOH	Acetic acid
ACP	Acyl carrier protein
AUC	Area under the curve
BBB	Blood-brain barrier
calcd	Calculated
CFU	Colony-forming unit
ClogD	Calculated logarithm of distribution coefficient
CNS TB	Central nervous system TB
CoA	Coenzyme A
CSF	Cerebrospinal fluid
CT	Computerized tomography
DCY	Decay-corrected yield
DD-CoA	*Trans*-2-Dodecenoyl-CoA
DMF	dimethylformaide
DMSO	Dimethyl sulfoxide
DNA	Deoxyribonucleic acid
E. coli	*Escherichia coli*
ECF	Extracellular fluid
ecFabI	Enoyl-ACP reductase from *Escherichia coli*
EMB	Ethambutol

EMEA	European Medicines Evaluation Agency
ESI	Electrospray ionization
EtOH	Ethanol
F. tularensis	*Francisella tularensis*
FabI	Enoyl-ACP reductase
FAS-II	Type II fatty acid biosynthesis
FDA	Food and Drug Administration
FDG	2- [^{18}F]-Fluorodeoxy-D-glucose
HCl	Hydrochloric acid
HIV	Human immunodeficiency virus
HNPs	Human neutrophils
HPLC	High-performance liquid chromatography
HTS	High-throughput screening
IC50	The half maximal inhibitory concentration
INH	Isoniazid
InhA	Enoyl-ACP reductase from *Mycobacterium tuberculosis*
KatG	Mycobacterial catalase-peroxidase
KOH	Potassium hydroxide
LB	Luria Broth
logD	Logarithm of distribution coefficient between *n*-octanol and water
MD	Microdialysis
MDR-TB	Multidrug-resistant TB
MeOH	Methanol

MH	Muller-Hilton
MHz	Megahertz
MIC	Minimal Inhibitory Concentration
MRI	magnetic resonance imaging
MRS	magnetic resonance spectroscopy
MRSA	Methicillin-resistant *Staphylococcus aureus*
MS	Mass spectrum
Mtb	*Mycobacterium tuberculosis*
NAD^+	Nicotinamide adenine dinucleotide (oxidized form)
NADH	Nicotinamide adenine dinucleotide (reduced form)
NaOH	Sodium hydroxide
NMR	Nuclear magnetic resonance
PCR	Polymerase chain reaction
PET	Positron Emission Tomography
PK	pharmacokinetic
PPB	Plasma protein binding
PZA	Pyrazinamide
R&D	Research and development
RIF	Rifampicin
Rt or RT	Room temperature
S. aureus	*Staphylococcus aureus*
saFabI	Enoyl-ACP reductase from *S. aureus*
SAR	Structure-activity relationship

TAC	Time-activity curve
TCC	Time-concentration curve
THF	Tetrahydrofuran
TK	thymidine kinase
UBI	ubiquicidin
VRSA	vancomycin-resistant *S. aureus*
WHO	World Health Organization
wt	Wild type
XDR-TB	Extensively drug-resistant tuberculosis

Acknowledgments

I would like express my deepest gratitude to my advisor, Prof. Peter J. Tonge, for his constant encouragement and guidance that have led me to overcome most challenging obstacles. He has not only provided support on my research but also helped me to pursue personal interest. Without him, it would not been possible to write this dissertation.

I would also like to thank Prof. Joanna S. Fowler, the chairperson of my dissertation committee, for her kind support, thoughtful criticism and valuable suggestions. I am grateful to Prof. Iwao Ojima, the third member of my dissertation committee, for teaching organic chemistry course and supporting my job search. It is my great pleasure to thank Prof. David J. Schlyer, the outside member of my committee, for his intelligent advice and kind help. I own sincere and earnest thankfulness to Prof. Jacob M. Hooker for his hands on mentorship and career guidance.

I would like to thank my friends in Tonge Group who shared joy and sorrow with me. I will cherish those moments in my whole life. I would also like to thank my friends and colleagues in Fowler Group who constantly provide help with my research.

I would like to thank my parents for supporting me and motivating me through my life. I am proud of being your son.

Finally, and most importantly, I would like to thank my wife Ziqi Gao. Her unwavering love was undeniably the bedrock upon which my study in United States has been built.

List of Publications

- **Liu, L.**; Xu, Y.; Shea, C.; Fowler, J.S.; Hooker, J.M. and Tonge, P.J. "Radiosynthesis and Bioimaging of the Tuberculosis Chemotherapeutics Isoniazid, Rifampicin and Pyrazinamide in Baboons." *J. Med. Chem.* **2010**, *53*, 2882-91
- **Liu, L**.; Kim, SW.; Fowler, J.S.; Hooker, J.M. and Tonge, P.J. "Radiosynthesis and Bioimaging of the Enoyl-ACP Reductase Inhibitors in Baboons." Manuscript in preparation
- Weinstein, E.A.* and **Liu, L.***; Ordonez, A.A.; Wang, H.; Hooker, J.M., Tonge, P.J. and Jain, S.K. "Noninvasive Determination of 2-[^{18}F]-Fluoroisonicotinic acid hydrazide Pharmacokinetics by Positron Emission Tomography in *Mycobacterium tuberculosis* Infected Mice." *Antimicrob. Agents Chemother*. Manuscript Submitted

.

Chapter 1

Introduction: Antibiotic Discovery, Infectious Disease Diagnosis, and Positron Emission Tomography

Antibiotic Discovery

The History of Antibiotics

In 1908, the first synthetic antibiotic, Salvarsan, was discovered by Paul Ehrlich, who screened hundreds of organic arsenical compounds against various organisms and found that Salvarsan was active against syphilis[1]. Twenty years later, Alexander Fleming observed the antibiotic property of the mold *Penicillium notatum* against *Staphylococcus aureus* (*S. aureus*), although it wasn't until 1942 that the manufacturing process for Penicillin was invented by Howard Florey and Ernst Chain[2]. In the meanwhile, German chemist, Gerhard Domagk, discovered the first sulfonamide antibiotics, Prontosil, and invented the manufacturing procedure[1]. These pioneers led to a discovery of over ten antibiotics between 1945 and 1960, which has later been called the "golden era" of antibiotic discovery (**Figure 1.1**)[3].

Following this "golden era", extensive medicinal chemistry efforts were undertaken in order to improve the pharmacological properties of the known scaffolds and to circumvent antibiotic resistance. In addition, the pace of the discovery of new classes of antibiotics has dramatically slowed down since 1960s. While the focus has shifted to modification of existing antibiotics, stricter regulations together with competition from generic drugs has hindered the discovery of new antibiotics. However, due to the emergence of antibiotic resistance, there is a pressing need to develop new classes of antibiotics[3]. For instance, the World Health Organization (WHO) estimates that about 650,000 cases of multi-drug resistant TB (MDR-TB) are present in the world in 2010, in which 9% of these cases are extremely drug-resistant TB (XDR-TB) and 150,000 people die due to MDR-TB annually[4].

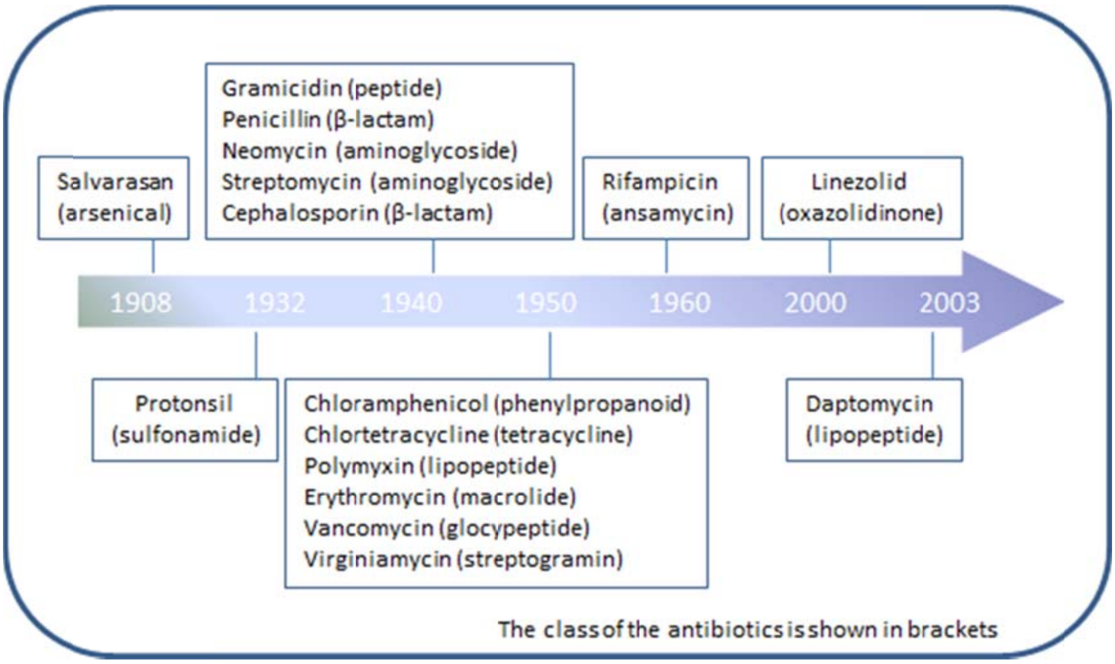

Figure 1.1 The history of antibiotic discovery. This figure is adapted from[3]

Current Antibiotic Discovery

Current antibiotic discovery is similar to general drug discovery. Typically, it involves the following steps: molecular target identification and validation, target-to-hit, hit-to-lead, lead optimization, preclinical, clinical and submission to launch. The process starts with exploration and identification of molecular targets. Normally a knockout or knockdown of a specific molecular target is performed to confirm essentiality. Once the molecular target is validated, a high-throughput screen (HTS) is conducted to identify a series of hit compounds. After a hit is confirmed as a lead, the next challenge is to optimize the lead by medicinal chemist to improve *in vitro* activity. The optimized lead is tested extensively to determine if the new antibiotic is safe and effective for evaluation in humans, which is followed by clinical trials and, finally, FDA approval (**Figure 1.2**)[5].

Figure 1.2 Times and successful rate of drug discovery. This figure is adapted from[5].

*P: the probability of successful transition from one stage to the next

**Parameters for overall process

Over the past few decades, government agencies, academic institutions and pharmaceutical companies have invested a great amount of capital into antibacterial research and development (R&D), and scientific and technology inputs have been advanced significantly. For example, identification of new drug targets has been aided by billion times faster DNA sequencing since the first genome sequence was determined in the 1970s. In addition, HTS facilitates the hit identification and is more than tenfold cost effective than in the mid-1990s. However, R&D productivity, measured by new antibiotics brought to market, has declined[6].

Antibiotic Concentration at Site of Infection

One possible reason for the decline in R&D productivity is poor estimation of drug concentration at the site of infection. During the preclinical and clinical stages of antibiotic discovery, the dose and duration of treatment is normally established using plasma pharmacokinetic (PK) data together with information on drug efficacy once treatment has been initiated. Although plasma drug concentration is an important guide for establishing treatment protocols, recent studies suggest that the distribution of antibiotics in tissue is a more critical determinant and predictive factor for their activities[7,8]. In addition, failure to reach optimal drug concentration at the site of infection may result in therapeutic failure and trigger bacterial resistance. Finally, regulation agencies, such as Food and Drug Administration (FDA) in the United States and European Medicines Evaluation Agency (EMEA) in Europe, require measurement of the distribution of antibiotics at uninfected and infected sites[8]. Thus there is a pressing need to have a technique to measure the drug concentration at the site of infection.

Measurement of Drug Concentration at the Site of Infection

Over the past few decades, several techniques have been developed to understand the tissue distribution of drugs. These approaches can be divided into invasive methods and non-invasive methods, while invasive methods can be further divided into direct and indirect methods.

Invasive Methods

Indirect method measures antibiotic concentration in the plasma and uses mathematical algorithms to derive concentration at peripheral compartments. This methodology has been used extensively in current antibiotic discovery and is based on theoretically sound compartments or physiological concepts[9,10]. However, studies have demonstrated that the real body is a multimillion-compartment model, and current technology, which seeks to determine the antibiotic transfer between plasma and tissue with heterogeneous and tissue specific rates, is merely able to account for all those compartments[11]. Thus although parameters such as the volume of distribution can be used to estimate tissue penetration, this refers to the penetration into a hypothetical compartment. Unless there is a rapid, unrestricted and homogeneous diffusion processes in this hypothetical compartment, the mathematical calculation is a poor estimation of antibiotic distribution in tissues[8].

As technology has developed, several direct experimental tools have been employed to circumvent the limitations of the indirect method. These approaches typically involve taking tissue or a fluid sample from a live organism, homogenizing the sample, extracting the antibiotic from the sample and quantifying the antibiotic by Liquid Chromatography-Mass Spectrometry (LC/MS or LC/MS/MS). This method is clearly advantageous in terms of sampling area compared to the indirect method. However, this involves the medical removal of tissue from a live subject performed by a surgeon, which is a more complicated procedure than taking plasma samples. In addition, the data obtained from the homogenized samples is complicated by the fact that the tissue distribution of drugs is not always homogeneous[12]. Finally, the extraction efficiency of drugs from tissue adds an additional complication.

Another innovative direct method is microdialysis (MD), a method that was initially designed for experimental neurophysiology and neurochemistry to measure neurotransmitter concentration in the central nervous system (CNS). The method has been gradually adopted by pharmacologists to measure drug distribution. The principle of MD is the diffusion of drugs across a semipermeable membrane at the tip of the MD probe. The MD probe is implanted into the tissue of interest and the concentration gradient of the drug drives the diffusion of the compound from the tissue into the probe. Samples from the probe are collected and quantified, and used to derive the extracellular fluid (ECF) concentration. To date, MD is the only feasible technique that can continuously monitor drug concentration in virtually any tissue. However, the invasive nature, high technique requirement, and recovery reliability raise limitations on using this technique[13,14].

Non-invasive Methods

Imaging techniques, such as Positron Emission Tomography (PET) and Single Photon Emission Computed Tomography (SPECT), have made significant improvements over the past few decades leading to their use for non-invasive detection of drug behavior and location *in vivo*. Technique likes PET, which images drugs and other molecules labeled with positron-emitting isotopes, provides a method of acquiring quantitative information on the dynamics of drug absorption, distribution, and elimination in a living animal or human. Together with advances in the development of methods for labeling drug molecules and other organic compounds, PET is emerging as a powerful alternative to invasive distribution studies. Indeed, PET can map three-dimensional tissue distribution over time noninvasively and the quantification reliability is as good as direct measurement of tissue samples[15]. In addition, the methodology developed for imaging drug distribution in laboratory animals using PET can be readily translated to humans. Finally, PET is also complementary to clinical MD and magnetic resonance spectroscopy (MRS) in terms of acquiring information on the tissue distribution of different chemical species[8], although the later technique is as sensitive as PET and thus it can only measure higher concentration of drugs.

Diagnosis of Infectious Disease

Diagnosis of infectious disease is as critical as antibiotic discovery, if not more so, in order to personalize treatment of patients[16]. Traditional diagnosis starts with obtaining a medical history and performing a physical exam. In addition, a more detailed diagnosis would include the culture of infectious agents isolated from a patient, typically blood or urine. A series of tests can be performed with patient samples to identify the infectious organism, such as microbial culture, microscopy, biochemical tests and molecular diagnostics. In some cases, when the infection is inside the body, a biopsy is performed after which the sample is tested in a similar way as blood and urine to identify the pathogen[17].

Imaging of Infectious Diseases

Imaging techniques represent a potentially non-invasive diagnostic method for infectious diseases. Over the last few decades, several types of imaging techniques have been developed and implemented for diagnosis. The imaging technique provides timely identification and localization of infection. Computerized tomography (CT), magnetic resonance imaging (MRI), and ultrasonography are powerful non-invasive methods to diagnose infectious disease[18,19]. However, these techniques cannot detect early stage infection as they can only differentiate disease status by anatomical changes, which would not happen at early stage of disease. In addition, a lesion left after the cure of infectious disease has minimal anatomical difference compared to active infection, which makes it difficult for a physician to judge the status of the disease[16].

Molecular Imaging

Molecular imaging is another category of non-invasive technique. It differs from traditional imaging in that it enables the visualization of the cellular function and the molecular process of living organism through a probe. This probe interacts with the molecular target of interest in the living organism and theoretically could identify the localization of infection and quantity bacterial load (**Figure 1.3**)[20].

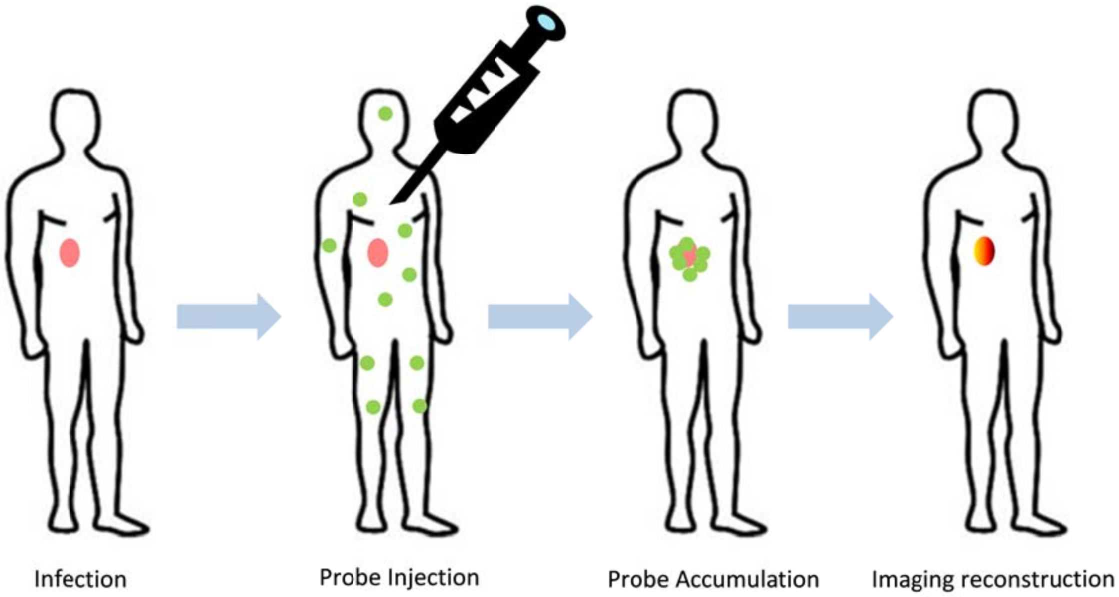

Figure 1.3 Molecular Imaging and Infection Diagnosis. Adopted from Opensource Handbook of Nanoscience and Nanotechnology

Molecular imaging techniques include several modalities, such as optical imaging, PET and SPECT. Optical imaging is the use of fluorescence or bioluminescence. In fluorescence imaging, an external light source is used to excite a fluorophore in the target molecule, and the resulting light emission is captured to reconstruct the image. In contrast, bioluminescence imaging utilizes a luciferase reporter gene as the source of light, which enables gene expression and infection status to be monitored. However, one crucial limitation of optical imaging is the inability of light to penetrate more than a few cm of tissue, which is especially critical when working at visible wavelengths[21]. In addition, fluorescent imaging requires the incorporation of a fluorophore into the drug, which may affect the biological properties of the molecule.

PET and SPECT are conceptually similar to fluorescent imaging. While fluorescent imaging implements a fluorophore, PET and SPECT utilize a radiolabeled probe, which contains a targeting compound and a radionuclide. Decay of the radionuclide is captured by an external detector and used to reconstruct the distribution of the probe. Compared to optical imaging, PET and SPECT have better tissue penetration, resulting in better resolution[21].

Development of PET and SPECT imaging is stimulated by advances in cell biology, the discovery of new targets and by unraveling the molecular pathways that lead to disease[22]. Moreover, these methods have already been identified as powerful techniques to study cancer[20,23-25], CNS diseases[26-30], and cardiovascular disease[31,32]. The use of molecular imaging to study infectious diseases is a relatively new area in comparison with cancer and CNS. Before introducing agents used for imaging infectious diseases, it is necessary to clarify infection and inflammation.

Infection and Inflammation

The definition of inflammation is “the response of tissues to any kind of injury in order to bring serum molecules and cells of the immune system to the site of damage”[16]. Inflammation is triggered by trauma, ischemia or infection[33]. Typical characteristics of inflammatory responses are enhanced blood supply, enhanced vascular permeability, and increased influx of leukocytes[34]. In the meanwhile, leukocytes and plasma proteins are generated as part of the defense mechanism.

Inflammation Probes

Strategies to image infection include targeting the inflammatory response and targeting the bacterium. However, it is worth pointing out that infection does not always generate inflammatory response, such as in the case of immunocompromised subjects[16]. Targeting the inflammatory response can be further categorized as non-specific uptake and specific uptake. The non-specific strategy utilizes increased vascular permeability and blood supply, such as [^{67}Ga]citrate and non-specific immunoglobulins, while the specific strategy involves the use of the influx of leukocytes, such as radiolabeled leukocytes, antigranulocyte monoclonal antibodies and leukocyte receptor-binding ligands[16]. Recently, 2- [^{18}F]-fluorodeoxy-D-glucose (FDG) has demonstrated utility for imaging infections[35,36], and the mechanism is related to leukocytes consuming glucose as energy source[37]. However, probes that target the inflammatory response often cannot be used to differentiate between infection and inflammation.

Infection Specific Probes

Probes such as radiolabeled antibiotics and antibacterial peptides, that are designed to target the infectious organism, are potentially able to distinguish sterile inflammation and infection. In the late 1980s, the first radiolabeled antibiotic was introduced by Dr. Solanki and coworkers[38]. In the next two decades, ciprofloxacin, lemofloxacin, ceftzoxime, isoniazid, fluconazole and other antibiotics have been radiolabeled[21,39]. Among those radiolabeled probes, [^{99m}Tc]ciprofloxacin has been studied most extensively. It is a synthetic broad spectrum fluoroquinolone antibiotic and binds to prokaryotic topoisomerase IV and DNA gyrase in bacteria[40,41]. Clinical applications of this radiotracer have been implemented by Dr. Britton and coworkers, who demonstrated 85.4% sensitivity and 81.7% specificity for detecting infection among 879 patients[42]. However, other studies in animals and patients provide controversial support for these reports with evidence of lower specificity[43]. ^{18}F labeled fleroxacin and trovafloxacin have been used to evaluate infection in animal models[44,45]. These studies determined the biodistribution of antibiotics at the site of infection and proved that PET imaging of radiolabeled antibiotic is a promising tool for determine tissue PK. However, the uptake of the probes at the infection site was not significantly different from control in either case. This unexpected result could partially be explained by low specific activity as the radiolabeled antibiotics are diluted to therapeutic dose by their unlabeled counterparts[44-46]. In addition, the use of the fluorine exchange labeling method provides a "cap" on the upper limit of specific activity of radiolabeled antibiotics as the mass of product is 1,000 times larger than otherwise the same nucleophilic substitution[18].

Several antimicrobial protein peptides were investigated in a similar manner for specific imaging of bacterial infection[47-51]. Human neutrophils (HNPs) were radiolabeled with ^{99m}Tc, and the resulting probe was evaluated in *S. aureus* and *Klebsiella pneumonia* (*K. pneumonia)* infection models. However, the signal ratio between infection and control was low and decreased even further with time[48]. Another antimicrobial peptide, ubiquicidin (UBI), has been investigated as truncated peptides, UBI 29-41(residues 29-41 of ubiquicidin) and UBI 18-35 (residues 18-35 of ubiquicidin). Each of them was radiolabeled with ^{99m}Tc and demonstrated statistical significant accumulation in infection than sterile inflammation[49,50,52].

More recently, another probe, [^{125}I]FIAU, has been used to image bacteria with positive thymidine kinase (TK) activity[53]. The function of TK is to transfer a γ phosphate group from ATP to the 5' hydroxyl group of pyrimidine deoxynucleosides[54]. The probe is a substrate of TK and undergoes a phosphorylation *in vivo*. Phosphorylated [^{125}I]FIAU accumulates within the cell as the free phosphate prohibits the penetration of the plasma membrane[55]. This probe was initially designed to image tumor cells with exogenous herpes virus infections and further adapted to bacterial imaging with endogenous TK[53].

A summary of known probes targeting bacteria are presented in **Table 1.1**.

Table 1.1 Probes for Imaging Bacteria Infection[21]

Probe	Bacterium	Maximum Ratio	Tmax	Isotopes
UBI 29-41	*S. aureus*	2.89	60 min	^{99m}Tc[52]
Ciprofloxacin	*S. Corynebacteria*	5.5	2 h	^{18}F[56]
(infecton)	*S. aureus*	1.7	0 h	^{99m}Tc[57]
Fleroxacin	*E. Coli.*	~1	2h	^{18}F[46]
Trovafloxacin	*E. Coli.*	<1	2h	^{18}F[45]
Ethambutol	Mtb	> 1	n/a	^{99m}Tc[58]
Isoniazid	Mtb	3.5	24 h	^{99m}Tc[59]
FIAU	*S. aureus*	~15	16 h	^{125}I[53]

Obviously, diagnosis of bacterial infections has been brought back into the spotlight and increasing research efforts have been invested in development of new probes for imaging specific molecular events in infection[18,53]. These probes have demonstrated application in early detection of infection, therapy decision making and therapy response access. However, current state of the art probes are not currently able to differentiate strains of bacteria. Theoretically, targeting strain specific enzymes or receptors would enable this differentiation. Even if probes target the same enzyme in different bacteria, altered binding affinity between these homologous proteins could also lead to the ability to differentiate bacterial strains.

Positron Emission Tomography

History of PET

In the late 1950s, two scientists, Drs. David E. Kuhl and Roy Edward, introduced the concept of emission and transmission tomography[60,61]. Based on their contribution, University of Pennsylvania designed and constructed several tomographic instruments[62]. Subsequently, scientists at Washington University carried the development of tomographic technique to the next stage[63,64]. In 1961, the first single-plane PET scanner was built by Dr. James Robertson and his associates at Brookhaven National Laboratory[65].

Besides the advancement in instrumentation, the development of PET was further facilitated by the invention of new radiopharmaceuticals, which led to the acceptance of PET as a diagnostic technique. The single most important tracer that has been developed is [^{18}F]FDG which was synthesized at Brookhaven National Lab under the direction of Dr. Al Wolf and Dr. Joanna Fowler[66]. In 1976, the first human study on [^{18}F]FDG was performed at the University of Pennsylvania with two healthy volunteers and the concentration of [^{18}F]FDG in organs were determined. In the next few decades, significant amount of research and capital have been invested in the development of both instrumentation and radiopharmaceuticals. Together with improvements in image reconstruction, PET has now been established as a sophisticated research and diagnostic tool.

Principles of PET

PET is an advanced medical imaging technique that is used to study and visualize human physiology at the molecular level. The positron emitting radioisotopes, carbon-11, nitrogen-13, and fluorine-18, are the most commonly used elements in PET through their chemical introduction into the molecule of interest (**Table 1.2**).

Table 1.2 The most commonly used short-lived radionuclides in PET[67]

Radionuclide	Half-life (min)	Nuclear reaction	Target	Product	Decay product
^{11}C	20.4	$^{14}N(p,\alpha)^{11}C$	$N_2(+O_2)$	$[^{11}C]CO_2$	^{11}B
			$N_2(+H_2)$	$[^{11}C]CH_4$	
^{13}N	9.97	$^{16}O(p,\alpha)$	H_2O	$[^{13}N]NO_x$	^{13}C
			H_2O+EtOH	$[^{13}N]NH_3$	
^{15}O	2.04	$^{15}N(d,n)^{15}O$	$N_2(+O_2)$	$[^{15}O]O_2$	^{15}N
^{18}F	110	$^{20}Ne(d,a)^{18}F$	$Ne(+F_2)$	$[^{18}F]F_2$	^{18}O
		$^{18}O(p,n)^{18}F$	$[^{18}O]H_2O$	$[^{18}F]F^-$	

After administration of the radiotracer, the PET radionuclide decays by positron emission (**Figure 1.4**). When a positron annihilates with an electron, two 511 keV γ-rays are generated and emitted at 180 degrees to each other[67]. These tissue penetrating γ-rays take a few nanoseconds to reach the detectors. When two detectors are hit within a set timing window by an annihilation photon pair, an electronic pulse is generated at each detector which determines the straight along which the event occurred. However, far more photon pairs are not detected because one or both of the gamma rays are not detected. During a PET scan, the system is counting the number of times each detector pair is hit in coincidence, so the raw data from a PET scan are simply the list of counts obtained along each line of response[68]. With the sophisticated three-dimensional (3D) or two-dimensional (2D) reconstruction algorithms, raw projection data can be converted into high quality images to provide quantitative measures of probe concentration in a subject at spatial resolutions of a few millimeters. In addition, these quantitative measures of probe concentration can be extended to yield more profound measures of PK and PD, as well as the biochemical status of enzymes and receptors.

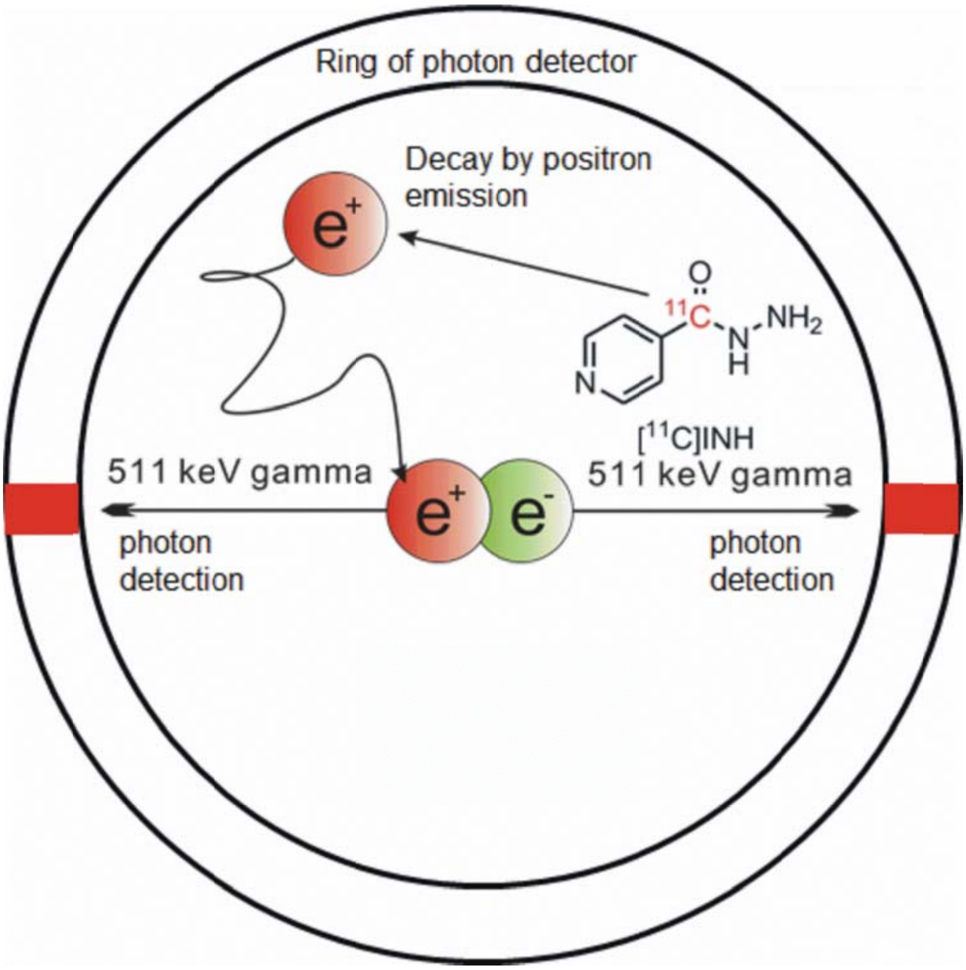

Figure 1.4 Principle of PET. A radiolabeled small molecule [^{11}C]INH decays by positron emission. Annihilation of positron results in two γ-rays, which are detected by photon detector

In summary, four steps are involved in a typical PET study: production of radionuclides, incorporation of radionuclides and purification of probes, quality control, data acquisition and reconstruction. The first two steps will be discussed in detail in the following section.

Production of radionuclides

The positron emitting radionuclides are produced during irradiation of the appropriate target and converted to synthetic precursors, either in the target or immediately after exiting the target. The number and type of products that are generated in a target are a function of the irradiation condition, the mixture of substances in the target and the presence of impurities. The radionuclides generated from this “hot atom” chemistry and commonly used in PET are carbon-11, fluorine-18, nitrogen-13 and oxygen-15. Among them, carbon-11 and fluorine-18 are particularly important. Carbon-11 and fluorine-18 have certain advantages and limitations: 1) Almost every organic target molecule has carbon, but only a small pool has fluorine. Carbon-11 labeled compounds will have identical pharmacological properties compared to the carbon-12 equivalent, while introduction of fluorine-18 may alter the chemical and biological properties of the drug. 2) The longer half-life of fluorine-18 enables multiple step synthesis and transportation of doses to sites several hours away. However, carbon-11 is normally limited to a much short time scale of reaction and an in-house cyclotron is always necessary. 3) Fluorine-18 provides better resolution than carbon-11 as it has lower energy[67].

Carbon-11 has a 20.4 min half-life and almost 100% of the radioactive decays are by positron emission. There are several reactions that can be used to produce carbon-11, with the $^{14}N(p,\alpha)^{11}C$ reaction on nitrogen gas being preferred[69]. With the addition of a small amount of oxygen, this reaction produces high yield of carbon-11 in the form of carbon dioxide. If hydrogen is added instead, this reaction yields carbon-11 in the form of methane. As nitrogen gas from the target is normally inert, the separation of carbon-

11 in the gas is accomplished by passing through a solution or solid phase trap. From there, the carbon-11 can be used to produce a wide range of precursors (**Scheme 1.1**)[67].

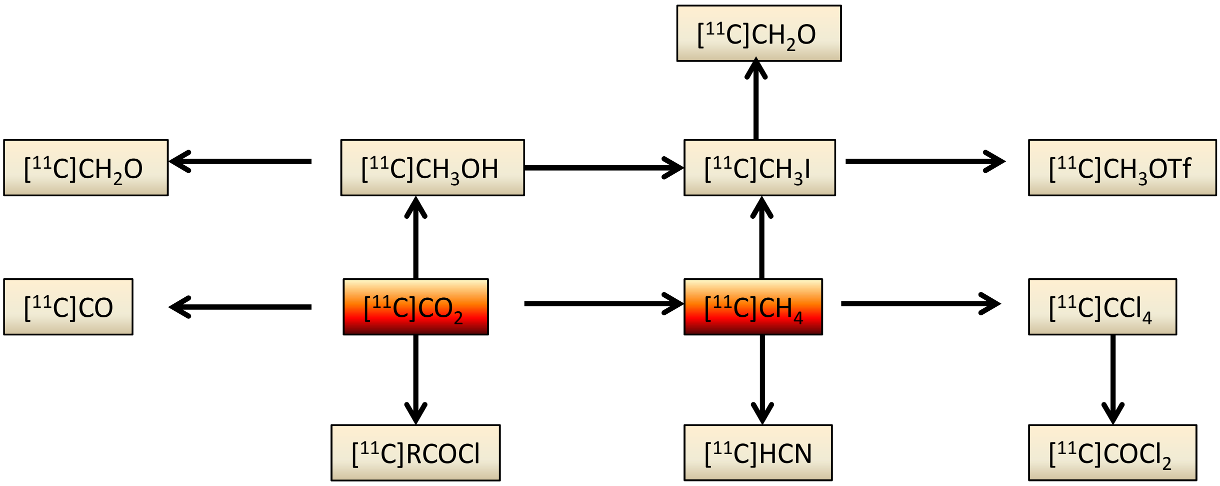

Scheme 1.1 Important Carbon-11 precursors produced from $[^{11}C]CO_2$ or $[^{11}C]CH_4$[67]

$[^{11}C]CH_3I$ is the most commonly used methylation agent, and can be prepared by a wet method with $LiAlH_4$ and hydriodic acid or by the gas-solid method with iodine from $[^{11}C]CO_2$ and $[^{11}C]CH_4$, respectively[70,71]. A more reactive methylation agent, $[^{11}C]CH_3OTf$, can be prepared by passing gaseous $[^{11}C]CH_3I$ through a heated column of silver triflate. The resulting agent has become more widely used recently because of its better reactivity and low volatility[72]. $[^{11}C]HCN$ is another commonly used starting material as the nitrile group is widely found in pharmaceutical molecules. The preparation of $[^{11}C]HCN$ involves reduction from $[^{11}C]CO_2$ to $[^{11}C]CH_4$ with H_2 and subsequent reaction with NH_3 over platinum[73]. The carbonyl group exists widely in biologically interesting molecule, and [^{11}C]CO is utilized as a labeling precursor for this group. [^{11}C]CO is readily synthesized from [^{11}C]CO_2 through heated zinc or molybdenum with the latter giving higher and more reliable yields[67]. [^{11}C]RCOCl can be utilized for incorporation of carbonyl functional groups and can be readily prepared with desired Grignard reagents. Another labeling molecule for the carbonyl functional group is [^{11}C]$COCl_2$ and it can be prepared from [^{11}C]CCl_4 by reaction with Fe_2O_3 powder and Fe granules[74]. [^{11}C]CH_2O was identified as a useful labeling reagent more than a decade ago, and now a new synthetic method has been developed which involves the oxidation of [^{11}C]CH_3I with trimethylamine *N*-oxide[75].

Fluorine-18 has a 110 min half-life and is the most widely used radionuclide in PET. 97% of the decays are positron emission, with 3% electron capture. Among a number of nuclear reactions that can be used to produce fluorine-18, $^{18}O(p,n)^{18}F$ and $^{20}Ne(d,\alpha)^{18}F$ are the major routes[76], and the resulting [^{18}F]F^- and [^{18}F]F_2 are the major forms of fluorine-18 for subsequent labeling reaction.

Incorporation of radionuclides

Introduction of the radioisotope with the labeling precursor is the second step in the process of applying PET imaging applications. Although the half-life of carbon-11 and fluorine-18 are only 20.4 min and 110 min, respectively, a large number of reactions have been developed in order to incorporate these isotopes into the probes in the appropriate time frame with limited forms of carbon-11 and fluorine-18 sources.

Labeling with carbon-11

Methylation with [^{11}C]CH_3I or [^{11}C]CH_3Tf is the most commonly used method for introduction of carbon-11 into organic molecules. It can be accomplished by either nucleophilic reaction with amine, alcohol or thiol precursor groups or palladium mediated methylation with stannanes. Typical examples include radiosynthesis of [^{11}C]raclopride, an antagonist of dopamine D2 receptor, and [^{11}C]M-MTEB, a metabotropic glutamate receptors ligand[77,78]. Labeling of carbonyl groups with carbon-11 is another widely accepted method of radiotracer generation, which can be accomplished with [^{11}C]$COCl_2$, [^{11}C]CO, [^{11}C]CO_2, or [^{11}C]HCN. Examples of radiotracers that have been synthesized using these precursors include [^{11}C]RPR-72840A, an serotonin reuptake inhibitor, [^{11}C]metergoline, an serotonin receptor antagonist and [^{11}C]INH, an enoyl-ACP reductase inhibitor (**Scheme 1.2**)[79-81].

Labeling with Fluorine-18

Fluorination is most commonly performed using nucleophilic reactions with [^{18}F]F^-. Several forms of [^{18}F]F^- can be used including [^{18}F]KF.K_{222}, [^{18}F]TBAF and [^{18}F]CsF. The key idea is to expose a “naked” [^{18}F]F^- and make it a better nucleophile. Forms of [^{18}F]F^- can be incorporated through aromatic and aliphatic nucleophilic substitution reactions. For example, the synthesis of [^{18}F]haloperidol, a dopamine antagonist, utilizes aromatic nucleophilic substitution, and [^{18}F]FDG, a widely used glucose analog, utilizes an aliphatic substitution reaction[82,83]. Electrophilic fluorination is an additional way to incorporate [^{18}F]F, although this method leads to lower specific activity and reaction selectivity in comparison with [^{18}F]F^{-}[67]. The best example of this approach is the first synthesis of [^{18}F]FDG at Brookhaven National Lab (**Scheme 1.2**)[66].

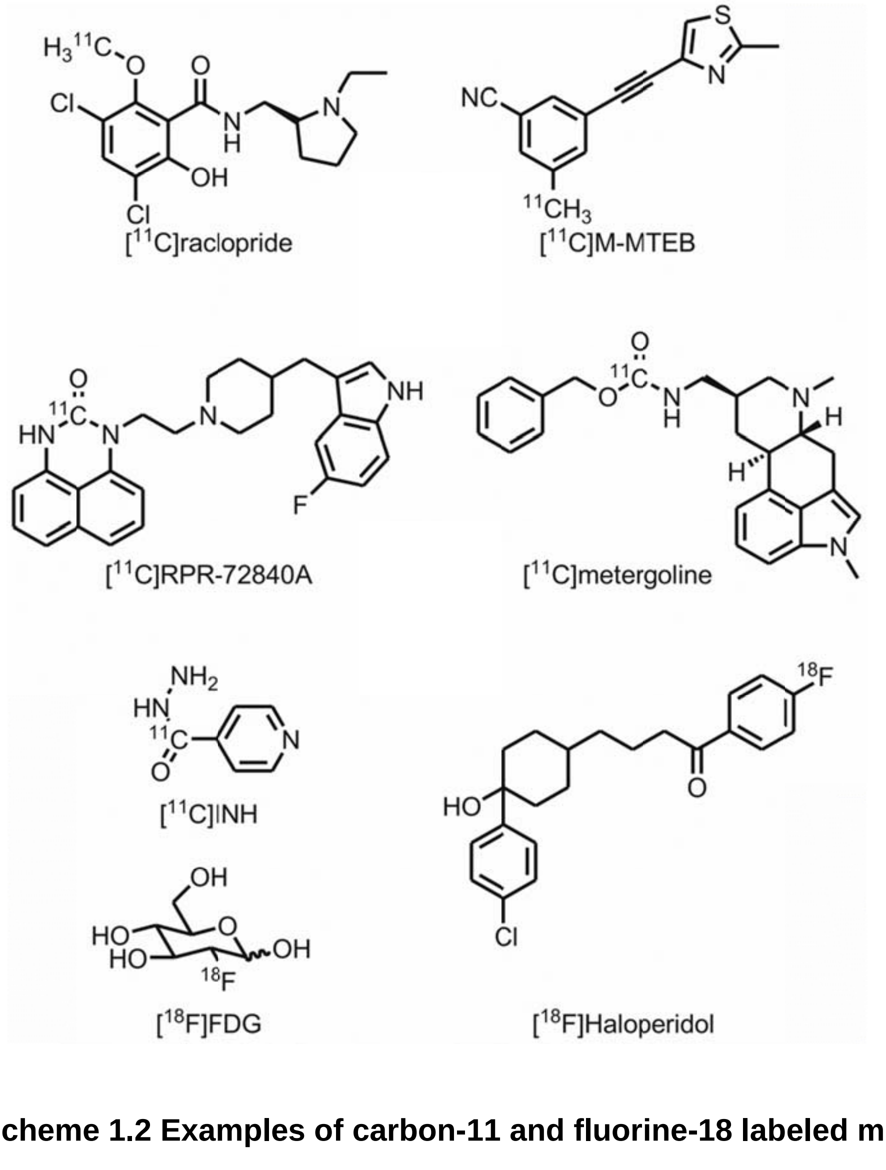

Scheme 1.2 Examples of carbon-11 and fluorine-18 labeled molecules

Summary

There is pressing need to understand the drug concentration at the side of infection for antibiotic discovery and better treatment regimes. In addition, timely identification and localization of infectious diseases is critical for appropriate treatment. We will first develop radiosynthesis methods or adopt existing methods to incorporate carbon-11 or fluorine-18 into the molecules of interest, which includes [^{11}C]INH with its [^{18}F]F labeled analog, [^{11}C]RIF, [^{11}C]PZA, [^{11}C]PT70, [^{11}C]PT119 and [^{18}F]PT161 and conduct PET imaging of those molecules in healthy animals and/or humans to understand the tissue PK. Second, we will utilize these radiolabeled probes to evaluate our ability to image bacterial infection, with specific focus on the two medically important pathogens *S. aureus* and *Mycobacterium Tuberculosis* (Mtb).

Chapter 2

Radiosynthesis and Bioimaging of the Tuberculosis Chemotherapeutics Isoniazid, Rifampicin and Pyrazinamide in Baboons

This chapter is based on the work that has been published in:

Liu, L.; Xu, Y.; Shea, C.; Fowler, J.S.; Hooker, J.M. and Tonge, P.J. “Radiosynthesis and Bioimaging of the Tuberculosis Chemotherapeutics Isoniazid, Rifampicin and Pyrazinamide in Baboons.” *J. Med. Chem.* **2010**, *53*, 2882-91

Dr. Hooker guided the development of radiosynthesis method. Drs. Fowler, Hooker and Tonge helped with the writing and revision of this publication.

Introduction

The dose and duration of treatment of antibiotics is normally established using plasma pharmacokinetic (PK) data together with information on drug efficacy once treatment has been initiated. Although plasma drug concentration is an important guide for establishing treatment protocols, recent studies indicate that the distribution of antibiotics in tissues is a more critical determinant and predictive factor for their activity[7,8]. This is because most drugs exert their bactericidal effects at the site of infection rather than in the plasma, and because drug equilibration between plasma and infection site cannot always be achieved[7,8]. Failure to reach optimal drug concentration at the site of infection may result in therapeutic failure and trigger bacterial resistance[8]. Therefore, the Food and Drug Administration (FDA) now requires clinical studies of tissue drug distribution at uninfected and infected sites[8]. Positron emission tomography (PET), which images drugs and other molecules labeled with positron-emitting isotopes, provides a method of acquiring quantitative information on the dynamics of drug absorption, distribution and elimination in a living animal or human. Together with advances in the development of methods for labeling drug molecules and other organic compounds with carbon-11 (half-life: 20.4 min), PET is emerging as a powerful alternative to *ex vivo* distribution studies using laboratory animals which sample a single time point per animal. Indeed PET can map three-dimensional tissue distribution over time non-invasively[15]. It is also complementary to clinical microdialysis (MD) and magnetic resonance spectroscopy (MRS) in terms of acquiring information on the tissue distribution of different chemical species[7]. In addition, the methodology developed for imaging drug distribution in laboratory animals using PET can be readily translated to humans[15].

More than two million deaths every year are attributed to infection with *Mycobacterium tuberculosis* (MTB) and the world health organization (WHO) has estimated that one third of the world's population is infected with this pathogen[84-86]. While many bacterial infections are treated using 1-2 weeks course of monotherapy, the treatment of tuberculosis (TB) requires the use of multiple antibiotics over a 6-9 month period, dramatically increasing the risk of noncompliance and enhancing the emergence of resistance[87]. The current treatment regime for drug-sensitive TB involves the use of isoniazid (INH), rifampicin (RIF), pyrazinamide (PZA) and ethambutol (EMB) or streptomycin for two months, followed by four months of continued dosing with INH and

RIF. This regime has been used for decades and is primarily based on PK studies in serum combined with historical data on the efficacy of treatment[88]. TB infection most commonly occurs through inhalation of live bacteria, and thus the primary site of infection in humans is the lung. However, MTB can also disseminate via the blood stream and infect other organs in the body. In particular, MTB infection of the brain (central nervous system TB, CNS TB) can occur. CNS TB is presented in many forms including tuberculous meningitis, cerebral tuberculomas without meningitis and spinal TB[89]. CNS TB is particularly difficult to manage since the pathogenesis, diagnosis and treatment of this form of TB infection has not been as intensively studied as pulmonary TB and there is little data to guide treatment options[89,90]. Current treatment for CNS TB normally follows the same format as that used for treating pulmonary TB, and involves an intensive phase of treatment followed by a continuation phase[89,90]. Thus, both INH and RIF are included in the treatment based on their potent activity against pulmonary TB infection and, in the case of INH, the significant levels of this drug that can be detected in the cerebrospinal fluid (CSF). In addition, although high concentrations of PZA can be detected in the CSF, the importance of this drug for treating CNS TB is largely unknown[89,90]. Although measurement of CSF drug concentration through lumbar puncture is a good indication of drug availability in brain, it would be advantageous to be able to measure brain drug distribution non-invasively and more accurately since a ventriculo-lumbar concentration gradient is often observed and the distribution of drugs in each compartment of the CNS is not homogeneous[91].

Here we present a PET imaging study of carbon-11 labeled RIF, INH and PZA in baboons in order to provide more direct insight into the PK and biodistribution of drugs commonly used to treat TB. These studies in healthy baboons, are a prelude to imaging experiments in infected animals and humans, which should ultimately be useful in evaluating new TB treatment regimes, especially for disseminated forms of the disease such as CNS TB where the ability to evaluate drug availability at the site of infection may be limited.

Using PET, we find that all three drugs and/or their radiolabeled metabolites are cleared rapidly from the lungs. In addition, their accumulations are consistent with the mechanism of excretion of each drug. We also find that the organ distribution of each drug differs by 1-1000 fold from the plasma drug distribution. All of the three injected drugs demonstrated higher concentrations in the lung than the plasma over the time course of the experiment. In addition, we find that the ability of the drugs to penetrate the blood-brain barrier decreases in the order PZA > INH > RIF. Estimates based on the weight of the baboon, a standard drug dose and the assumption that the positron signal derives primarily from the intact drug indicates that the concentrations of RIF, INH and PZA in the lungs are at least 10, 10 and 1-3 times higher, respectively, than the minimum inhibitory concentration (MIC) values for these drugs against MTB. Estimates of drug concentrations in the brain using the same assumptions outlined above suggest that the concentrations of RIF and INH are 3-4 and >10 times higher than their MIC values, while the concentration of PZA is similar to or slightly higher than its MIC. These data have important implications for the treatment of TB and CNS TB, and set the scene for additional studies in humans.

Results and Discussion

Radiosynthesis of [^{11}C]RIF

The radiolabeling of the RIF piperazine moiety with [^{11}C]CH_3I was accomplished by using potassium carbonate and a combination of DMSO and MeCN (**Scheme 2.1**). Although the conditions for labeling a piperazine with [^{11}C]CH_3I have been published before[92], we were concerned that other nucleophilic sites could also be alkylated (e.g. *O*-methylation of the phenolic oxygens).

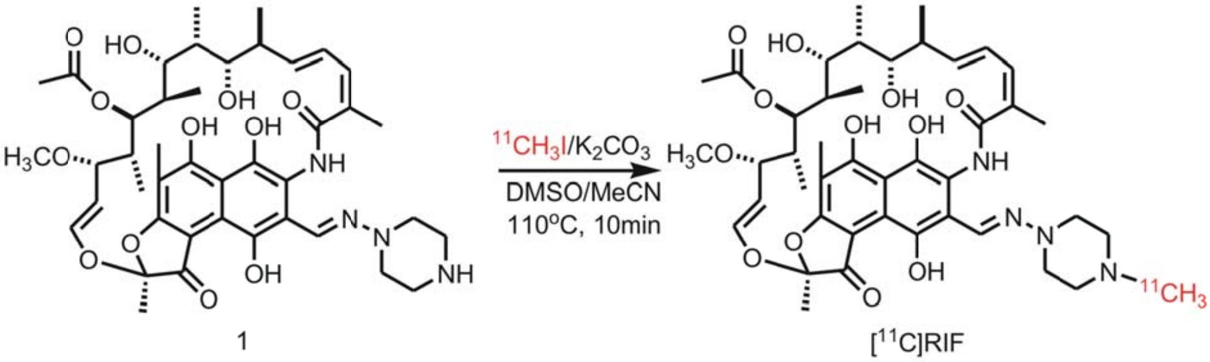

Scheme 2.1 Radiosynthesis of [^{11}C]RIF

Consequently, we explored a range of non-nucleophilic organic and inorganic bases in combination with polar aprotic solvents in order to identify conditions that would give the required rate, radiochemical yield and regioselectivity (i.e. *N*-methylation). These studies resulted in the use of potassium carbonate as the base and a combination of DMSO and MeCN as the solvent (**Scheme 1**). The [^{11}C]RIF was subsequently purified by high performance liquid chromatography (HPLC) using a semi-preparative

Phenomenex Luna C-18 column (250×10, 5 μm) and 100 mg of ascorbic acid was added to the product solution prior to concentration *in vacuo* in order to prevent oxidation. In the optimized reaction scheme, the average decay-corrected yield (DCY), calculated from [^{11}C]CH_3I, was 15%-25% in a total synthesis time of 50 min. Analytical HPLC and TLC demonstrated that the radiolabeled product was over 99% radiochemically pure, with a specific activity of 580 mCi/μmol at the time of delivery to the animal.

Radiosynthesis of [^{11}C]INH

The synthesis of [^{11}C]INH was accomplished in three steps beginning from [^{11}C]HCN. The first step involved treating iodopyridine (**2**) with [^{11}C]HCN in a DMSO reaction mixture catalyzed by tetrakis(triphenylphosphine)palladium(0) (**Scheme 2.2**) for 5 min to form [^{11}C]cyanopyridine (**3**). This method was adapted from previously reported radiolabeling of an aromatic ring with [^{11}C]HCN[93], and gave 90% radiochemical yield (RCY) as determined by HPLC.

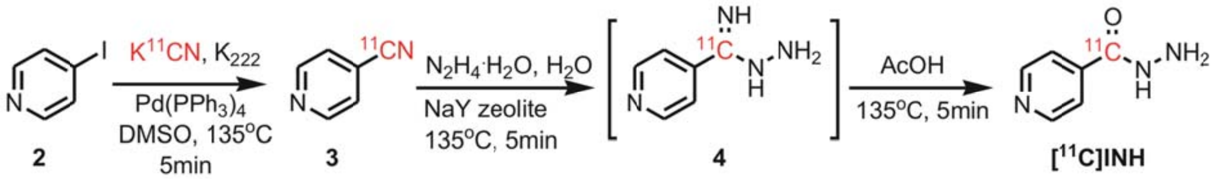

Scheme 2.2 Radiosynthesis of [^{11}C]INH

The subsequent hydrazine hydrolysis of the cyanide was accomplished in two steps which involved a nucleophilic attack by hydrazine and subsequent hydrolysis of the imine by water. This procedure was a modification of a published method[94], which used NaY zeolite as the catalyst to hydrolyze the aromatic cyano group without adding acetic acid to drive the reaction. Initial studies indicated that the hydrolysis step was too slow to be useful with carbon-11 (approximately 60 min at 180°C). However, since mass spectrometry revealed the formation of intermediate (**4**) together with the complete consumption of **3** within the first 5 min of the reaction, acetic acid was added to promote hydrolysis of the intermediate. Using this two step procedure, the hydrolysis time of **3** was reduced to 10 min. The final product was formed with an average 45%-50% DCY (calculated from [^{11}C]HCN) in a total synthesis time of 50 min. Isonicotinamide was the only major side product, but with optimization of the ratio between hydrazine, water and acetic acid (3:3:1), formation of this adduct could be reduced to less than 15% of the desired product. [^{11}C]INH was purified by semi-preparative HPLC and the amount of hydrazine in the sample, that initially coeluted with [^{11}C]INH, was reduced by leaving the sample on the rotary evaporator for 10 min. The average amount of hydrazine present in the injected solution was 8.2 μg/ml (~10.0 μg/injection) as determined by an analytical assay, which was adapted from a previous report[95]. Analytical HPLC and TLC were used to demonstrate that the radiolabeled product was over 99% radiochemically pure, with a specific activity of 140-165 mCi/μmol at the time of delivery.

Radiosynthesis of [^{11}C]PZA

The radiosynthesis of [^{11}C]PZA is shown in **Scheme 2.3**. Initially, [^{11}C]cyanopyrazine (**6**) was generated with a 90% RCY in 5 min from 2-iodopyrazine (**5**) and [^{11}C]HCN using tetrakis(triphenylphosphine)palladium(0) as the catalyst under the same reaction conditions as those used for [^{11}C]INH[93]. Subsequent hydrolysis of the cyano group was accomplished in an additional 5 min by treating the **6** with hydrogen peroxide under basic conditions. The overall DCY was 50%-55% (calculated from [^{11}C]HCN) in a total synthesis time of 45 min. An unidentified volatile compound co-eluted with the [^{11}C]PZA product during HPLC purification, however this was removed during concentration of the product *in vacuo*. Analytical HPLC and TLC demonstrated that the radiolabeled product was over 99% radiochemically pure, with a specific activity of 120-150 mCi/μmol at the time of delivery.

Scheme 2.3 Radiosynthesis of [^{11}C]PZA

LogD and plasma protein binding (PPB).

The lipophilicity (logD) and PPB of each drug was determined using the radiolabel to report on drug concentration. The results are presented in **Table 2.1**, and are similar to literature values reported elsewhere[96,97].

Table 2.1 LogD and PPB determination

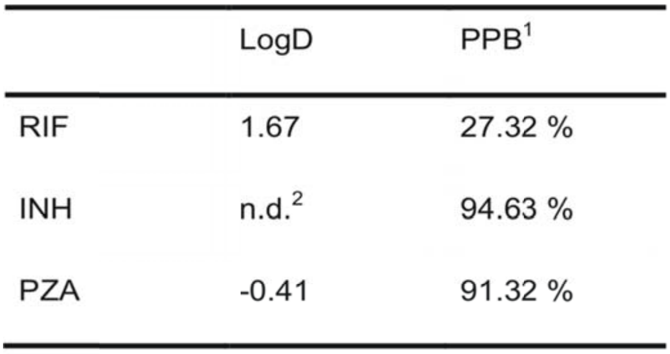

	LogD	PPB[1]
RIF	1.67	27.32 %
INH	n.d.[2]	94.63 %
PZA	-0.41	91.32 %

[1] Value expressed as % of free fraction in plasma

[2] Octanol water partitioning was highly variable

Brain PET imaging in anesthetized baboons.

PET imaging studies were performed with [^{11}C]RIF, [^{11}C]INH and [^{11}C]PZA to determine brain penetration and distribution. Time-activity curves (TACs) (**Figure 2.1a**) were generated from the image data, which was acquired for 90 min following i.v. administration of each radiolabeled drug. Area under the curves (AUCs) (**Figure 2.1b**) were produced by integrating TACs as a function of time and dose corrected coronal images (**Figure 2.1c**) were generated by sum from 15 to 90 min. Regions-of-interest (ROIs) were drawn manually.

These PET studies are the first in which dynamic TB drug concentrations have been measured in whole brain tissue in a living animal. **Figure 2.1** clearly demonstrates that the ability of the drugs and their radiolabeled metabolites to penetrate the blood-brain barrier decreases in the order PZA > INH > RIF. The [^{11}C]RIF TAC, AUC and image (**Figure 2.1**) showed that RIF and/or its radiolabeled metabolites poorly penetrate the blood-brain barrier in healthy baboons, consistent with previous studies in which the concentration of i.v. delivered RIF in human CSF was measured, although our studies demonstrate a higher RIF concentration in brain tissue than that observed in the CSF.[98] The unit % of injected dose per cubic centimeter (%ID/cc) was used and the concentration of injected [^{11}C]RIF in the whole brain area was monitored over the 90 min scanning period with a C_{30min} = 0.000642 %ID/cc (1.09 μg/ml), C_{60min} = 0.000536 %ID/cc (0.912 μg/ml) and C_{90min} = 0.000710 %ID/cc (1.21 μg/ml).

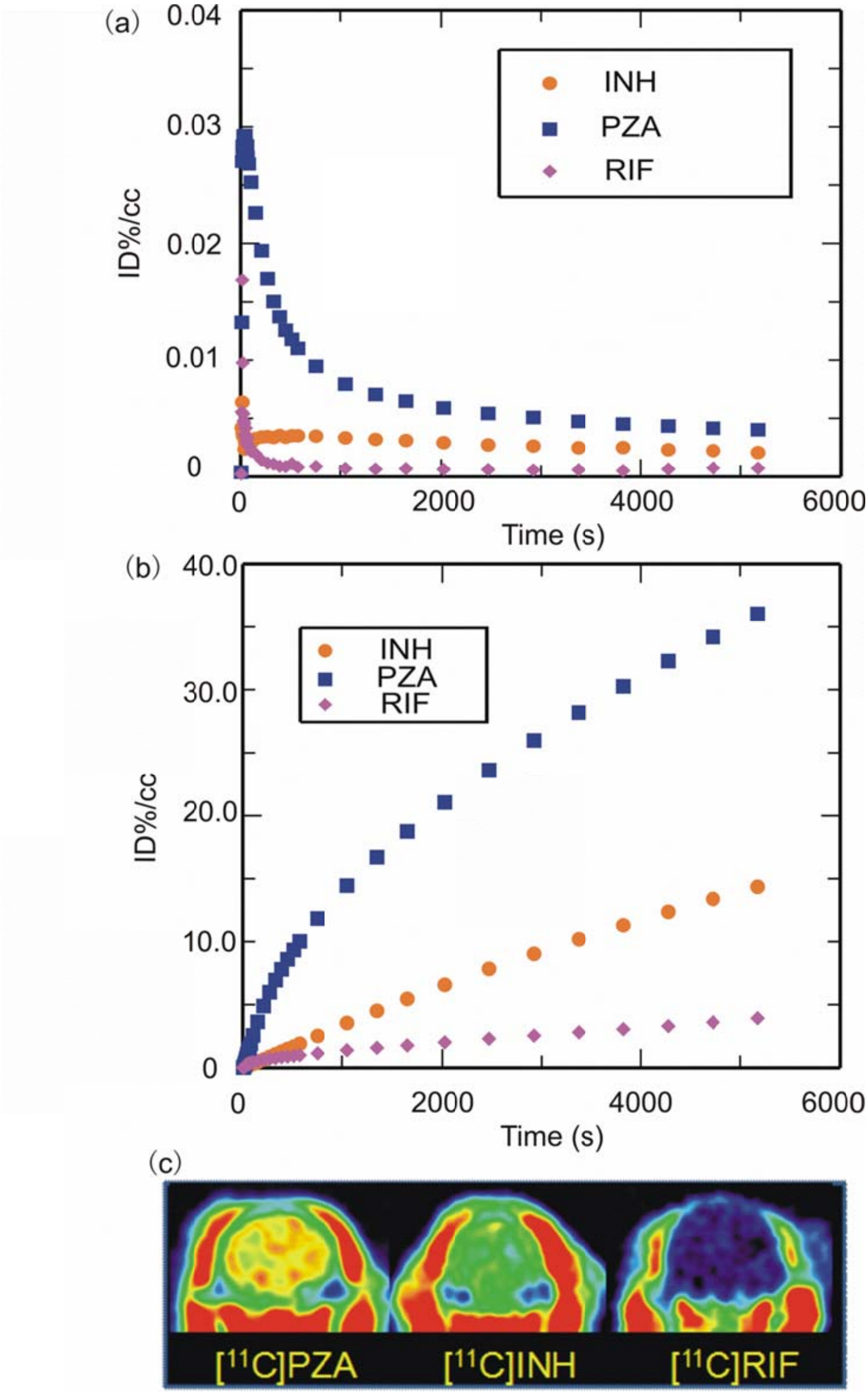

Figure 2.1 Blood-brain barrier penetration, brain tissue distribution and TACs for [^{11}C]INH, [^{11}C]RIF and [^{11}C]PZA.

(a) TACs generated from the image acquired after intravenous administration of each drug in baboons by manually drawing the ROIs. (b) Whole-brain regions of interest were used to generate TACs for each labeled drug. The resulting curves were integrated as a function of time to produce AUC plots. (c) Dose corrected coronal images summed over frames 24-35 (15-90 min). The NIH color scale was used to represent relative radioactivity concentration.

In parentheses we have estimated the expected concentration of RIF in the baboon brain based on the weight of the baboon (17 kg), the recommended daily dose for a human adult (10 mg/kg) and the assumption that the positron signal derives primarily from the intact drug. Thus, for a 17 kg baboon the injected dose is 170 mg and, for example, at 30 min the concentration in the brain is estimated to be 0.000642% of 170 mg which is 1.09 µg/ml. The anticipated concentration of RIF in the baboon brain is therefore 3-4 times above the MTB MIC for this compound, supporting the use of RIF for treating CNS TB infections[89,98]. The concentrations of RIF observed in our study are similar to the value of 0.87 µg/g determined in monkeys 6 hours after i.v. administration of [^{14}C]RIF[99], which suggests that the observed level of RIF could persist for several hours in brain tissue. In addition, although studies in mice revealed a much higher RIF brain tissue concentration of 10.25 µg/ml 3-7 hours after i.p. administration[100], the latter measurements were made with a 100 mg/kg dose of RIF, and thus are likely similar to the concentrations reported from our PET study if our estimates were based on a 100 mg/kg dose. Finally, Thomas and coworkers resected human brain tissue around tumors and determined a RIF concentration of 0.29 µg/ml following i.v. infusion of 600 mg RIF in 500 ml saline over 3h[101].

Thus, the concentrations of RIF determined by PET imaging the distribution of [^{11}C]RIF in healthy baboons are similar to those observed in mice and monkeys, while the ~3.5-fold difference between our values and that determined by resecting brain tissue could be due to the limited sampling region in the latter experiments. Although the studies with [^{14}C]RIF do provide information on drug distribution, this is only at a single time point, whereas the PET imaging experiments provide dynamic data from 0-90 min. Importantly, the PET studies are non-invasive and thus can be readily applied to determining RIF concentration and distribution in humans.

The [^{11}C]INH TAC, AUC and image (**Figure 2.1**) showed a higher initial brain penetration and tissue accumulation when compared to RIF, consistent with CSF analysis in humans[102,103]. The concentration of injected [^{11}C]INH in the whole brain area was monitored after i.v. administration (**Figure 2.1a**), and gave C_{30min} = 0.00299 %ID/cc (2.54 µg/ml), C_{60min} = 0.00248 %ID/cc (2.11 µg/ml) and C_{90min} = 0.00206 %ID/cc (1.75 µg/ml). Again, concentrations in µg/ml are estimated based on the weight of the baboon, the recommended daily dose for a human adult which is 5 mg/kg and the assumption that the positron signal derives primarily from the intact drug. Thus, the calculated INH concentration is more than 10 times above the MIC of this compound against MTB, and hence INH should be a suitable therapy for CNS TB infection as recommended[89], with the caveat that INH must be used with another drug since INH-resistant mutants emerge quickly during monotherapy[104]. Concentrations estimated from our [^{11}C]INH study are similar to those determined in mice using [^{14}C]INH in which a 10 mg/kg s.c. dose gave concentrations of 4.4 μg/g and 3.2 μg/g at 30 min and 60 min, respectively[105]. However, studies in cats in which [^{14}C]INH was administered i.p. revealed much lower penetration of INH into the brain, with a calculated INH concentration of only 0.02 μg/g[106,107]. The lower brain concentration of INH determined in cats compared to our baboon study could reflect interspecies differences and/or the different routes of administration that were used. Finally, although the observed CSF concentrations in humans from two experiments are contradictory (1.9 μg/ml with 8.5 mg/kg oral dose at 2 h[108] and 0.31 μg/ml with 108.7 mg oral dose at 1 h[102]), it is clear that the INH concentration in brain tissue is equal to, or greater than, the concentration in the CSF.

The [^{11}C]PZA TAC, AUC and image indicated excellent penetration of PZA into healthy brain tissue in vivo (**Figure 2.1**). This result is consistent with CSF analysis in humans in which the PZA concentration in the CSF exceeded that in the serum[109](e.g. brain C_{60min} = 0.00463 %ID/cc and plasma C_{60min} = 0.00272 %ID/cc). The concentration of [^{11}C]PZA in the whole brain area decreased following i.v. administration, with C_{30min} = 0.00619 %ID/cc (21.05 μg/ml), C_{60min} = 0.00463 %ID/cc (15.74 μg/ml) and C_{90min} = 0.00403 %ID/cc (13.70 μg/ml). As above, concentrations in μg/ml are estimated based on the weight of the baboon, the recommended daily dose for a human adult which is 20 mg/kg and the assumption that the positron signal derives primarily from the intact drug. We believe that this is the first study of PZA distribution in the primate brain. Studies with rats conducted by Wu and coworkers using MD gave similar brain tissue concentrations with a similar dose and i.v. administration[110]. In patients with inflamed meninges, the CSF concentration of PZA was 50 μg/ml following a single 3 g oral dose[109]. The calculated PZA concentration at different time points from our baboon study is similar to or slightly greater than the MIC value for this drug against MTB.

Torso PET imaging in anesthetized baboons

PET imaging studies were performed with [^{11}C]RIF, [^{11}C]INH and [^{11}C]PZA to determine their peripheral organ distribution. The TACs (**Figures 2.2, 2.3 and 2.4**) were generated from the image acquired after i.v. administration of each drug to baboons by manually drawing the ROIs.

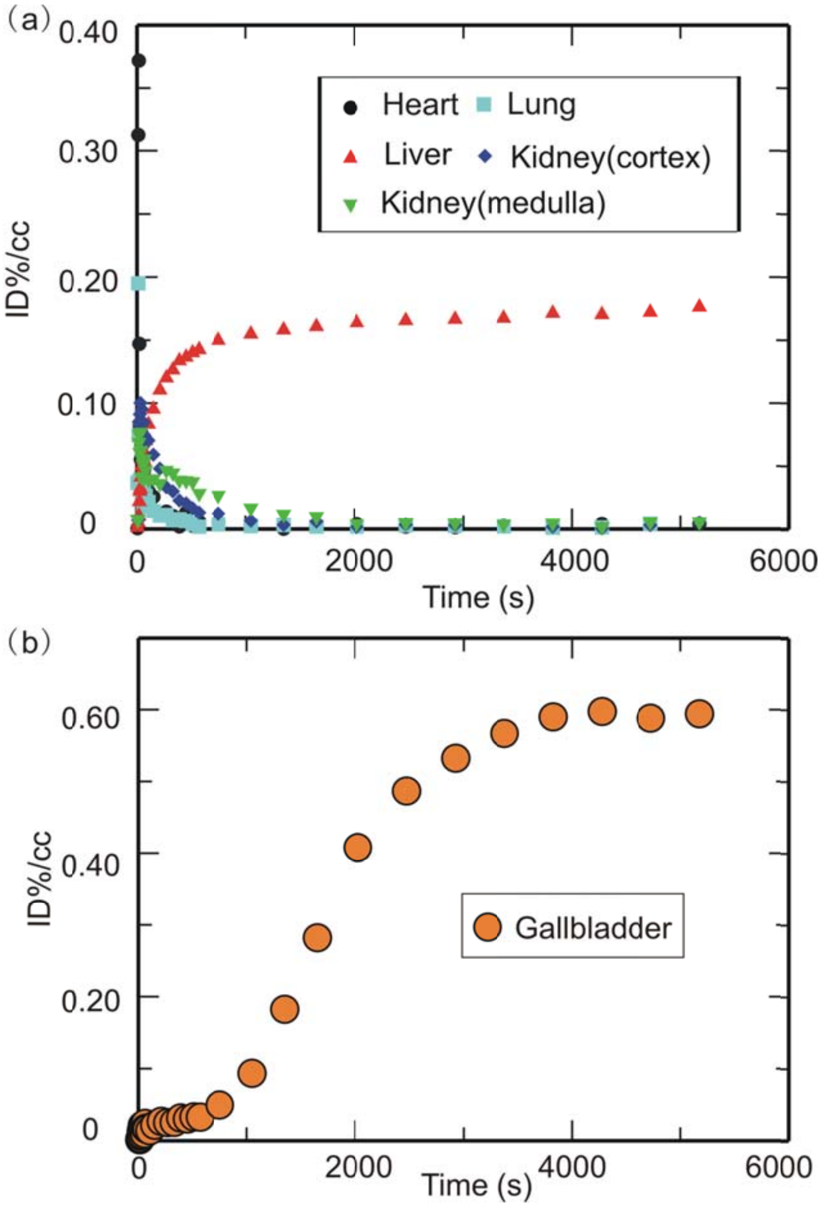

Figure 2.2 TACs for [^{11}C]RIF in the (a) heart, lungs, liver, kidneys and (b) gallbladder.

[^{11}C]RIF administered i.v. had moderate distribution in the heart, lung and kidneys, and was concentrated in the liver and gallbladder (**Figure 2.2**). The concentration of RIF in µg/ml at 15, 30, 60 and 90 min has been estimated based on the weight of the baboon, the recommended dose of RIF and assumption that the positron signal derives primarily from the intact drug (**Table 2.2**).

Table 2.2: Distribution of [^{11}C]RIF administered i.v. to baboons[1]

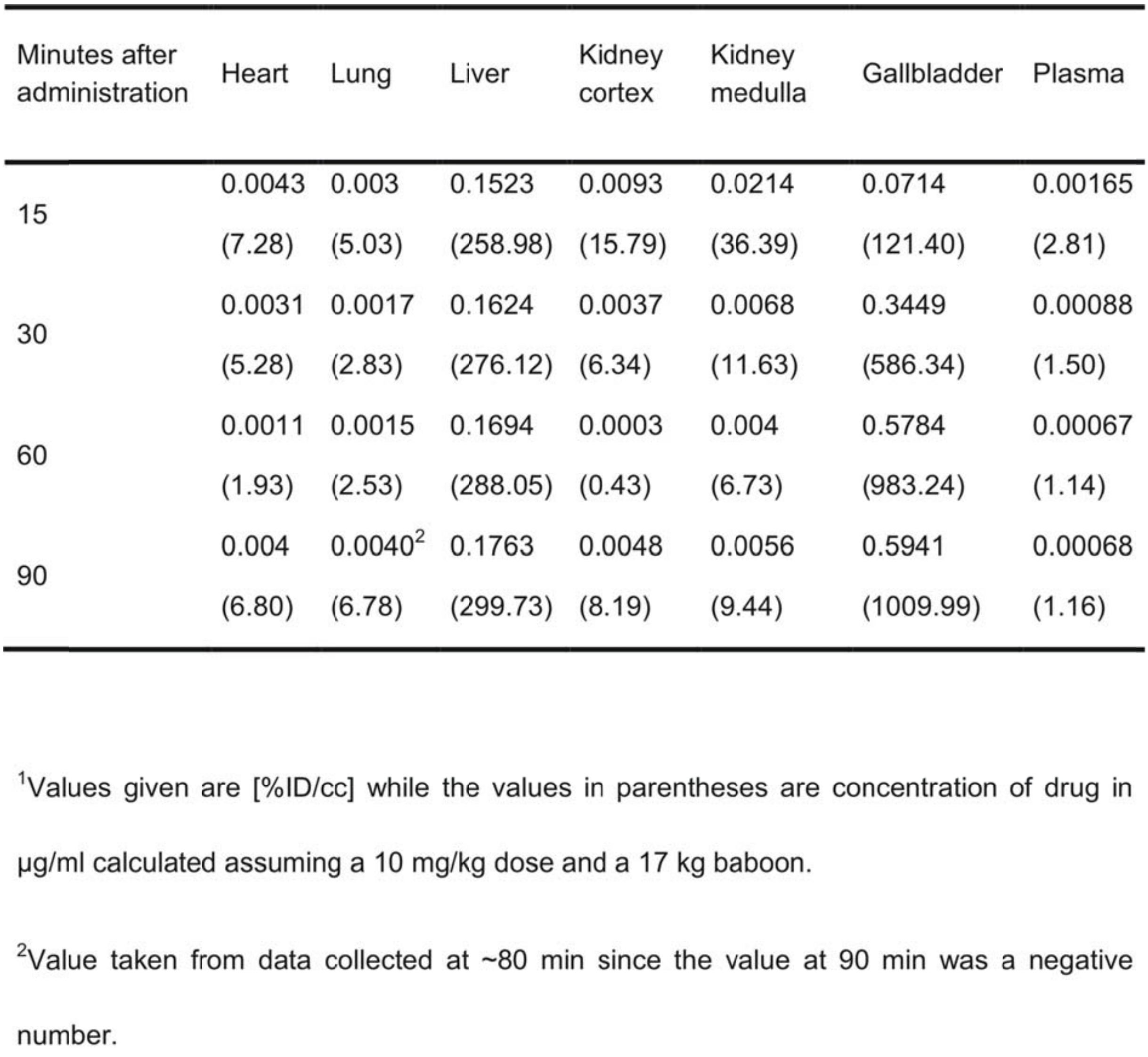

Minutes after administration	Heart	Lung	Liver	Kidney cortex	Kidney medulla	Gallbladder	Plasma
15	0.0043 (7.28)	0.003 (5.03)	0.1523 (258.98)	0.0093 (15.79)	0.0214 (36.39)	0.0714 (121.40)	0.00165 (2.81)
30	0.0031 (5.28)	0.0017 (2.83)	0.1624 (276.12)	0.0037 (6.34)	0.0068 (11.63)	0.3449 (586.34)	0.00088 (1.50)
60	0.0011 (1.93)	0.0015 (2.53)	0.1694 (288.05)	0.0003 (0.43)	0.004 (6.73)	0.5784 (983.24)	0.00067 (1.14)
90	0.004 (6.80)	0.0040[2] (6.78)	0.1763 (299.73)	0.0048 (8.19)	0.0056 (9.44)	0.5941 (1009.99)	0.00068 (1.16)

[1] Values given are [%ID/cc] while the values in parentheses are concentration of drug in μg/ml calculated assuming a 10 mg/kg dose and a 17 kg baboon.

[2] Value taken from data collected at ~80 min since the value at 90 min was a negative number.

The anticipated concentration of RIF in the lung is more than 10 times above the MTB MIC for this compound, and hence RIF should be a suitable therapy for TB infections as recommended by American Thoracic Society[88]. In most organs the concentration of injected RIF exceeds that in plasma over the study period except for the cortex of the kidney at 60 min. Although Nitti et al. have reported a PK study of RIF administered i.v. from 15 min to 12 h[111], these results are difficult to compare with our own since in their case the RIF was infused over a 3 h period. Furesz and coworkers used samples obtained by biopsy to determine the concentration of orally administered RIF in the organs and body fluid of patients with diseases that are presumed not to affect the absorption and elimination of RIF[112]. Although these data do not show concentrations before 90 min, the relative abundance of RIF in each organ and body fluid is quite similar to our own measurements and shows that in most cases the concentration of drug in the organs exceeds that in the serum. In their study, the bile concentration after 150 mg oral dose is up to 538.5 µg/ml at 3-5 h, while the concentration in the liver is between 22-35 µg/ml which is several fold smaller than our estimated liver concentration. This result may suggest that RIF is cleared quickly from the liver between 1.5 h to 3 h post administration. Our data can also be compared with the tissue distribution of RIF in monkeys performed 6 h after i.v. administering [^{14}C]RIF. In the latter experiment the liver still had the highest concentration (60.41µg/g), while the heart, lung and kidney retained some drug (10.11 µg/g, 8.32 µg/g and 14.69 µg/g, respectively)[99]. Finally, a semi-quantitative evaluation of whole body RIF distribution in mice using i.v. injected [^{14}C]RIF suggested a similar drug distribution compared to our own studies except that the difference between the liver and other organs was not as large[113].

The tissue distribution of injected [^{11}C]INH is shown in **Figure 2.3** where it is clear that INH and/or its radiolabeled metabolites rapidly penetrates the heart, lung, liver and kidney.

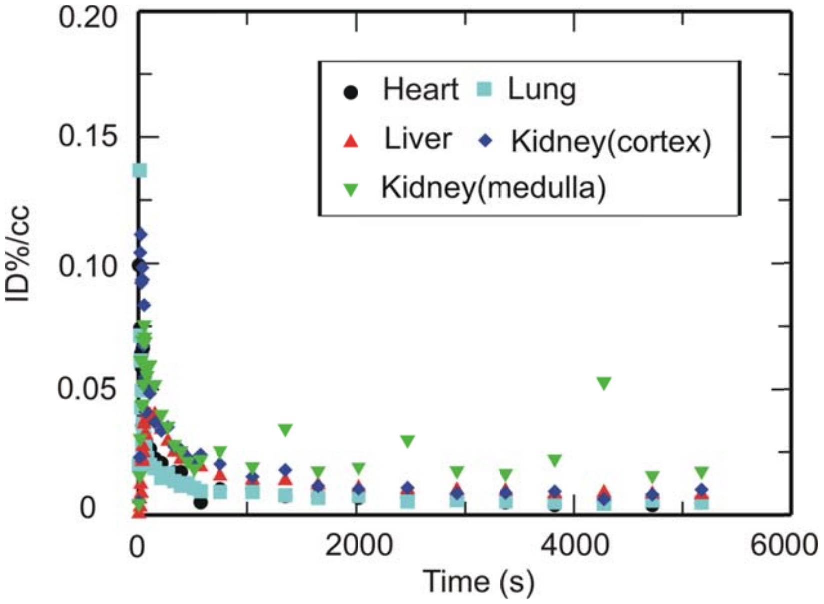

Figure 2.3 TACs for [^{11}C]INH in the heart, lungs, liver and kidneys

Table 2.3 gives the estimated concentration of INH in μg/ml at 15, 30, 60 and 90 min following i.v. administration based on the recommended dose of INH, the weight of the baboon and assumption that the positron signal derives primarily from the intact drug. The calculated INH concentration is more than 10 times the MIC of this compound against MTB, and hence INH should be a suitable therapy for TB infection as recommended[88]. Barclay and coworkers have shown that the concentration of INH in a surgically removed normal human lung is 1.79 μg/g at about 3 h after i.v. administration of 108.7 mg INH using [^{14}C]INH as the tracer[102]. In addition, Roth and coworkers have studied the distribution of INH in mice using s.c. injected [^{14}C]INH and have shown similar drug distributions at 0.5 h and 1 h compared to our baboon study assuming that 10 mg/kg drug is administered.[105] Other studies in mice with i.v. administration show drug concentrations in the liver, lung and kidney that are several fold higher than the amounts estimated using PET imaging[114], while Roohi et al. used a technetium-99m derivative of INH to determine the drug biodistribution in Sprague-Dawley rats giving similar drug concentrations in heart and lung but more than 10-fold higher concentrations in the liver and kidney compared to the other studies[115]. Again, interspecies variation could play an important role in any differences observed between our study and those conducted in rodents, with the additional caveat that the study in rats involved the use of INH that had been modified with technetium-99m.

Table 2.3 Distribution of [^{11}C]INH administered i.v. to baboons.[1]

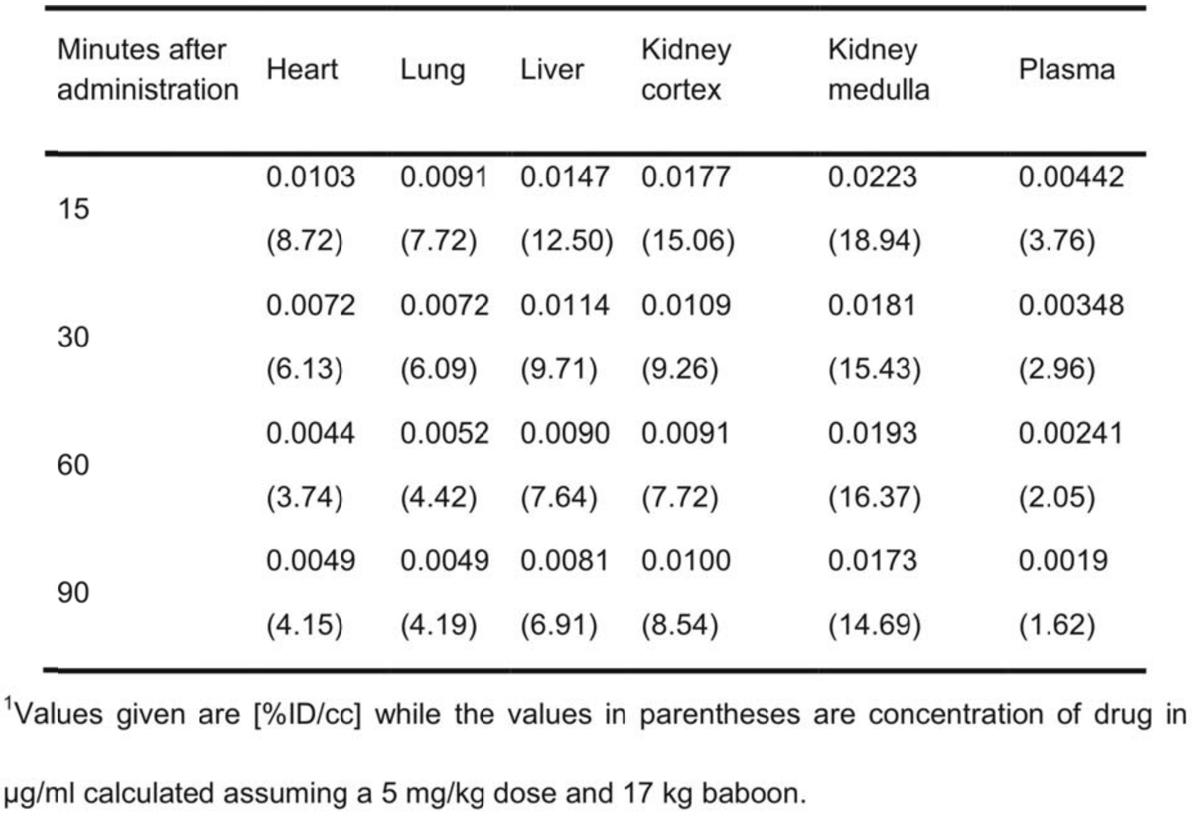

Minutes after administration	Heart	Lung	Liver	Kidney cortex	Kidney medulla	Plasma
15	0.0103 (8.72)	0.0091 (7.72)	0.0147 (12.50)	0.0177 (15.06)	0.0223 (18.94)	0.00442 (3.76)
30	0.0072 (6.13)	0.0072 (6.09)	0.0114 (9.71)	0.0109 (9.26)	0.0181 (15.43)	0.00348 (2.96)
60	0.0044 (3.74)	0.0052 (4.42)	0.0090 (7.64)	0.0091 (7.72)	0.0193 (16.37)	0.00241 (2.05)
90	0.0049 (4.15)	0.0049 (4.19)	0.0081 (6.91)	0.0100 (8.54)	0.0173 (14.69)	0.0019 (1.62)

[1]Values given are [%ID/cc] while the values in parentheses are concentration of drug in µg/ml calculated assuming a 5 mg/kg dose and 17 kg baboon.

The tissue distribution of [^{11}C]PZA administered i.v. is shown in **Figure 2.4**. The concentration of PZA at 15, 30, 60 and 90 min has been estimated based on the weight of the baboon, the recommended dose of PZA and the assumption that the positron signal derives primarily from the intact drug (**Table 2.4**). The calculated PZA concentration is 1-3 fold higher than the MIC of this compound against MTB. [^{11}C]PZA and/or its radiolabeled metabolites rapidly penetrated the heart, lungs, liver and kidneys, and in all cases the tissue concentration of PZA exceeded the concentration in serum with the exception of the kidney cortex. The calculated plasma concentration agreed closely with the published value determined in rabbits with i.v. administration[116], while the known plasma concentration in humans following oral administration of PZA is about twice that determined in our baboon study[117].

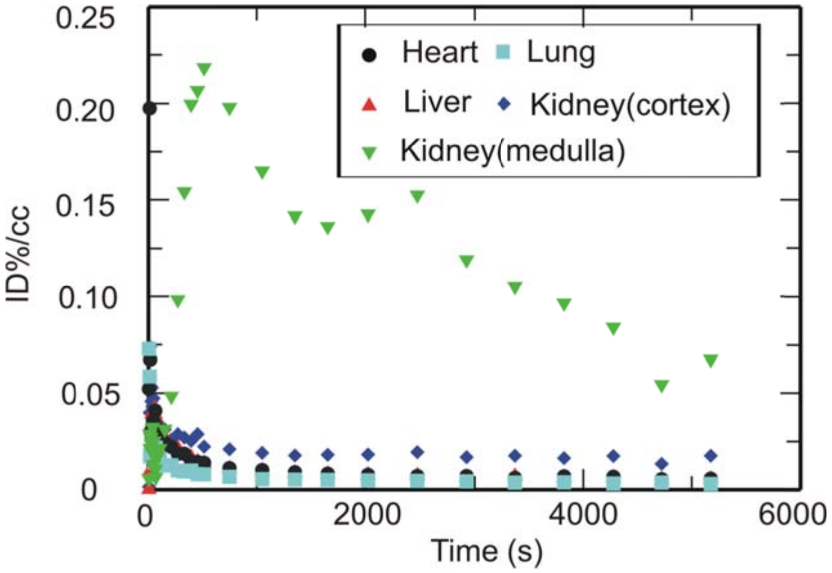

Figure 2.4: TACs for [^{11}C]PZA in the heart, lungs, liver and kidneys.

The organ distribution in rabbits has also been examined by dissection and gave a lower concentration of PZA in the lungs, kidneys and liver compared to that determined in baboons[116]. Since the blood concentration is quite similar in the two studies, the difference in organ distribution could result from differences in drug permeability in the two species. The ability of PZA to cross the blood-brain barrier in rabbits is also quite different since PZA was not observed in the rabbit brain[116] in contrast to our studies and other literature reports[109]. The concentrations of PZA in baboons determined in the present work are broadly similar to the plasma concentration of PZA determined by MD and HPLC-MS in rats[110], and in humans 1 h after oral administration of 27 mg/kg PZA[118].

Table 2.4: Distribution of [^{11}C]PZA administered i.v. to baboons.[1]

Minutes after administration	Heart	Lung	Liver	Kidney cortex	Kidney medulla	Plasma
15	0.0199 (67.76)	0.0103 (35.03)	0.0106 (36.14)	0.0060 (20.52)	0.1815 (617.02)	0.00648 (22.03)
30	0.0181 (61.50)	0.0078 (26.48)	0.0079 (26.96)	0.0049 (16.59)	0.1395 (474.39)	0.00429 (14.59)
60	0.0169 (57.59)	0.0065 (22.17)	0.0065 (21.98)	0.0037 (12.55)	0.1009 (343.00)	0.00331 (11.25)
90	0.0175 (59.49)	0.0055 (18.58)	0.0056 (19.19)	0.0029 (9.93)	0.0675 (229.44)	0.00266 (9.04)

[1] Values given are [%ID/cc] while the values in parentheses are concentration of drug in µg/ml calculated assuming a 20 mg/kg dose and a 17 kg baboon.

The imaging experiments reported in the present work were conducted using drug administered i.v. and so represent the fate of the drugs once they reach the serum. This is an important point given that the normal route of administration for INH, PZA and RIF is by mouth. In addition, only micro doses of drugs were used, and we are aware that drug distribution can change as a function of administered dose if one or more processes that affect distribution become saturated. However, based on the mechanism of action of these drugs together with our experience from other drug PK studies, we believe that saturable processes are likely to play only a minor role in modulating distribution. These studies, which were conducted using healthy baboons, thus clearly highlight the utility of using PET imaging to determine drug PK parameters and drug biodistribution non-invasively *in vivo*, and are a prelude to imaging experiments in infected animals and humans. Ultimately, this approach should be useful for determining better TB treatment regimes, especially for disseminated forms of the disease such as CNS TB where assessing drug availability at the site of infection may be difficult. It is also hypothesized that these labeled drugs may be eventually useful for determining the location of bacterial populations *in vivo* since these drugs are expected to accumulate within the bacteria either by conversion to metabolites that are unable to rapidly leave the cell or by binding with long residence times to their drug targets. Both PZA and INH are prodrugs for which activating enzymes are present in the mycobacterium[119,120], while the INH-NAD adduct, which is the active form of INH, has a residence time of 60 min on the MTB enoyl-ACP reductase InhA[121]. In addition RIF is also thought to have a long residence time on the mycobacterial RNA polymerase based on studies with the *E. coli* homologue which provided a residence time of ~90 min[122]. Importantly, the rapid clearance of all drugs and/or their radiolabeled metabolites from the lungs provides a clear window for imaging populations of TB bacteria since this is the primary site of TB infection.

Conclusions

The front-line TB chemotherapeutics INH, RIF and PZA have been labeled with carbon-11 and the biodistribution of the labeled drugs has been imaged in baboons *in vivo*. These PET imaging studies provide an opportunity to review the bioavailability of known drugs both in the brain and peripheral organs, which could potentially improve their use and help to determine the effective dose since these methods can be easily translated to healthy volunteers and patients. Radiosynthesis and formulation of each drug has been accomplished in 1 h, using $[^{11}C]CH_3I$ to label RIF and $[^{11}C]HCN$ to label INH and PZA. Following i.v. administration, the labeled drugs have been imaged in baboons using PET. INH, PZA, RIF and/or their metabolites clear rapidly from many tissues, however INH, PZA and/or their metabolites accumulate in the bladder while RIF and/or its metabolites accumulate in the liver and gall bladder, consistent with the routes of excretion of the drugs. In addition, estimates based on the weight of baboon, a standard drug dose and the assumption that the positron signal derives primarily from the intact drug indicates that the concentrations of RIF, INH and PZA in the lungs are at least 10, 10 and 1-3 times higher, respectively, than the MIC values for these drugs against MTB. Furthermore, we find that the ability of the drugs and their radiolabeled metabolites to penetrate the blood-brain barrier decreases in the order PZA > INH > RIF. Estimates of drug concentrations in the brain using the same assumptions outlined above suggest that the concentrations of RIF and INH are 3-4 and >10 times higher than their MIC values, respectively, while PZA is similar to or slightly higher than the MIC. The PK and drug distribution data have important implications for treatment of disseminated TB in the brain, and set the scene for imaging the distribution of the pathogen *in vivo*.

Experimental Section

General

$[^{11}C]CH_3I$ was generated from $[^{11}C]CO_2$ using a PETtrace MeI Microlab (GE Medical System, Milwaukee, WI, USA). Briefly, $[^{11}C]CO_2$ was obtained from proton bombardment of a N_2/O_2 target ($^{14}N(p,\alpha)^{11}C$) using an EBCO TR 19 cyclotron (Advanced Cyclotron System INC. Richmond, Canada). $[^{11}C]CO_2$ was heated with H_2 on nickel to produce $[^{11}C]CH_4$ and the latter was converted to $[^{11}C]CH_3I$ by iodination which was released into a stream of argon.

$[^{11}C]HCN$ was generated from $[^{11}C]CO_2$ using a home-made unit. Briefly, $[^{11}C]CO_2$ was obtained and converted to $[^{11}C]CH_4$ using the same conditions as those used for $[^{11}C]CH_3I$ production. Reaction of $[^{11}C]CH_4$ and NH_3 mediated by platinum produced $[^{11}C]HCN$ which was released into a stream of argon.

Chemical and radiochemical purity was determined by an analytical HPLC system equipped with both UV and radioactivity detectors. The purities of the intermediate and final products were > 95%, and the specific solvent gradients used for each compound are given below.

Synthesis of de-methyl RIF(1) (RIF precursor)

1-Nitrosopiperazine[123]. Piperazine 0.86 g (10 mmol) in 6N HCl (6 ml) was cooled to -10°C and a solution of $NaNO_2$ (0.69 g, 10 mmol) in H_2O (12 ml) was added slowly over 1 h. At a temperature below 0 °C, the pH was adjusted to 10 using NaOH, and then the mixture was extracted using chloroform, dried over Na_2SO_4, and the solvent removed by evaporation. The crude product was purified by column chromatography using silica gel and 8% $MeOH/CH_2Cl_2$ as the mobile phase. The product was a yellow oil and the yield was 72%. ^{1}H-NMR(300 MHz, $CDCl_3$) δ: 4.15-4.18(m, 2H), 3.74-3.77(m, 2H), 3.00-3.03(m, 2H), 2.75-2.79(m, 2H), 1.83(s, 1H). ESI-MS calculated for $[M+H]^+$ m/z = 116, found 116.

De-methyl RIF (**1**)[123,124]. 1-Nitrosopiperazine 230 mg (2 mmol) was dissolved in 2 ml of THF and was then added slowly to a suspension of $LiAlH_4$ (216 mg, 6 mmol) in 10ml THF under N_2 at 0 °C. The mixture was stirred for 5 min and then heated to reflux for 3 h. The cooled reaction mixture was quenched by MeOH until no further bubbles were formed, concentrated *in vacuo* and filtered. The resulting filter cake was washed with MeOH, and the combined filtrate was evaporated to dryness, yielding crude 1-aminopiperazine as a solid. *p*-Toluenesulfonic acid (5 mg), 10 ml dry THF and 140 mg 3-formyl-rifamycin (0.2 mmol) were then added with molecular sieves to the crude 1-aminopiperazine. The reaction mixture was stirred at room temperature overnight, filtered and concentrated *in vacuo*. The crude product was purified by column chromatography with silica gel using 5% $MeOH/CH_2Cl_2$ as the mobile phase. The product was a red solid and the yield was 78%. ^{1}H-NMR (600 MHz, $CDCl_3$) δ: 13.15 (s, 1H), 12.01 (s, 1H), 8.30 (s, 1H), 6.57 (dd, *J* = 15.6, 11.4 Hz, 1H), 6.38 (d, *J* = 11.4 Hz, 1H), 6.20 (d, *J* = 12.6 Hz, 1H), 5.93 (dd, *J* = 15.6 Hz, 4.8 1H), 5.10 (dd, *J* = 12.6, 6.6 Hz, 1H), 4.94 (d, *J* = 10.8 Hz, 1H), 3.77 (d, *J* = 9.0 Hz, 1H), 3.47 (d, *J* = 6.6 Hz, 1H), 3.11-3.14 (m, 2H), 3.05-3.06 (m, 2H), 3.04 (s, 3H), 3.01-3.03 (m, 2H), 2.97-3.01 (m, 2H), 2.97-3.06 (m, 1H), 2.33-2.41 (m, 1H), 2.22 (s, 3H), 2.08 (s, 3H), 2.06 (s, 3H), 1.79 (s, 3H), 1.69-1.72 (m, 1H), 1.51-1.56 (m, 1H), 1.33-1.38 (m, 1H), 1.01 (d, *J* = 7.2 Hz, 3H), 0.88 (d, *J* = 7.2 Hz, 3H), 0.60 (d, *J* = 6.6 Hz, 3H), -0.30 (d, *J* = 6.6 Hz, 3H). ^{13}C-NMR (100 MHz, $CDCl_3$) δ 195.12, 174.32, 171.91, 169.50, 169.36, 147.85, 142.60, 142.54, 138.68, 135.02, 134.19, 129.31, 123.18, 120.29, 118.50, 117.87, 112.89, 110.85, 108.74, 106.04, 104.44, 94.39, 77.20, 76.87, 76.77, 74.41, 70.62, 57.09, 53.43, 51.48, 44.82, 39.56, 38.59, 37.55, 33.43, 21.55, 20.80, 17.83, 10.96, 9.02, 8.57, 7.65. ESI-MS calculated for $[M+H]^+$ m/z = 809, found 809. Chemical purity was determined by reverse-phase analytical HPLC using a Phenomenex, Luna C-18, 250×4.6, 5 μm column operated at 1 ml/min flow rate using a mobile phase of 32% MeCN/68% H_2O.

Radiosynthesis of [^{11}C]RIF

The synthesis of [^{11}C]RIF was performed using **1** as precursor. A solution of precursor (1.0 mg, 1.2 μmol) was dissolved in 0.1ml MeCN and 0.2 ml DMSO with 0.2 mg K_2CO_3. After [^{11}C]CH_3I was purged into the solution and trapped, the reaction vessel was sealed and heated at 110°C for 10 min in an oil bath. The reaction mixture was diluted with 1 ml of aqueous ammonium formate (0.1M) prior to loading onto a semi-preparative HPLC column. HPLC purification was performed using a reverse phase C-18 column

(Phenomenex, Luna C-18 250×10, 5 µm), at a 5 ml/min flow rate with a mobile phase consisting of 35% MeCN/65% aqueous ammonium formate (0.1 M). The product was collected at the expected retention time (17 min), mixed with 100 mg ascorbic acid, and the solvent was removed by rotary evaporation. After dilution with 4 ml saline, the solution was filtered through an Acrodisc 13-mm Syringe Filter with 0.2 µm Supor membrane (Pall Corporation, Ann Arbor, MI) into a sterile vial for delivery. Radiochemical purity was determined by reverse-phase analytical HPLC using a Phenomenex, Luna C-18, 250×4.6, 5 µm column operated at 1 ml/min flow rate using a mobile phase of 35% MeCN/65% 0.1 M aqueous ammonium formate. Subsequently, purity was verified using TLC (15% MeOH/85% CH_2Cl_2) by co-spotting the labeled product with a standard.

Radiosynthesis of [^{11}C]INH

The synthesis of [^{11}C]INH was performed using **2** as the precursor. The precursor (1.0 mg), K_{222} (0.2 mg) and tetrakis(triphenylphosphine)palladium(0) (2.0 mg) was placed in a vial with 0.2 ml DMSO and heated until all the solid dissolved. This solution was then added to [^{11}C]HCN that had been purged and trapped in 0.1 ml DMSO, and the reaction mixture was sealed and heated at 135°C for 5 min. Water (0.3 ml), hydrazine monohydrate (0.3 ml) and NaY zeolite (20 mg) were then added, and after heating for 5 min at 135 °C, acetic acid (0.1 ml) was added. Following an additional 5 min at 135 °C, the reaction mixture was filtered through celite and the reaction vessel was washed with 0.5 ml water prior to injection onto the semi-preparative HPLC column. HPLC purification was performed using a reverse phase PFP column (Phenomenex, Luna PFP(2) 250×10, 5 μm) at a 5 ml/min flow rate with a gradient elution: 0-5 min, 100% water; 5-20 min from 100% water to 20% MeCN/80% water. The product was collected at the expected retention time (12 min), and the solvent and the majority of hydrazine coeluted was removed by ~10 min rotary evaporation. After dilution with 4 ml saline, the solution was filtered through an Acrodisc 13-mm Syringe Filter with 0.2 μm Supor membrane (Pall Corporation, Ann Arbor, MI) into a sterile vial for delivery. Radiochemical purity was determined by reverse-phase analytical HPLC using a Phenomenex, Luna PFP, 250×4.6, 5 μm column operated at 1 ml/min with a gradient of 0% to 20% MeCN in water over 20 min. Subsequently, purity was verified using TLC (25% MeOH/75% CH_2Cl_2) by co-spotting the labeled product with a standard.,

Quantification of hydrazine in the final formulated solution was determined by the modification of a published procedure[95]. Briefly, an aliquot (20 μl) of saline formulated solution was added to a test tube containing 20 μl H_2SO_4 solution (0.1 M) and 20 μl of benzaldehyde in methanol (1 ml benzaldehyde/100 ml methanol). Additional 40 μl sodium borate solution (0.01 M) and 20 μl methanol was added to the previous mixture and 25 μl of this new solution was injected into HPLC. The concentration of hydrazine was calculated based on the UV absorption (313 nm) of hydrazone and the standard curve. A blank sample (INH standard without hydrazine) was also analyzed which confirmed that INH did not interfere with the detection of hydrazine.

Radiosynthesis of [^{11}C]PZA

The synthesis of [^{11}C]PZA was performed using **5** as the precursor. The precursor (1.0 mg), K_{222} (0.2 mg) and tetrakis (triphenylphosphine)palladium(0) (2.0 mg) was placed in a vial with 0.2 ml DMSO and heated until all the solid dissolved. This solution was then added to [^{11}C]HCN that had been purged and trapped in 0.1 ml DMSO, and the reaction mixture was sealed and heated at 135 °C for 5 min. K_2CO_3 (0.2 ml, 0.1 M) and H_2O_2 (0.1 ml, 30%) were then added, and after heating for 5 min at 135℃, the reaction mixture was diluted with 0.3 ml ammonium formate (0.025 M, 5% acetic acid) and filtered through celite. The reaction vessel was washed with 0.5 ml ammonium formate solution prior to injection onto the semi-preparative HPLC column. HPLC purification was performed using a reverse phase PFP column (Phenomenex, Luna PFP(2) 250×10, 5 μm) at a 5 ml/min flow rate with a mobile phase consisting of 2% MeCN/98% ammonium formate (0.025M, 5% acetic acid). The product was collected at the expected retention time (7 min), and the solvent was removed by rotary evaporation. After dilution with 4 ml saline, the solution was filtered through an Acrodisc 13-mm Syringe Filter with 0.2 μm Supor membrane (Pall Corporation, Ann Arbor, MI) into a sterile vial for delivery. Radiochemical purity was determined by reverse-phase analytical HPLC using a Phenomenex, Luna PFP, 250×4.6, 5 μm column operated at 1 ml/min using 3% MeCN/97% 0.025 M aqueous ammonium formate as the mobile phase. Subsequently, purity was verified using TLC (25% MeOH/75% CH_2Cl_2) by co-spotting the labeled product with a standard. .

PET Imaging and Data Processing

All animal experiments performed in this study were approved by the Brookhaven Institutional Animal Care and Use Committee. Four baboons were included in this study. Ketamine hydrochloride (10mg/kg) was administered intramuscularly as an anesthetic agent and anesthesia was further maintained with oxygen (800 ml/min), nitrous oxide (1500 ml/min) and isoflurane (Forane, 1-4%) during scanning. Two catheters were placed in a radial arm vein and the popliteal artery for [^{11}C]-labeled drug injection and arterial sampling, respectively. [^{11}C]-labeled drug was injected through the prior catheter and arterial blood was collected through the latter one as following time intervals: every 5 s for 2 min, then 2, 5, 10, 20, 30, 45, 60 and 90 min. During the PET scanning, heart rate, respiration rate, body temperature and pO_2 were monitored. Siemens HR+ (Siemens high-resolution, whole-body PET scanner with 4.5×4.5×4.8 mm resolution at the center of field of view) was used to perform dynamic PET scans for a total of 90 min with the following time frames in 3D mode: 1×10, 12×5, 1×20, 1×30, 8×60, 4×300, 8×450 s. Correction of attenuation was obtained by a transmission scan of a ^{68}Ge rod source prior to each PET scan. Six baboon studies were conducted with average injected doses for RIF, INH and PZA of 1.54 mCi, 4.38 mCi and 5.17 mCi respectively. Images were reconstructed by filtered back projection (FBP) and analyzed using AMIDE® software[125].

LogD and PPB Determination

LogD determination: A test tube containing 2.5 ml of octanol and 2.5 ml of phosphate buffer solution (pH 7.4) was mixed with ~50 μl aliquot of formulated [^{11}C]-labeled drug by vortex for 2 min followed with centrifugation for 2 min to ensure full separation of the aqueous and organic phases. An aliquot from the octanol layer (0.1 ml) and aqueous layer (1 ml) were collected for radioactivity measurement. An additional 2.0 ml aliquot of the octanol layer was carefully transferred to a new test tube containing 0.5 ml octanol and 2.5 ml phosphate buffer (pH 7.4) and the previous procedure (vortex mixing, centrifugation, sampling, and transfer) was repeated for an additional five times to obtain six sets of samples. A well counter (Picker, Cleveland, OH) was used to measure radioactivity in each set of samples and the logD value of each sample was calculated by the following equation:

logD = log (decay-corrected radioactivity in octanol layer × 10/decay-corrected radioactivity in phosphate buffer layer).

PPB determination: A 10 μl aliquot of the formulated [^{11}C]-labeled drug was mixed with a sample of baboon plasma (0.8 ml, collected from at least 4 different baboons and pooled) by gently inverting several times. The mixture was incubated for 10 min at room temperature and then a 20 μl aliquot was taken to determine the total radioactivity in the plasma sample (A_T; A_T=A_{bound}+$A_{unbound}$). An additional 0.2 ml aliquot of plasma was placed in the upper level of a centrifree® tube (Amicon, Inc., Beverly, MA) and then the tube was centrifuged for 10 min. After discarding the upper part of the Centrifree tube, a 20 µl aliquot from the bottom part of the tube was taken to determine the amount of radioactivity that passed through the membrane ($A_{unbound}$). PPB was calculated by the following equation: % unbound = $A_{unbound} \times 100/A_T$

Metabolite analysis

Several aliquots (~0.2 ml each) of baboon plasma sample were collected at various time points during the PET study. Each sample was counted and added to a solution of unlabeled standard (20 µl of a 1 mg/ml solution) in MeCN (0.3 ml). The resulting solution was vortexed and centrifuged and the supernatant was collected. After mixing with 0.3 ml water, the supernatant was analyzed by HPLC using the following conditions: RIF, Waters µbondapak C-18 3.9×300 mm column with eluents 70% MeCN/30% 0.1 M aqueous ammonium formate at 1.0 ml/min using UV (254 nm) and radio-detection; INH, Phenomenex spherisorb ODS(2) 4.6×300 mm, 5 µm column with eluents 2% MeCN/98% 0.02 M aqueous heptane sulfonic acid at 1.0 ml/min using UV (254 nm) and radio-detection; PZA, Phenomenex spherisorb ODS(2) 4.6×300 mm, 5 µm column with eluents 10% MeCN/90% 0.01 M aqueous potassium phosphate (pH 5.2) at 1.7 ml/min using UV (254 nm) and radio-detection. The percent of unmetabolized radiotracer was determined as the ratio between the fraction of radioactivity coeluting with the unlabeled standard and the total radioactivity from the HPLC column.

Chapter 3

Radiosynthesis and Bioimaging of Enoyl-ACP Reductase Inhibitors in Rodents and Baboons

Introduction

FabI, the enoyl-ACP reductase encoded by the *fabI gene*, is responsible for the reduction of the double bond of the growing fatty acid acyl chain and shows a very high structural similarity across different bacterial species (**Figure 3.1**). This enzyme is a component of the type II fatty acid biosynthesis pathway (FASII pathway) in which fatty acids are generated through rounds of elongation. These fatty acids are essential for the construction of the bacterial cell wall, and FabI is an attractive target for the development of novel drugs against various diseases, including Staph infection and Tuberculosis (TB)[126-128].

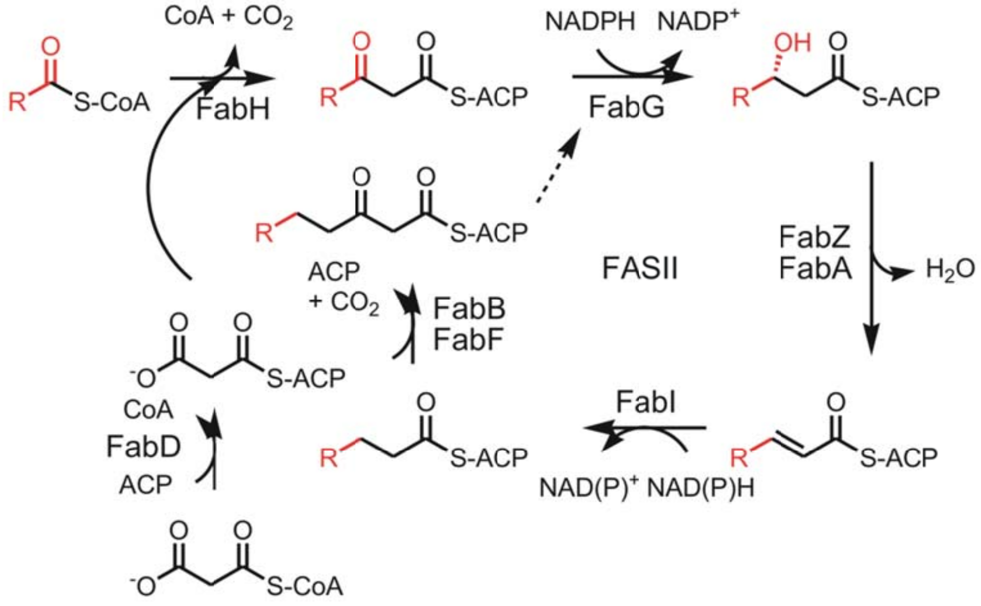

Figure 3.1 The FASII pathway

The causative pathogen for staph infection is *Staphylococcus aureus (S. aureus)*, which is also known as golden staph. It is estimated that 20% of the human population a long-term carrier of *S. aureus*[129]. The emergence of antibiotic-resistant strains, such as methicillin-resistant *S. aureus* (MRSA) and vancomycin-resistant *S. aureus* (VRSA), raises challenges for chemotherapy and stresses the need for new antibiotics with novel mechanisms of action[127,130]. Although staph infections are generally presented on the surface of the skin, *S. aureus* are able to disseminate via the blood stream or through surgical process into other organs[131-133]. In particular, *S. aureus* can also invade deeper into kidney and heart, which are the two common sites of organ infection[134,135]. Moreover, *S. aureus* infection in the brain, which is termed *S. aureus* meningitis, has high mortality rates, although the incidence is low. The treatment of drug-resistant *S. aureus* meningitis, such as infection caused by MRSA or VRSA, is even more complicated since treatment is limited to drugs that are able to penetrate the blood-brain barrier (BBB). The standard treatment for MRSA meningitis is difficult to establish as there is a lack of techniques that are able to assess drug concentration inside the human brain tissue[136,137].

Mycobacterium Tuberculosis (Mtb) is the causative agent of TB, an infectious disease that is carried by one third of the world's population and that is responsible for 2 million deaths each year[84-86]. The most common site of TB infection are the lungs as the primary route of infection is through inhalation of live bacteria. A more severe Mtb infection, in the form of tuberculous meningitis, cerebral tuberculomas or spinal TB, can occur in the brain and is called CNS TB[89]. Current treatment for CNS TB normally follows the same format as that used for treating pulmonary TB. Consequently, information about drug distribution in the brain would be helpful to guide the development of new treatment regimes[89]. The emergence of multi-drug resistant TB (MDR-TB) and extremely drug-resistant TB (XDR-TB) contribute to the spread of infection and worsen the situation by either lengthening the treatment or invalidating current treatment, especially in the case of CNS TB. Therefore, drugs with novel mechanisms of action are urgently needed to control the spread of disease[128]. One of the front-line TB treatments is isoniazid (INH), which is a prodrug that has to be activated by KatG, the mycobacterial catalase-peroxidase, to form the active inhibitor INH-NAD adduct[119]. Since isoniazid resistance occurs primarily from mutations in KatG[138], inhibitors of InhA that do not require activation should be active against isoniazid-resistant strains of Mtb[139]. Thus a series of sub-nanomolar diaryl ether inhibitors of FabI that are active against Mtb has been developed (**Scheme 3.1**)[139-142]. As the FabI has structural similarity across different bacterial species, those inhibitors demonstrated potent activity against a broad spectrum of bacteria, including *S. aureus* and *Francisella tularensis* (**Scheme 3.1**)[143,144].

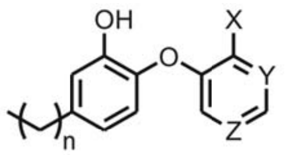

5-Alkyl-Aryl-Ethers. n=0-8
X=F,Cl,Br,CH_3,CN,NH_2
Y=Z=C,N

Scheme 3.1 Structure of diaryl ether inhibitors

While most drug discovery program measures plasma pharmacokinetics (PK) and compares the plasma concentration with corresponding MIC values, there is a growing appreciation that the distribution of antibiotics in the tissue of interest is a more critical determinant and predictive factor for activity[7,8]. This is because most drugs exert their bactericidal effects at the site of infection rather than in the plasma, and because drug equilibration between plasma and infection site cannot always be achieved[7,8]. In addition, bacterial resistance emerges if optimal drug concentration at the site of infection was not reached, and the regime would lengthen and the cost would increase[8,128]. Therefore, the tissue distribution of drugs at the site if infection is required by the Food and Drug Administration (FDA) for clinical studies[8].

Positron Emission Tomography (PET) is a powerful non-invasive method to map the three-dimensional distribution of drugs over time. In addition, the methodology developed for imaging drug distribution in laboratory animals using PET can be readily translated to humans[15]. Here, we report using PET to evaluate the tissue distribution of two potent FabI inhibitors, PT-70 (n = 5, X = CH_3, Y = Z = C) and PT-119 (n = 5, X = CN, Y = Z = C) that inhibit the FabI enzymes from *S. aureus* (saFabI) and TB (InhA) (**Table**

3.1). Both inhibitors have been radiolabeled and the biodistribution of the labeled drugs has been imaged in baboons *in vivo*. It is estimated that the concentrations of PT-70 and PT-119 in the lungs are at least 10 times higher than the MIC values for each compound against MTB. In addition, as AUC/MICs are likely the driver of the efficacy for those two compounds, we calculated $AUC_{0\text{-}90min}$/MIC for both PT-70 and PT-119. The $AUC_{0\text{-}90min}$/MIC for PT-70 and PT-119 are 51% and 14% of the $AUC_{0\text{-}90min}$/MIC for INH, respectively, which suggests that PT-70 is a better candidate than PT-119 to treat pulmonary TB infection in non-human primates and humans. In addition, the estimated inhibitor concentration in the heart and kidneys are at least 20 times higher for PT-70 and 100 times higher for PT-119 than the MIC values of these compounds against *S. aureus*. The $AUC_{0\text{-}90min}$/MIC for PT-119 is 16368 min and 51023 min for heart and kidney, respectively, and both are ~3 times higher than the values for PT-70. The results suggest that PT-119 is better candidate than PT-70 to treatment *S. aureus* infection in the heart and kidney. The ability of the PT-70 and their radiolabeled metabolites to penetrate the blood-brain barrier is similar to INH, while the ability of PT-119 is two times higher than INH. It is estimated that the concentrations of PT-70 and PT-119 in the brain are at least 10 times higher than their MIC values against TB. The $AUC_{0\text{-}90min}$/MIC are 38% and 37% of INH $AUC_{0\text{-}90min}$/MIC for PT-70 and PT-119 respectively, which suggests that PT-70 and PT-119 are potential candidates for treatment of CNS TB. For *S. aureus* infection, PT-119 had an $AUC_{0\text{-}90min}$/MIC value in the brain that was 10 times higher than that for PT-70, and it is clear that PT-119 is a superior candidate for the treatment of *S. aureus* meningitis. These studies provide the first tissue distribution of PT FabI inhibitors in non-human primates, and will facilitate antibiotic discovery program, particularly to the CNS TB and *S. aureus* meningitis indication of treatment.

Table 3.1 Activity of PT-70 and PT-119 against FabIs and Bacteria.

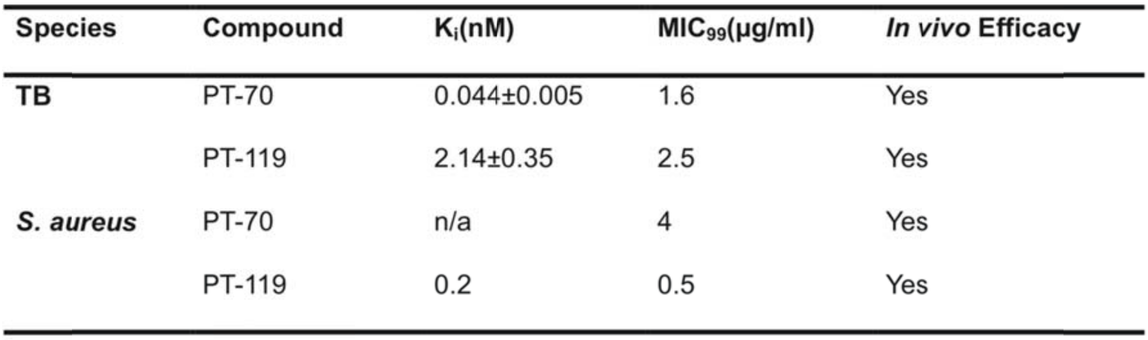

Species	Compound	K_i(nM)	MIC_{99}(μg/ml)	*In vivo* Efficacy
TB	PT-70	0.044±0.005	1.6	Yes
	PT-119	2.14±0.35	2.5	Yes
S. aureus	PT-70	n/a	4	Yes
	PT-119	0.2	0.5	Yes

Result and Discussion

Organic Synthesis

The synthesis of precursors **7** and **8** was adopted from methods developed internally by another graduate student in the lab (Pan Pan) without optimization (**Scheme 3.2**) (unpublished data). Briefly, compound **3** was prepared from commercially available vanillin through three steps. Vanillin was protected with a benzyl group and coupled with a hexyl chain using a Wittig reaction to form compound **2**[145]. Reduction of compound **2** with hydrogen generated compound **3**. Compound **4** was synthesized by nucleophilic aromatic substitution of **3** with 1-fluoro-2-nitrobenzene, and was converted to compound **5** by reduction with H_2 catalyzed by palladium on charcoal. Compound **6** was prepared from **5** by utilizing the Sandmeyer reaction, which went through a diazonium salt intermediate prior to iodide anion attack[146]. The deprotection was carried out with tribromoborane in dichloromethane to form **7**, and compound **8** was prepared with additional treatment of tributylchlorostannane on **7** under strong basic condition in diethyl ether.

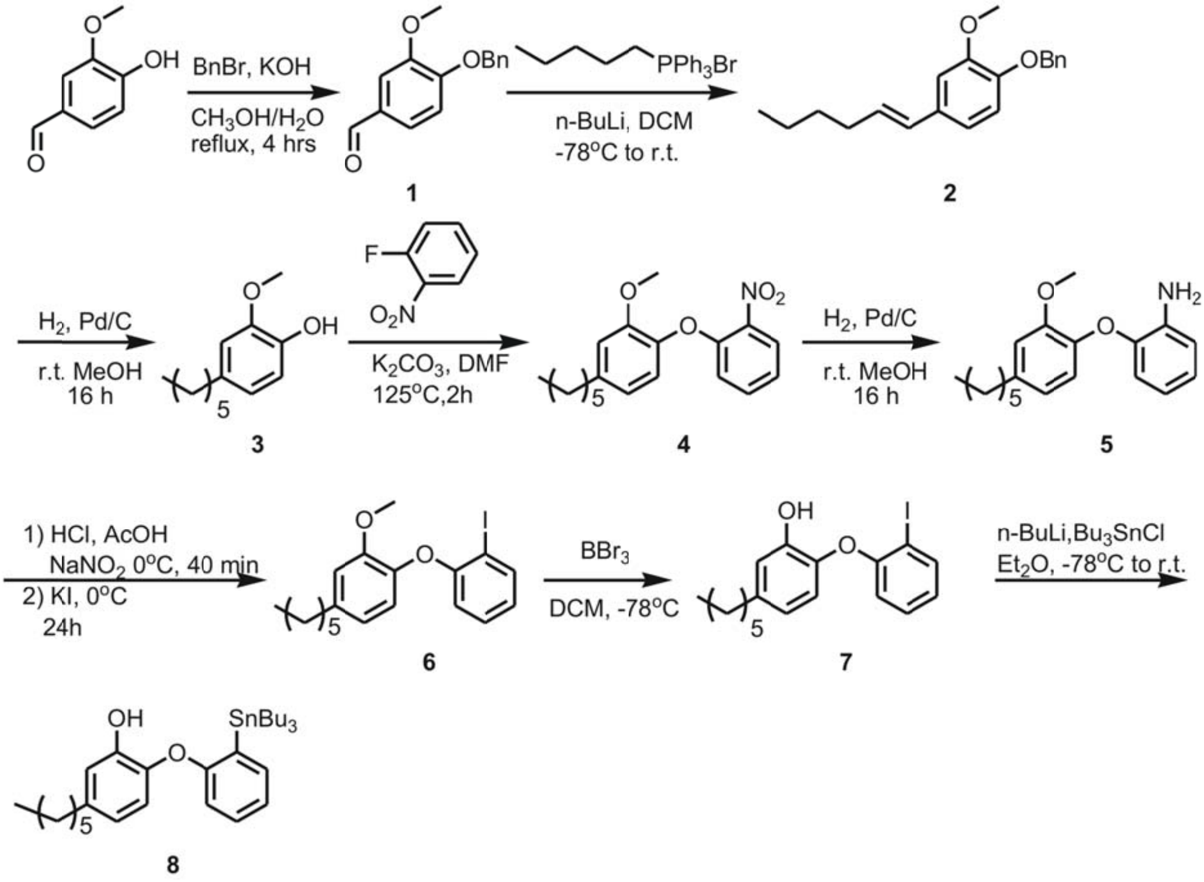

Scheme 3.2 Synthesis of precursors for [^{11}C]PT-70 and [^{11}C]PT-119

Radiosynthesis

Radiosynthesis of [^{11}C]PT-70

The radiosynthesis of [^{11}C]PT-70 was accomplished by using the modified Stille reaction using precursor **8** as shown in **Scheme 3.3**[67]. Initially, the reaction was successfully carried out in toluene at 100°C for 10 min. However this involved a time consuming evaporation procedure before the chromatographic purification due to incompatible solvents and consequently we explored a range of solvent systems in order to identify conditions that would give the required rate, radiochemical yield and solvent compatibility. This screening approach resulted in the use of THF as the solvent with a 5 min reaction time (**scheme 3.3**). This reaction was also tolerant of the phenol group and no major side reactions were observed. The [^{11}C]PT-70 was subsequently purified by high performance liquid chromatography (HPLC) and concentrated *in vacuo*. The average decay-corrected yield (DCY), calculated from [^{11}C]CH_3I, was 40%-50% in a total synthesis time of 50 min. Analytical HPLC and TLC demonstrated that the radiolabeled product was over 98% radiochemically pure, with a specific activity of 7-13 Ci/µmol at the end of bombardment (EOB).

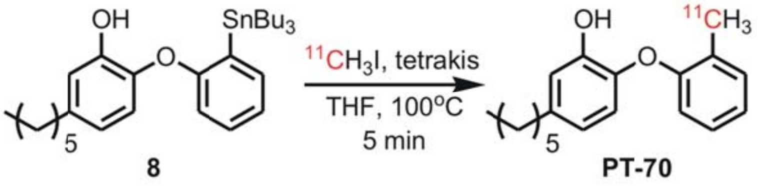

Scheme 3.3 Radiosynthesis of [^{11}C]PT-70

Radiosynthesis of [^{11}C]PT-119

The radiosynthesis of [^{11}C]PT-119 was accomplished by a one step tetrakis(triphenylphosphine)palladium(0) catalyzed cyanation (**Scheme 3.4**). This method was adopted from the previously reported radiolabeling of an aromatic ring with [^{11}C]HCN[80], and involved treating **7** with [^{11}C]HCN in a DMSO reaction mixture for 5 min at 135°C. The reaction mixture was subsequently purified by HPLC and fractions from the HPLC were concentrated *in vacuo* to generate the dry product. Analytical HPLC and

TLC demonstrated that the radiolabeled product was over 98% radiochemically pure, with a specific activity of 0.5-0.8 Ci/μmol at the EOB.

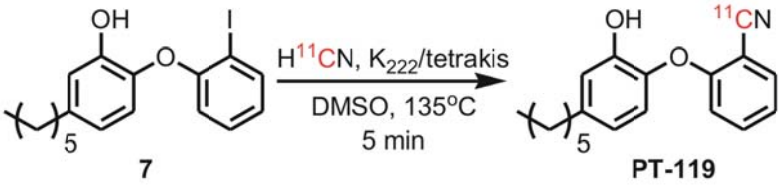

Scheme 3.4 Radiosynthesis of [^{11}C]PT-119

LogD and plasma protein binding (PPB)

The lipophilicity (logD) and PPB of each radiolabeled drug was determined using the radiolabel to report on drug concentration. The results are presented in **Table 3.2**, and the logD is lower than the calculated logD.

Table 3.2 LogD and PPB determination

	LogD	PPB[1]
PT-70	3.65	99.76 %

[1] Value expressed as % of free fraction in plasma.

Brain PET imaging in anesthetized baboons

PET imaging studies were performed with [^{11}C]PT-70 and [^{11}C]PT-119 to determine the brain penetration and distribution. Images were acquired for 90 min following i.v. administration of each radiolabeled drug and time-activity curves (TACs) (**Figure 3.2a**) were generated from the imaging data and the region-of-interests (ROIs) were drawn manually[80]. Time-concentration curves (TCCs) in **Figure 3.2b** were produced by a linear extrapolation of estimated concentration of each compound in µg/ml assuming 50 mg/kg dose and 20 kg baboon, while dose corrected coronal images (**Figure 3.2c**) were generated by sum from 15 to 90 min. The area under the curve values (AUCs) were produced by integrating the concentration-time curve as a function of time. $AUC_{0-90min}$/MIC values, which are a critical predictor of *in vivo* efficacy, are given in **Table 3.3** where they are compared with the corresponding value for INH from similar PET studies[80].

Table 3.3 AUC$_{0\text{-}90min}$ and AUC$_{0\text{-}90min}$/MIC values for PT70 and PT119 in the Brain using the MIC values for Mtb and *S. aureus*[1]

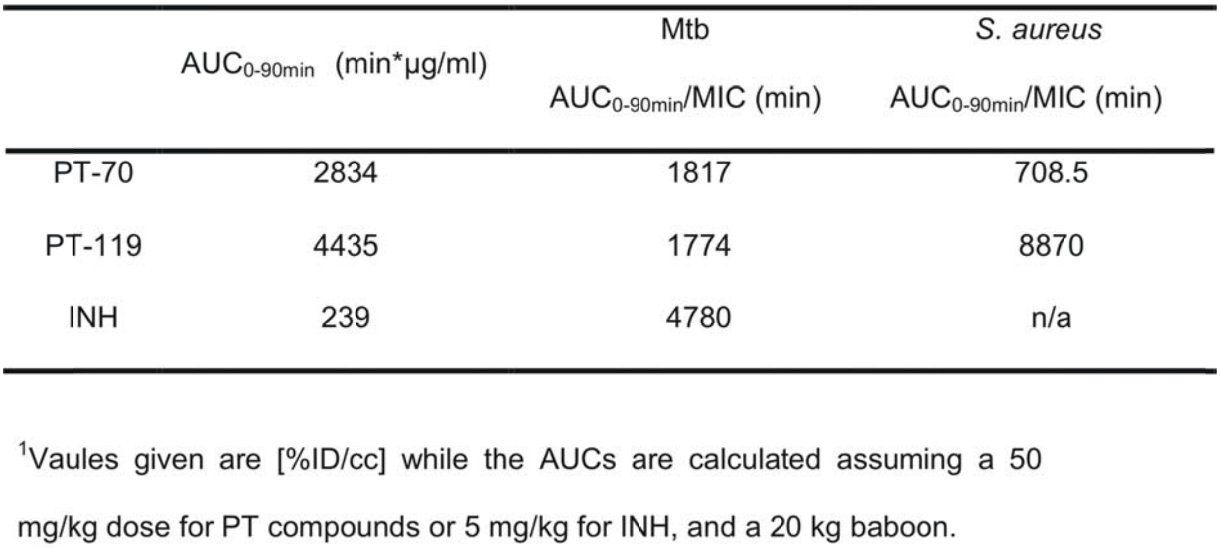

	AUC$_{0\text{-}90min}$ (min*µg/ml)	Mtb	*S. aureus*
		AUC$_{0\text{-}90min}$/MIC (min)	AUC$_{0\text{-}90min}$/MIC (min)
PT-70	2834	1817	708.5
PT-119	4435	1774	8870
INH	239	4780	n/a

[1] Vaules given are [%ID/cc] while the AUCs are calculated assuming a 50 mg/kg dose for PT compounds or 5 mg/kg for INH, and a 20 kg baboon.

To our knowledge, these PET studies are the first in which TB drug candidates have been measured in whole brain tissue in a living non-human primate. **Figure 3.2** clearly demonstrates that the ability of the compounds and their radiolabeled metabolites to penetrate the BBB decreases in the order PT-119 > PT70 > INH, although PT-70 and INH only differ slightly. The unit % of injected dose per cubic centimeter (%ID/cc) was used and the concentration in µg/ml was estimated based on the weight of baboons (20 kg), the recommended daily dose of PT-70 (50 mg/kg, which was selected based on no toxicology study in mouse, unpublished data) and the assumption that the positron signal derives primarily from the intact drug. Thus, for a 20 kg baboon the injected dose is 1,000 mg for PT-70. For example, at 30 min the concentration of PT-70 in the brain is estimated to be 0.0035% of 1,000 mg which is 35 µg/ml. The anticipated concentration of PT-70 in the brain is therefore over 10 times above the Mtb MIC for this compound (**Figure 3.2b**) through the study time frame, supporting the candidacy of PT-70 for CNS

TB infection treatment. In addition, the $AUC_{0\text{-}90min}$/MIC value of PT-70 is about 38% of the value for INH, which provides further indication of the efficacy of PT-70 against TB. Moreover, although PT-70 is less active against *S. aureus* as the MIC is ~2.5 times larger and $AUC_{0\text{-}90min}$/MIC is less attractive than the one for Mtb, the estimated concentration in the brain is still over 5 times above the *S. aureus* MIC, which suggests that this compound has sufficient potency for treatment of *S. aureus* meningitis.

The [^{11}C]PT-119 TAC, TCC (**Figure 3.2**) showed a higher brain penetration and accumulation when compared to PT-70. The activity of injected [^{11}C]PT-119 in the whole brain was monitored after iv administration (**Figure 3.2**) and the estimated concentration in µg/ml has been calculated based on the same assumptions as those described above. Therefore, the calculated PT-119 concentration is more than 10 times above the MIC of this compound against Mtb (**Figure 3.2b**), and hence PT-119 should be a good candidate for the treatment of CNS TB infection. Moreover, the $AUC_{0\text{-}90min}$/MIC value of PT-119 is similar to the value of PT-70, and about 39% of the value of INH. Taken together with the efficacy of INH in CNS TB treatment, it is clear that PT-119 would be a promising candidate for CNS TB treatment. In the meanwhile, the predicted potency against *S. aureus* meningitis is 5 times better than that for CNS TB based on the $AUC_{0\text{-}90min}$/MIC, and over 10 times better than the potency of PT-70 against *S. aureus* meningitis. The estimated concentration in the brain is over 80 times above the *S. aureus* MIC through the study time frame. Taken together, the biodistribution studies suggest that PT-119 is a highly promising candidate for the treatment of *S. aureus* meningitis.

Vancomycin is commonly prescribed for MRSA meningitis and administered through iv infusion or intraventricular instillation[147,148]. Although the peak concentration in CSF reached almost 300 μg/ml with intraventricular injection of a 10 mg dose, it was difficult to reach above 6 μg/ml with iv administration [149]. It is also known that higher AUC/MIC values of vancomycin correlated with better treatment outcome, although other PK/PD correlation was proposed[150]. Given a 1 μg/ml MIC against *S. aureus* and a peak concentration of less than 6 μg/ml in CSF, the calculated $AUC_{0\text{-}90min}$/MIC would be less than 540 min, which is significantly lower than the estimated $AUC_{0\text{-}90}$/MIC for PT-70 and PT-119. Another common prescription for *S. aureus* meningitis is linezolid, which is considered to be effective if $AUC_{0\text{-}24h}$/MIC value is over 100 hrs (2,400 min)[151]. As the $AUC_{0\text{-}90}$/MIC for PT-70 and PT-119 are 708 and 8870 min (**Table 3.3**) it is likely that $AUC_{0\text{-}24h}$/MIC would be larger than 2,400, at least for PT-119, which further suggests that both compounds may be active against *S. aureus* meningitis.

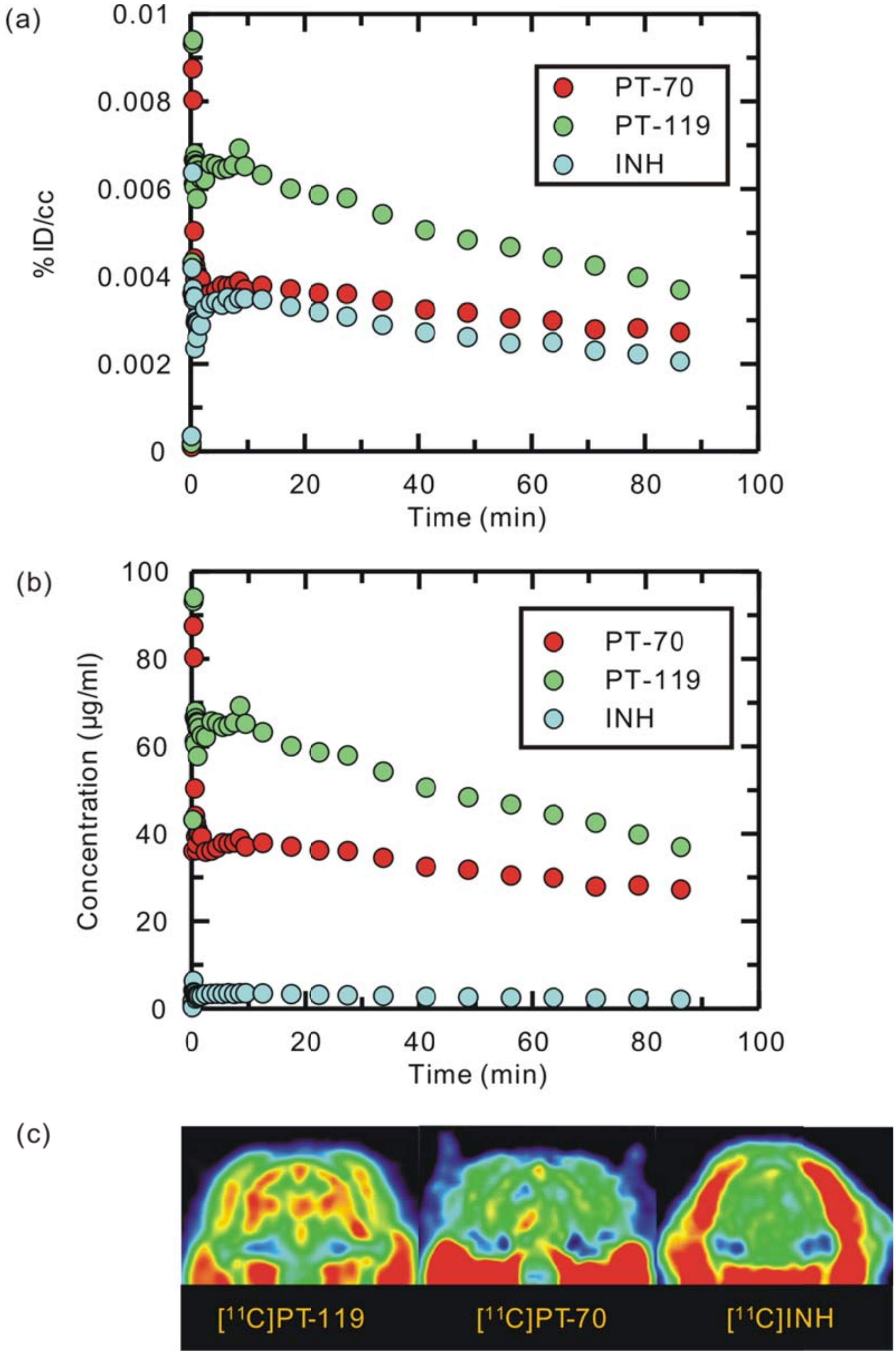
(a)
%ID/cc
0.01
0.008
0.006
0.004
0.002
0
0
20
40
60
80
100
Time (min)
PT-70
PT-119
INH
(b)
Concentration (μg/ml)
100
80
60
40
20
0
0
20
40
60
80
100
Time (min)
PT-70
PT-119
INH
(c)
[11C]PT-119
[11C]PT-70
[11C]INH

Figure 3.2 Blood-brain barrier penetration, TACs and TCCs for [^{11}C]PT-119, [^{11}C]PT-70 and [^{11}C]INH.

(a) TACs generated from the image acquired after iv administration of each compounds in baboons by manually drawing the ROIs. (b) TCCs calculated from TACs assuming a 50 mg/kg dosage and a 20 kg baboon. (c) Dose corrected coronal images summed over 15-90 min. The NIH color scale was used to represent relative radioactivity concentration.

Torso PET imaging in anesthetized baboons

PET imaging studies were performed with [^{11}C]PT-70 and [^{11}C]PT-119 to determine their peripheral organ distributions. The TACs (**Figures 3.3 and 3.4**) were generated from the images acquired after i.v. administration of each drug to baboons by manually drawing the ROIs, and the TCCs in the lung were estimated the same way as that described earlier for the brain.

[^{11}C]PT-70 was administered iv and monitored over the 90 min dynamic PET scan. The injected [^{11}C]PT-70 cleared rapidly from the heart, lung and blood, with moderate accumulation in liver and kidney, while a large portion of radioactivity accumulated in the gallbladder (**Figure 3.3**). The rectilinear scan at around 120 min after administration suggests that another large portion of the injected [^{11}C]PT-70 was eliminated into the bladder. The estimated concentration of PT-70 in the lung is more than 50 times above the Mtb MIC for this compound over the scan period, and hence PT-70 should be a suitable candidate for pulmonary TB infection. In addition, the $AUC_{0\text{-}90min}$/MIC of PT-70 is 51% of the value for INH ($AUC_{0\text{-}90min}$/MIC = 13040 min) **(Table 3.4)**, which further supported the potential of PT-70 drug candidacy. The radioactivity in the organs was higher than values observed in plasma, which confirms that differences exist between drug concentrations in plasma and in organs, and demonstrates that there is a need to measure the compound concentration at the site of infection. The penetration of radioactivity into the heart and kidney, the common sites of severe infection of *S. aureus*, is higher than lung, and the estimated $AUC_{0\text{-}90min}$/MIC values are 5023 min and 18126 min (**Table 3.4**).

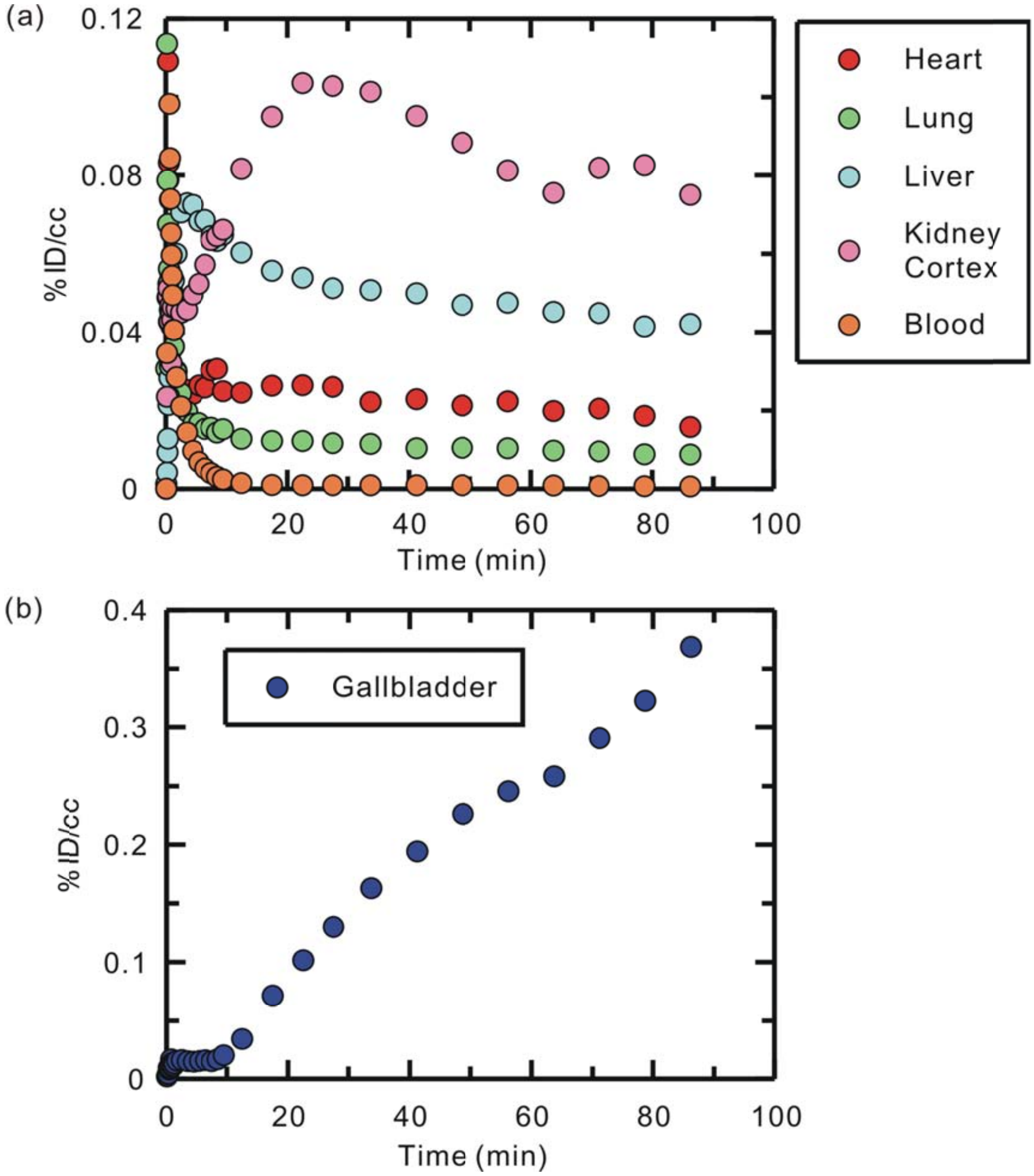

Figure 3.3 TACs for [11C]PT-70 in the (a) heart, lungs, liver, kidneys, blood and (b) gallbladder.

Table 3.4 $AUC_{0\text{-}90min}$ and $AUC_{0\text{-}90min}$/MIC in Lung[1]

	PT-70		PT-119	
	AUC$_{0\text{-}90min}$ (min*μg/ml)	AUC$_{0\text{-}90min}$/ MIC (min)	AUC$_{0\text{-}90min}$ (min*μg/ml)	AUC$_{0\text{-}90min}$/ MIC (min)
Lung (Mtb)	10376	6651	4464	1785
Heart (S. aureus)	20092	5023	8184	16368
Kidney (S. aureus)	72507	18126	25511	51023

[1] Vaules given are [%ID/cc] while the AUCs are calculated assuming a 50 mg/kg dose for PT compounds or 5 mg/kg for INH, and a 20 kg baboon.

The tissue distribution of [^{11}C]PT-119 administered iv is shown in **Figure 3.4**. The TCC has been estimated based on the method described earlier for the brain. The calculated PT-119 concentration in lung is more than 10 fold higher than the MIC of this compound against Mtb over the study time frame. [^{11}C]PT-119 and/or its radiolabeled metabolites rapidly penetrated the heart, lungs, liver and kidneys, and in all cases the tissue radioactivity of PT-119 exceeded the concentration in blood. The AUC$_{0\text{-}90min}$/MIC value for PT-119 is only 14% of that for INH and 27% of that for PT-70 **(Table 3.4)**, which suggests that PT-119 may not as effective for the treatment of pulmonary TB infection as PT-70. On the other hand, PT-119 has demonstrated promising AUC$_{0\text{-}90min}$/MIC values, which are over 3 times higher than the value for PT-70, in heart and kidney (**Table 3.4**) against *S. aureus*, although the penetrations are not as good as PT-70.

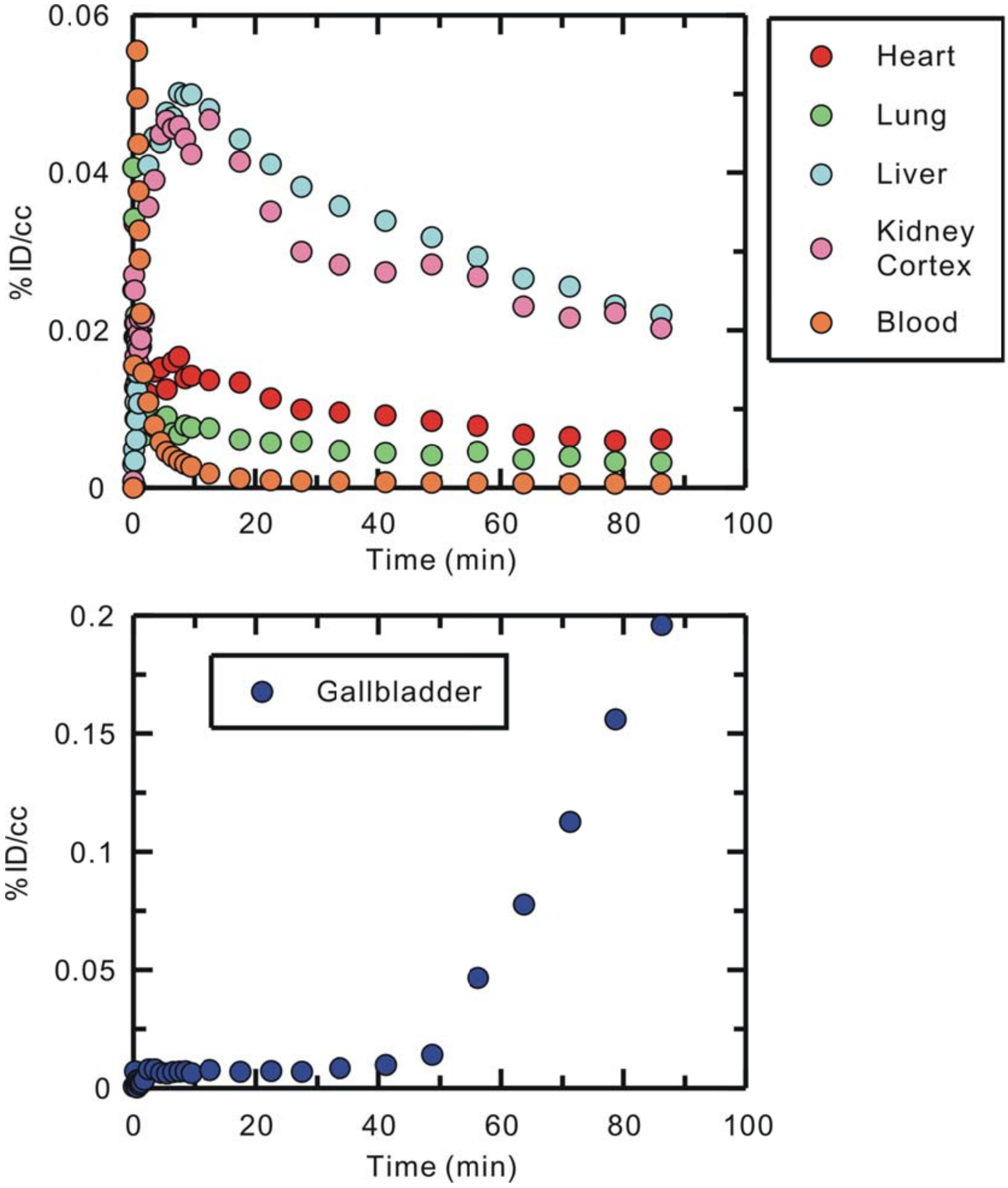

Figure 3.4 TACs for [^{11}C]PT-119 in the (a) heart, lungs, liver, kidneys, blood and (b) gallbladder.

The imaging experiments reported here in the present work were conducted using microdoses (1-10 µg) of compounds, and so the estimated PK for a therapeutic dose of drug was obtained by linear extrapolation. We are aware that drug distribution can change as a function of administered dose if one or more processes, such as transporters or metabolic enzymes that affect distribution, become saturated. However, based on the mechanism of action of these compounds together with the observation that no significant difference exists for tissue PK between microdose and therapeutic dose in mice (**Figure 4.3, Chapter 4**), we believe that saturable processes are not likely to play a major role in modulating distribution in tissues. In addition, we are also aware that the radioactivity signal may not come from the intact drug, especially in the case of liver and kidney, where the drugs are metabolized. The major route of metabolism of diaryl ether analogs is through glucuronidation at the phenol group, which does not remove the radiolabel from the parent compound[152]. Because of the addition of the glucuronic acid, however, the antibacterial properties of the compound are likely altered. Thus it is possible that we overestimate the penetration, $AUC_{0\text{-}90min}$, and $AUC_{0\text{-}90min}/MIC$, as part of the radioactivities may not represent the intact compounds. However, in other organs, especially in brain, we are confident that most of the signals are from intact drugs as metabolism is slow in those organs. The current studies in healthy baboons clearly demonstrate the utility of using PET imaging to determine the PK parameters and biodistribution of drug candidates non-invasively *in vivo* before the establishment of systematic toxicology information. In addition, these studies provide closer estimation of distribution in human than rodents. Eventually, this approach should facilitate the drug discovery process to treat TB infection and Staph infection, especially for disseminated forms of the disease such as CNS TB and *S. aureus* meningitis, where the compound concentration at the site of infection is difficult to measure. Because these compounds are able to penetrate tissues of various organs and efficacy has been demonstrated in animal models, we expect the radiolabeled compound would surround or accumulate within the bacteria. Given that these compounds have long residence time on their FabI targets, we hypothesize that these labeled compounds may be good candidates for localizing bacterial populations *in vivo*. Both PT-70 and PT-119 have long residence times, of 30 min and 90 min respectively, on the Mtb enoyl-ACP reductase InhA. Moreover, PT-119 also has a long residence time (100 min) on the *S. aureus* enoyl-ACP reductase, which suggests that this compound has the potential to locate and quantify *S. aureus* in addition to Mtb.

Conclusion

Two potent enoyl-ACP reductase inhibitors, with *in vitro* and *in vivo* activity against Mtb and *S. aureus*, have been radiolabeled with carbon-11 and the biodistribution of the labeled drugs has been imaged in baboons *in vivo*. These studies have elucidated the distribution of these compounds in the tissues of non-human primates and the results provide guidance for designing studies to assess efficacy in clinical trials. In addition, based on the $AUC_{0\text{-}90min}$ and $AUC_{0\text{-}90min}$/MIC, we can expect the efficacy of PT-70 and PT-119 towards each form of *S. aureus* and Mtb infection. Based on the weight of the baboon, a safe or standard drug dose, and the assumption that the signal derives primarily from the intact drug, it is estimated that the ability of PT-70 and their radiolabeled metabolites to penetrate the blood-brain barrier is similar to INH, while the ability of PT-119 is two times higher than INH. In addition, it is estimated that the $AUC_{0-90min}$/MIC values for PT-70 and PT-119 are 38% and 37% of the INH $AUC_{0-90min}$/MIC, respectively, which suggests that PT-70 and PT-119 have similar potential to treat CNS TB in non-human primates and humans. For *S. aureus* infection, PT-119 demonstrated 10 times higher $AUC_{0-90min}$/MIC value than that for PT-70 in the brain, and it is clear that PT-119 is a superior candidate for the treatment of *S. aureus* meningitis. For pulmonary TB infection, it is estimated that the $AUC_{0-90min}$/MIC values for PT-70 and PT-119 are 51% and 14%, respectively, of the INH $AUC_{0-90min}$/MIC, which suggests that PT-70 is a better candidate than PT-119. The estimated concentrations in heart and kidney are at least 20 times higher for PT-70 and 100 times higher for PT-119 than the MIC values against *S. aureus*. The $AUC_{0-90min}$/MIC for PT-119 is 16368 min and 51023 min for heart and kidney respectively, and both are ~3 times higher than the values for PT-70. The result suggested PT-119 is better candidate than PT-70 to treatment *S. aureus* infection in the heart and kidney.

Future Work

First, radiolabel another drug candidate, PT-161 (n = 5, X = F, Y = N, Z = C) with [^{18}F]F^{-}. The precursor has been synthesized with vanillin, and both compound **9** and **12** could be a good precursor for PT-161 (**Scheme 3.5**)

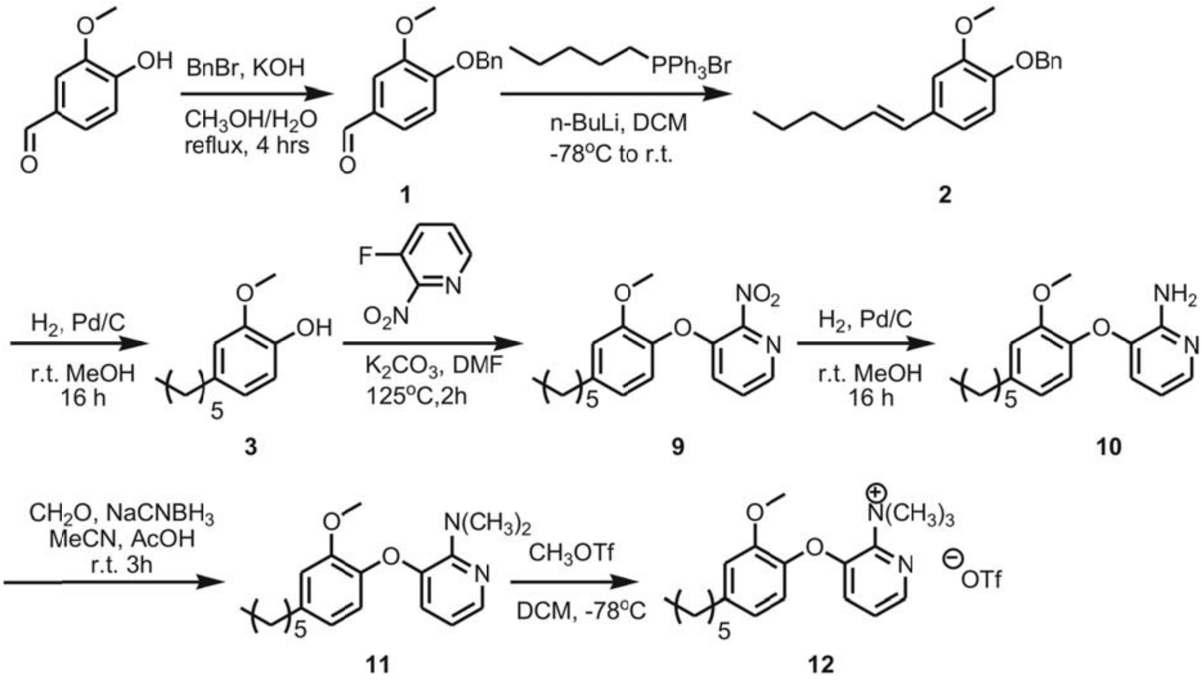

Scheme 3.5 Synthesis of precursors for [^{11}C]PT-161

The radiosynthesis of [^{18}F]PT-161 has been proposed in **scheme 3.6**[67], and efforts have been made to synthesize [^{18}F]PT-161, although step 1 hasn’t worked in my hand.

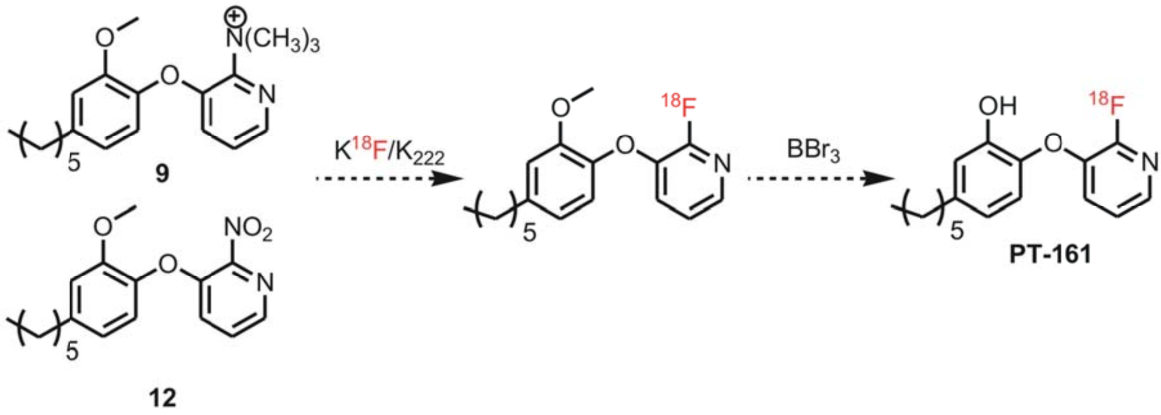

Scheme 3.6 Radiosynthesis of [^{18}F]PT-161

The two hypotheses are: 1) the phenol group is electron donating group, which make the nucleophilic aromatic substitution harder. 2) the large group on left ring provide steric hindrance to the reaction. In addition, the quality of compound **9** is another concern as the purification is difficult. Reported recrystallization conditions failed to provide crystals and column chromatography would not able to elute the charged compound. Although the crude product demonstrated >95% purity based on NMR, it is difficult to predict the effect of the small amount of impurity to the reaction, given the nmol scale of fluorine-18. Fortunately, another group member, Hui Wang, demonstrated to radiolabel PT-161 with compound **9** as precursor, and the second step has been tested with carbon-12 intermediate.

Second, we would like to search our pool of enoyl-ACP reductase inhibitors, and choose a new compound with better affinity, lower MIC, longer residence time and longer *in vivo* half-life. The metabolism of diaryl ether analog has been reported before, and the phase II glucuronidation was the major route to facilitate elimination [152]. The new group of inhibitors, 4-pyridinone aryl ether (**Scheme 3.7**), has demonstrated 10 times higher AUC than diaryl ether analog (unpublished data), and they are of particular interest for radiolabeling.

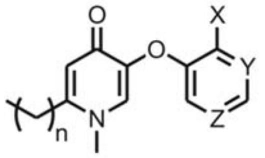

4-Pyridinone Aryl Ethers. n=0-8
X=F,Cl,Br,CH_3,CN,NH_2
Y=Z=C,N

Scheme 3.7 Structure of 4-pyridinone aryl ether

Experimental Section

Organic Synthesis

4-(Benzyloxy)-3-methoxybenzaldehyde (**1**)[153]

A solution of benzyl bromide (3.93 ml, 33 mmol) was added to the mixture of 4.56 g vanillin (30 mmol) in 50 ml MeOH and 1.85 g KOH (33 mmol) in 50 ml H_2O dropwise and the whole mixture was heated to reflux for 4 hrs. After the completion of reaction, the product was extracted with DCM and H_2O, and the aqueous layer was further washed with DCM. The combined DCM layers were dried with $MgSO_4$, and concentrated *in vacuo*. The crude product **1** was purified by automated column chromatography with silica gel using 5% ethyl acetate/petroleum ether as the mobile phase. The product was obtained as a white solid with a yield of 52%. ESI-MS calculated for $[M+H]^+$ m/z = 243, found 243.

1-((4-((E)-hex-1-enyl)-2-methoxyphenoxy)methyl)benzene (**2**)[154]

A solution of n-BuLi (2M solution in cyclohexane, 6.7 ml, 13.4 mmol) was added dropwise to an solution of n-Pentyltriphenylphosphonium bromide (13.4 mmol) in DCM at -78°C. After 30 min, 2.5 g of **1** (10.3 mmol) was added to the mixture before the cooling bath was removed, and the reaction mixture was stirred overnight. The reaction was subsequently quenched by slowly adding 1M HCl, after which the pH was adjusted to 7 using $NaHCO_3$ Solution. The aqueous layer was extracted with DCM twice and the combined organic layers were washed with brine before drying with $MgSO_4$. The crude product **2** was concentrated *in vacuo* prior to purification by automated column chromatography with silica gel using 5% ethyl acetate/petroleum ether as the mobile phase. The yield was 75%. ESI-MS calculated for $[M+H]^+$ m/z = 297, found 297.

4-Hexyl-2-methoxyphenol (**3**)[155]

Activated palladium on charcoal (200mg) was added to 50 ml MeOH solution of compound **2** (2.28 g, 7.8 mmol). The reaction mixture was stirred under hydrogen overnight and then filtered through celite. The crude product **3** in the filtrate was concentrated *in vacuo* and purified by automatic column chromatography with silica gel using 5% ethyl acetate/petroleum ether as the mobile phase. The product was a colorless liquid and the yield was 91%. ESI-MS calculated for $[M+H]^+$ m/z = 209, found 209.

1-(4-Hexyl-2-methoxyphenoxy)-2-nitrobenzene (**4**)[156]

A solution of 1.484 g compound **3** (7.1 mmol) and 2.9 g K_2CO_3 dissolved in 5 ml DMF was stirred for 10 min prior the addition of 1.303 g 1-fluoro-2-nitrobenzene (6.4 mmol). The reaction was heated to 120 ^oC under N_2 for 2 hrs before quenching with 50 ml H_2O. The aqueous layer was extracted 3 times with 30 ml diethyl ether and the combined organic layer was washed with 50 ml brine and dried with $MgSO_4$. The crude product was concentrated *in vacuo* and was used for the next step without purification.

2-(4-Hexyl-2-methoxyphenoxy)benzenamine (**5**)[156]

Activated palladium on charcoal (200 mg) was added to a solution of compound **4** (2.0 g, 6.1 mmol) in 25 ml of MeOH. . The reaction mixture was stirred under hydrogen overnight and then filtered through celite. The crude product **3** in the filtrate was concentrated *in vacuo* and purified by automated column chromatography with silica gel using 5% ethyl acetate/petroleum ether as the mobile phase. The product was colorless liquid and the yield was 89%. ESI-MS calculated for $[M+H]^+$ m/z = 300, found 300.

1-(4-Hexyl-2-methoxyphenoxy)-2-iodobenzene (**6**)[157]

HCl (6M. 6.0 ml) and $NaNO_2$ (1.5 g) were added to a solution of compound **5** (2g, 6.7 mmol) in 50ml of 50% AcOH/50% H_2O at 0°C, and the mixture was stirred for 40 min prior to the addition of 4.8 g of KI (28 mmol). After 24 hrs, the reaction quenched with 200 ml solution of 50% DCM/50% H_2O. The organic layer was obtained and the aqueous later was extracted 2 times with DCM. The combined organic layer was dried with $MgSO_4$ and concentrated *in vacuo*. 1.74 g of crude product was collected and used for next step without purification.

2-(2-Iodophenoxy)-5-hexylphenol (**7**)[157]

6.3 ml BBr_3 solution (1M, 6.3 ml) was added dropwise to a solution of compound **6** (1.74g, 4.2 mmol) in 10 ml DCM at -78°C, and the mixture was warmed to room temperature slowly. Before quenching the reaction with 10 ml MeOH, the reaction was cooled to -78 °C. The reaction was dried *in vacuo* and redissolved with 30 ml DCM. Organic layer was washed with $NaHCO_3$, water and brine sequentially prior to dry with $MgSO_4$. The crude product was concentrated in vacuo and purified by automated column chromatography with silica gel using 4% ethyl acetate/petroleum ether as the mobile phase. The product was yellow liquid and the yield was 81%. ^1H NMR (300MHZ,

$CDCl_3$) δ 7.85 (dd, *J* = 8.4, 1.5 Hz, 1H), 7.24-7.30 (m, 1H), 6.72-6.90 (m, 3H), 6.74 (d, *J* = 8.1 Hz, 1H), 6.65 (dd, *J* = 8.1, 2.1 Hz, 1H), 5.51 (s, 1H), 2.56 (t, *J* = 7.8 Hz, 2H), 1.50-1.62 (br, 2H), 1.21-1.40 (br, 6H), 0.89 (t, *J* = 6.6 Hz, 3H); ESI-MS for $[M+H]^-$ m/z = 395, found 395

2-(2-(Tributylstannyl)phenoxy)-5-hexylphenol (**8**)[157]

t-BuLi (2M solution in cyclohexane, 1.14 ml, 2.28 mmol) was added dropwise to a solution of **7** (300mg, 0.76 mmol) in 10 ml dry diethyl ether at -78°C. The mixture was stirred for 30 min prior to the dropwise addition of tributylchlorostannane (0.818 ml, 3.04 mmol). The reaction was stirred at -78°C and allowed to warm to room temperature overnight. The reaction was then quenched with 0.1 M phosphate buffer (pH 7) at -78°C, and 100 ml 50% diethyl ether/50% H_2O was added. The organic layer was collected and the aqueous layer was extracted with additional diethyl ether.. The combined organic layers were dried over $MgSO_4$, and the solvent was removed *in vacuo*. The crude product was purified by automated column chromatography with silica gel using 1% triethylamine/4% ethyl acetate/95% petroleum ether as the mobile phase. The product was a yellow oil and the recovered yield was 25%. ^1H NMR (300MHZ, $CDCl_3$) δ 7.48 (dd, *J* = 7.2, 1.8 Hz, 1H), 7.22-7.28 (m, 1H), 7.08-7.12 (m, 1H), 6.88 (d, *J* = 2.1 Hz, 1H), 6.74 (dd, *J* = 7.5, 2.4 Hz, 2H), 6.64 (dd, *J* = 8.4, *J* = 2.1, 1H), 5.35 (s, 1H), 2.56 (t, *J* = 7.5 Hz, 2H), 1.47-1.63 (br, 8H), 1.24-1.36 (br, 12H), 1.04-1.10 (br, 6H), 0.84-0.92 (br, 12H); ESI-MS for $[M+H]^-$ m/z = 599, found 599.

Synthesis of [^{11}C]PT-70

The synthesis of [^{11}C]PT-70 was performed using organotin or stannanes **6** as the precursor[67]. The precursor (1.0 mg) was dissolved in 0.3 ml THF with 2 mg tetrakis(triphenylphosphine)palladium(0). After [^{11}C]CH_3I was purged into the solution and trapped at 0°C, the reaction vessel was sealed and heated at 100°C for 5 min in an oil bath. The reaction mixture was diluted with 1 ml of aqueous ammonium formate (0.1M) prior to loading onto a semi-preparative HPLC column. HPLC purification was performed using a reverse phase PFP column (Phenomenex, Luna PFP 250×10, 5 μm), at a 5 ml/min flow rate with a mobile phase consisting of 68% MeCN/32% aqueous ammonium formate (0.1 M). The product was collected at the expected retention time (17 min) and the solvent was removed by rotary evaporation. After dilution with 4 ml saline with 1 ml sterile alcohol, the solution was filtered through an Acrodisc 13-mm Syringe Filter with 0.2 μm Supor membrane (Pall Corporation, Ann Arbor, MI) into a sterile vial for delivery. Radiochemical purity was determined by reverse-phase analytical HPLC using a Phenomenex, Luna PFP, 250×4.6, 5 μm column operated at 1.0 ml/min flow rate using a mobile phase of 70% MeCN/30% water, with 10 min retention time. Subsequently, purity was verified using TLC (5% EA/95% HE, Rf = 0.45) by co-spotting the labeled product with a standard.

Synthesis of [^{11}C]PT-119

The synthesis of [^{11}C]PT-119 was performed using iodo-precursor **5**[80]. The precursor **5** (1.0 mg), K_{222}(0.2 mg) and tetrakis(triphenylphosphine)palladium(0) (2.0 mg) was placed in a vial with 0.2 ml DMSO and heated until all the solid dissolved. This solution was then added to [^{11}C]HCN that had been purged and trapped in 0.15 ml DMSO, and the reaction mixture was sealed in a reaction vial and heated at 135°C for 5 min in an oil bath. The reaction was quenched by the addition of 1 ml water and the mixture was filtered through celite prior to injection onto the semi-preparative HPLC column. HPLC purification was performed using a reverse phase PFP column (Phenomenex, Luna PFP 250×10, 5 μm), at a 5 ml/min flow rate with a mobile phase consisting of 70% MeCN/30% aqueous ammonium formate (0.1 M). The product was collected at the expected retention time (10 min) and the solvent was removed by rotary evaporation. After dilution with 4 ml saline with 1 ml sterile alcohol, the solution was filtered through an Acrodisc 13-mm Syringe Filter with 0.2 μm Supor membrane into a sterile vial for delivery. Radiochemical purity was determined by reverse-phase analytical HPLC using a Phenomenex, Luna PFP, 250×4.6, 5 μm column operated at 1.0 ml/min flow rate using a mobile phase of 70% MeCN/30% H_2O, with 10 min retention time. Subsequently, purity was verified using TLC (5% EA/95% HE, Rf = 0.4) by co-spotting the labeled product with a standard.

PET Imaging and Data Processing

All animal experiments performed in this study were approved by the Brookhaven Institutional Animal Care and Use Committee. Two baboons were included in this study. Ketamine hydrochloride (10mg/kg) was administered intramuscularly as an anesthetic agent and anesthesia was further maintained with oxygen (800 ml/min), nitrous oxide

(1500 ml/min) and isoflurane (Forane, 1-4%) during scanning. Two catheters were placed in a radial arm vein and the popliteal artery for [^{11}C]-labeled drug injection and arterial sampling, respectively. [^{11}C]-labeled drug was injected through the prior catheter and arterial blood was collected through the latter one as following time intervals: every 5 s for 2 min, then 2, 5, 10, 20, 30, 45, 60 and 90 min. During the PET scanning, heart rate, respiration rate, body temperature and pO_2 were monitored. Siemens HR+ (Siemens high-resolution, whole-body PET scanner with 4.5×4.5×4.8 mm resolution at the center of field of view) was used to perform dynamic PET scans for a total of 90 min with the following time frames in 3D mode: 1×10, 12×5, 1×20, 1×30, 8×60, 4×300, 8×450 s. Correction of attenuation was obtained by a transmission scan of a ^{68}Ge rod source prior to each PET scan. Six baboon studies were conducted with average injected doses for RIF, INH and PZA of 1.54 mCi, 4.38 mCi and 5.17 mCi respectively. Images were reconstructed by filtered back projection (FBP) and analyzed using AMIDE® software.[125]

LogD and PPB Determination

LogD determination: A test tube containing 2.5 ml of octanol and 2.5 ml of phosphate buffer solution (pH 7.4) was mixed with ~50 μl aliquot of formulated [^{11}C]-labeled drug by vortex for 2 min followed with centrifugation for 2 min to ensure full separation of the aqueous and organic phases. An aliquot from the octanol layer (0.1 ml) and aqueous layer (1 ml) were collected for radioactivity measurement. An additional 2.0 ml aliquot of the octanol layer was carefully transferred to a new test tube containing 0.5 ml octanol and 2.5 ml phosphate buffer (pH 7.4) and the previous procedure (vortex mixing, centrifugation, sampling, and transfer) was repeated for an additional five times to obtain six sets of samples. A well counter (Picker, Cleveland, OH) was used to measure radioactivity in each set of samples and the logD value of each sample was calculated by the following equation:

logD = log (decay-corrected radioactivity in octanol layer × 10/decay-corrected radioactivity in phosphate buffer layer).

PPB determination: A 10 μl aliquot of the formulated [^{11}C]-labeled drug was mixed with a sample of baboon plasma (0.8 ml, collected from at least 4 different baboons and pooled) by gently inverting several times. The mixture was incubated for 10 min at room temperature and then a 20 μl aliquot was taken to determine the total radioactivity in the plasma sample (A_T; $A_T = A_{bound} + A_{unbound}$). An additional 0.2 ml aliquot of plasma was placed in the upper level of a centrifree® tube (Amicon, Inc., Beverly, MA) and then the tube was centrifuged for 10 min. After discarding the upper part of the Centrifree tube, a 20 μl aliquot from the bottom part of the tube was taken to determine the amount of radioactivity that passed through the membrane ($A_{unbound}$). PPB was calculated by the following equation:

$$\% \text{ unbound} = A_{unbound} \times 100/A_T$$

Metabolite analysis

Several aliquots (~0.2 ml each) of baboon plasma sample were collected at various time points during the PET study. Each sample was counted and added to a solution of unlabeled standard (20 μl of a 1 mg/ml solution) in MeCN (0.3 ml). The resulting solution was vortexed and centrifuged and the supernatant was collected. After mixing with 0.3 ml water, the supernatant was analyzed by HPLC using the following condition: Waters μbondapak C-18 3.9×300 mm column with eluents 65% MeCN/35% 0.1 M aqueous ammonium formate at 1.0 ml/min using UV (254 nm) and radio-detection. The percent of unmetabolized radiotracer was determined as the ratio between the fraction of radioactivity coeluting with the unlabeled standard and the total radioactivity from the HPLC column.

Chapter 4

Evaluation of Carbon-11 Radiolabeled FabI inhibitors for Detection of *Staphylococcus aureus* in A Mouse Model of Infection

Infected animal experiments were conducted at BNL with Yang Lu and Hui Wang

Introduction

It has been estimated that 20% of the human population is a long-term carrier of *S. aureus*[129]. The incidence of infection has increased every year, and hospitalization involving *S. aureus* has almost doubled from 1999 to 2005[130]. The emergence of antibiotic-resistant strains, such as methicillin-resistant *S. aureus* (MRSA) and vancomycin-resistant *S. aureus* (VRSA), raises challenges for chemotherapy and increases mortality[127,130]. Although staph infections generally occur on the skin, *S. aureus* are able to disseminate via the blood stream or through surgical processes into other organs[131-133]. In particular, *S. aureus* can also invade the heart and cause endocarditis, which results in 25-47% mortality[134,135,158]. Typical diagnostic procedures for staph infection involve appearance upon examination and biological analysis of blood samples or nasal secretions. Recent technological advances in RT-PCR have enabled reliable and rapid procedures to be created for the identification and characterization of clinical isolates of *S. aureus*. However, challenges have remained for the clinical diagnosis of *S. aureus* endocarditis as it still primarily relies on unspecific signs such as heart murmur, fever and the presence of bacteria in the blood[158]. Given the high mortality rate that results from staph infection, there is a pressing need to develop improved diagnostic methods for this disease to guide the treatment.

Non-invasive imaging is emerging as a powerful tool to study *S. aureus* and complement current diagnostic methods. Optical imaging, which utilizes bioluminescent bacteria or synthetic fluorescent probes, has demonstrated notable successes in localizing and quantifying *S. aureus* in rodent[159-162]. However, pathogenic bacteria do not carry either luciferase enzymes or fluorescent proteins in their native state. In addition, optical imaging is only feasible for imaging bacteria at a depth of a few cm[162]. Several MRI studies of *S. aureus* have been reported, but the accumulation of contrast agents was nonspecific and attributed to inflammation[163,164]. Recently, imaging of *S. aureus* using PET and SPECT with radiolabeled antibodies, antibiotics, peptides and proteins has been reported[42,158,165-168]. Although antibodies and peptides can specifically bind to molecular targets, their relatively large size limits tissue diffusion and peptides are also vulnerable to decomposition by proteases[162]. A few antibiotics are tagged with radiolabel and evaluated in living animals. Traditional methods for labeling antibiotics typically employ a radiolabel that is attached through a linker or involves fluorine-exchange to generate low specific activity fluorine-18 analogues of drugs such as fluoroquinolone antibiotics[39,42]. Both methods however suffer from disadvantages: attachment of a linker may alter the biological activity of the antibiotics, while the latter results in very low specific activity radiotracer.

Here we report PET imaging studies of two saFabI inhibitors, PT-119 and PT-70 in *S. aureus* infected mice (**Scheme 4.1**). Those two inhibitors were developed in-house by Dr. Tonge's group, and radiolabeled with carbon-11 as described in Chapter 3. Both compounds demonstrate tight binding towards saFabI, and antibacterial activities of 0.5 μg/ml and 4 μg/ml MIC towards *S. aureus* for PT-119 and PT-70, respectively (**Table 3.1 Chapter 3**). In addition, PT-119 has a unique long residence time (99 min, **Table 3.1, chapter 3**), which is expected to increase the signal-to-noise ratio as the unbound radiotracer will be washed away[169]. While PT-70 is not a long residence time inhibitor of saFabI, it is a tight binding inhibitor and thus could serve as a control for PT-119.

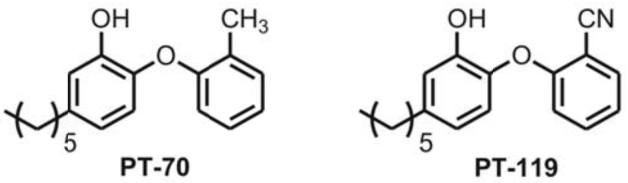

Scheme 4.1 Structures of PT-70 and PT-119

So far, we are still in the stage of animal model development with limited preliminary results. We started with the thigh infection model, which has been used significantly by different investigators before with different probes. [^{11}C]PT-119 and [^{11}C]PT-70 were not able to show significant accumulation in the infected thigh versus uninfected thigh. [^{18}F]FDG was then utilized to validate the model, but we failed to observe accumulation of [^{18}F]FDG as well. Given that [^{18}F]FDG was unable to image *S. aureus* in our thigh infection model, we turned to the systemic infection model where we observed significant accumulation ($P < 0.05$) of [^{18}F]FDG in infected kidney and spleen in comparison with corresponding organs in uninfected animals, which are consistent with the location of staph infection according to CFU counts. Additional experiments are planned to evaluate the performance of [^{11}C]PT-119 and [^{11}C]PT-70 in the systemic infection model.

Result and Discussion

In vitro assay for the uptake of radiolabeled compounds by *S. aureus*

In **Figure 4.1**, we depict the *in vitro* uptake of various radiolabeled compounds by *S. aureus* in 2 hrs. [^{18}F]FDG clearly demonstrates time-dependent uptake and increases almost linearly from 10 min to 2 hr, while [^{11}C]PT-119 was incorporated by the bacteria quickly and decreased from 20 min to 2 hr. In addition, bacteria accumulated ~3% of incubated [^{18}F]FDG in 20 min, which is 10 times lower than the uptake of [^{11}C]PT-119 (~45% of incubated dose). The significant difference suggests that [^{11}C]PT-119 is potentially a better probe than [^{18}F]FDG for *in vivo* imaging of *S. aureus*, although membrane association might contribute a certain amount of uptake. In addition, the specific activity of [^{11}C]PT-119 was probably 100-1000 times higher than [^{18}F]FDG as the latter was diluted with glucose, which may also contribute to the 10 times difference in uptake as well as the rate of uptake. The [^{18}F]FDG uptake we measured was 2 times higher than the value reported by Welling[35], which could due to slightly higher (25%) amount of bacteria in our system and differences in the bacterial strain.

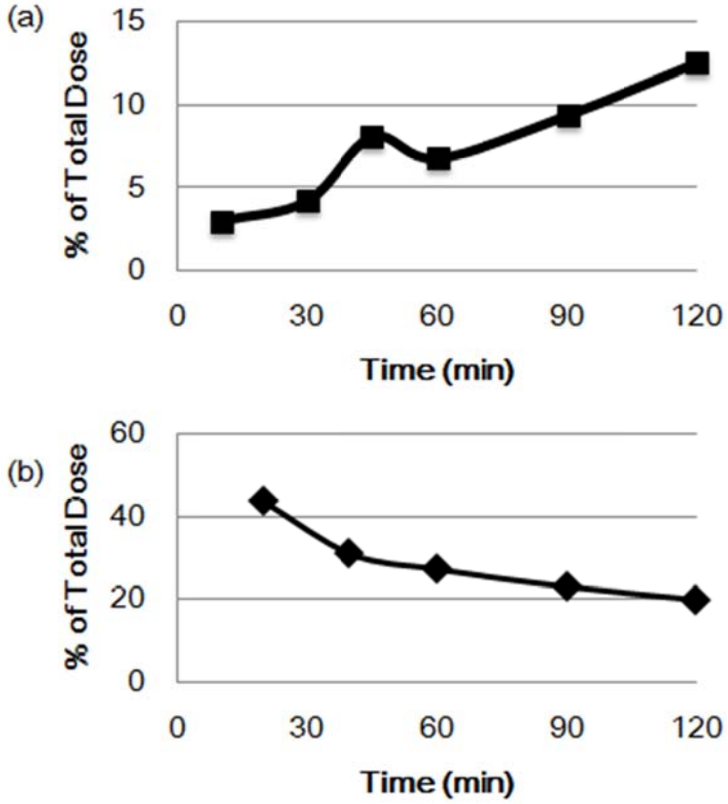

Figure 4.1 Uptake of (a) [^{18}F]FDG and (b) [^{11}C]PT-119 to viable *S. aureus in vitro*. 3 samples were taken for each time point.

The results of competition studies with corresponding “cold” compounds, [^{12}C]PT-119 and glucose, are presented in **Figure 4.2**. The addition of 10 mg/ml glucose resulted in a significant ($P < 0.005$) decrease in the uptake of [^{18}F]FDG when measured 20 min after incubation (**Figure 4.2 b**), and the ratio remained up to 2 hrs. Interestingly, the uptake of [^{11}C]PT-119 increased significantly ($P < 0.005$) with addition of 25 µg/ml PT-119. In addition, the competition group maintained at the uptake level over 2 hrs, while the group without addition of PT-119 decreased by 50% over the same time period. This unexpected result could be attributed to the high concentration (25 µg/ml) of PT-119, which is high enough to kill the bacteria giving the MIC value for PT-119 is 0.5 μg/ml. Thus the ideal candidate to compete with PT-119 would be a structurally similar compound, but with much lower antibacterial activity against *S. aureus*.

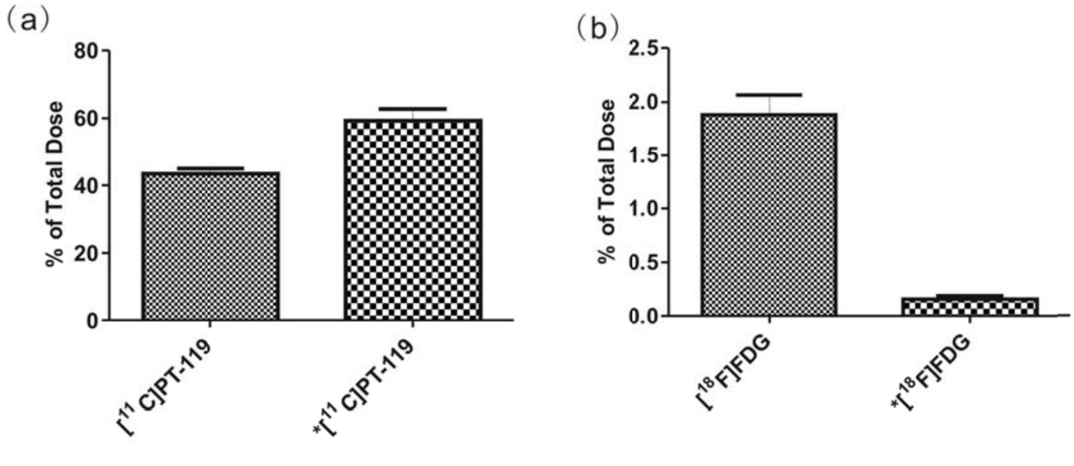

Figure 4.2 Uptake of (a) [^{11}C]PT-119 and (b) [^{18}F]FDG at 20 min. Group marked with * has either (a) cold PT-119 or (b) glucose added.

Biodistribution of radiolabeled [^{11}C]PT-70 in healthy mice

[^{11}C]PT-70 was injected iv into mice with (Study 1) or without (study 2) a predose of 200 mg/kg “cold” PT-70. The mice were euthanized one hr after injection [^{11}C]PT-70, and the biodistribution was determined by dissecting animals and counting radioactivity *ex vivo* (**Figure 4.3**). The accumulation of radioactivity was similar in major organs, although stomach and spleen demonstrated 4 and 2 fold difference respectively ($P < 0.05$). In addition, the ability of the compound to penetrate the blood brain barrier (BBB) provided further information to support the claim in **Chapter 3** that PT-70 may be of value for treating CNS TB and *S. aureus* meningitis.

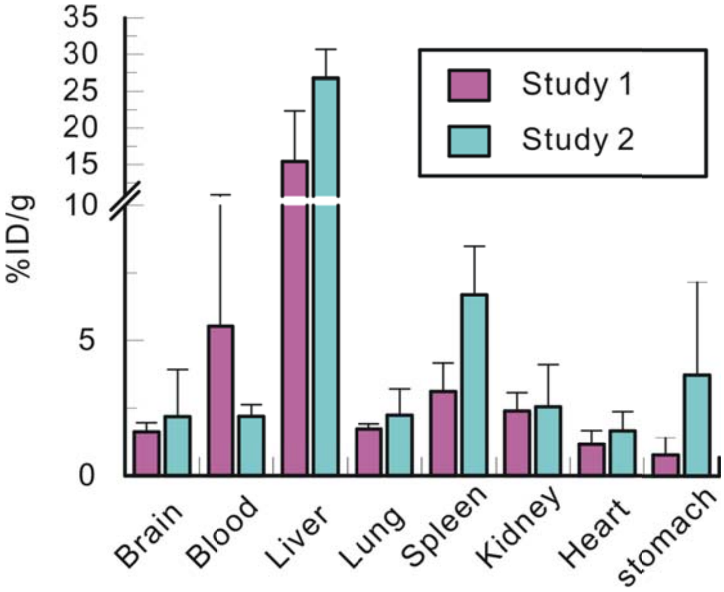

Figure 4.3 [^{11}C]PT-70 biodistribution in organs following dissection without (study 1) or with (study 2) predose of 200 mg/kg PT-70.

Imaging thigh infection model in immunocompetent mice

[^{18}F]FDG

Separate cohorts of ICR mice were inoculated with different amount of *S. aureus* RN4220 (~10^8 CFU or ~10^7 CFU) into the left thigh (T), and equal volumes of sterile growth media were injected into the right thigh (NT) as a control. [^{18}F]FDG (100~200 μCi) was injected iv 24 hrs post- infection. In **Figure 4.4 a** are shown T/NT ratios at 1 hr and 2hrs respectively after the administration of [^{18}F]FDG. Whole animal images at 7.5 min, 1h and 2h after the injection are shown in **Figure 4.4 b**. The T/NT ratio with

[^{18}F]FDG was measured by euthanizing the animals, counting the radioactivity and weighting the thighs. The ratios were significantly below one ($P < 0.05$) for all the study groups (**Figure 4.4 a**), while the value reported by Welling for the same study was 2.3-2.6[35]. The difference in strain alone, ATCC 25923 versus RN4220 in current report, is not likely enough to explain such a huge difference, given the uptake experiment *in vitro* demonstrated similar results. As shown in the images (**Figure 4.4 b)**, it seems that radioactivity has not penetrated into the thigh area. Thus we hypothesize that severe inflammation, observed from visual inspection of dissected thigh, has blocked the blood flow into area, and thus that [^{18}F]FDG was not exposed to the bacteria.

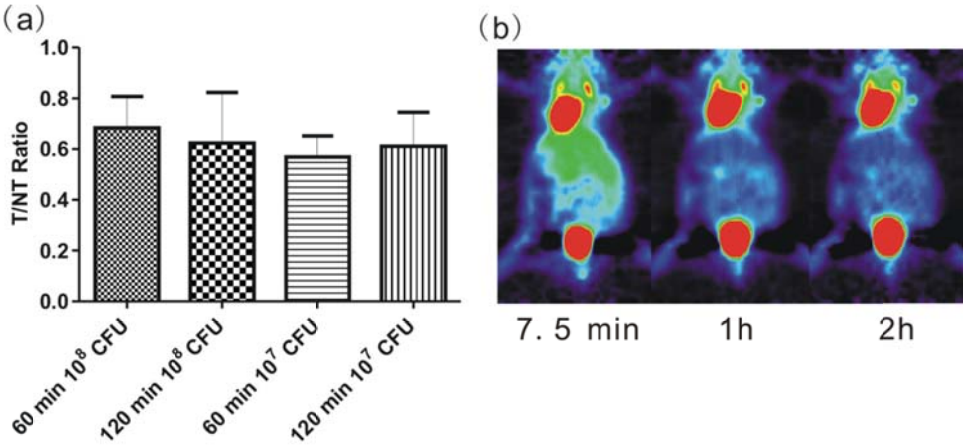

Figure 4.4 Detection of *S. aureus* in infected animal with [^{18}F]FDG. (a) N/NT ratio. (b) Averaged image at 7.5 min, 1h and 2h.

In order to limit the inflammation, additional experiments were conducted with immunocompromised mice. However, similar results were observed for immunocompromised mice (N/NT ratio were not significantly greater than one).

$[^{11}C]$PT-119 and $[^{11}C]$PT-70

Separate experiments were conducted with similar amounts of bacteria (~10^8 CFU) to inoculate the left thigh (T) while vehicle was injected into the right thigh (NT). $[^{11}C]$PT-119 or $[^{11}C]$PT-70 were then injected iv 24 hrs after infection. In **Figure 4.5 a** are shown the T/NT ratio at 20 min, 40 min and 60 min after the administration of $[^{11}C]$PT-119 while the corresponding images for $[^{11}C]$PT-70 are shown in **Figure 4.5 b**. The T/NT ratio was measured by euthanizing animals, counting the radioactivity and weighting the thighs.

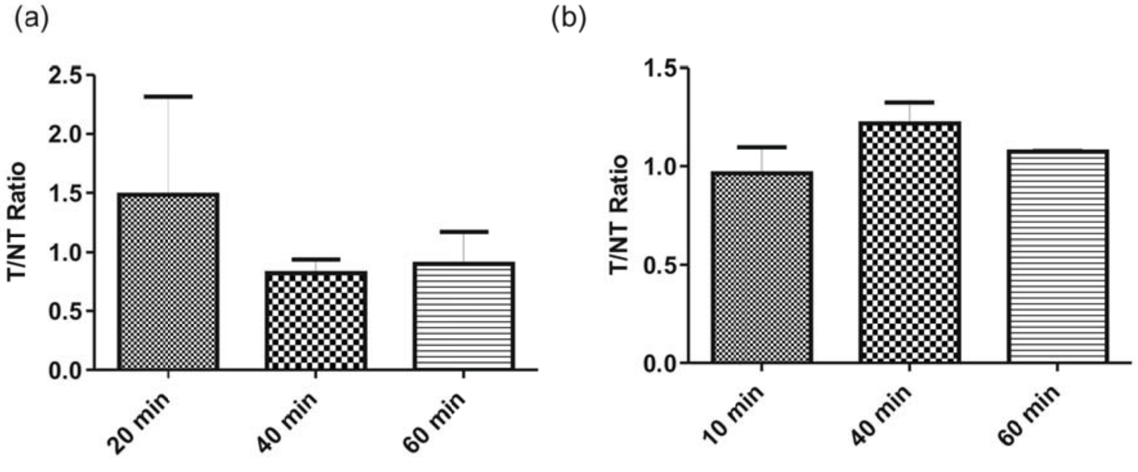

Figure 4.5 Detection of *S. aureus* in infected animal with (a) $[^{11}C]$PT-119 and (b) $[^{11}C]$PT-70

As shown in Figure **4.5 a**, the T/NT radio is about 1.5 20 min after injection and it decreased sharply to 0.8 at 40 min. At 60 min, it increased slightly to 0.9. Although 20 min ratio looks promising, it is not significantly higher than one ($P > 0.05$). In addition, there is no clear trend over the 1 hr study time frame, which made the design of additional experiments more difficult. Instead of focusing on [^{11}C]PT-119 alone, we moved toward another diaryl ether [^{11}C]PT-70 and performed similar experiment. As shown in **Figure 4.5 b**, the T/NT ratio are less variable than that with [^{11}C]PT-119. The N/NT ratio moved from 0.97 at 10 min to 1.22 at 40 min. At 60 min, the ratio decreased to 1.1. Again, the trend is not clear whether the ratio would increase or decrease over time, which made it hard to decide whether we should pursue probes with radiolabels that have longer half-lives.

These results, especially the control from [^{18}F]FDG, tend to suggest that our animal model may not be the best for our purpose, although it has been utilized by other researchers intensively for nuclear imaging and optical imaging and they demonstrated that the T/NT ratios are between 2 to 6[35,160,165,170]. An alternative explanation is that our thigh infection model differs fundamentally from that used in other studies. However, the consistent bacterial growth measured by CFU, together with reliable efficacy studies using the same model, suggests that the model is performing as expected. Since we have so far been unable to explain the apparent discrepancy between our results and those reported in the literature, we decided to pursue the systemic infection model for comparative purposes.

Imaging systemic infection model in immunocompetent mice

[^{18}F]FDG

Systemic infection was induced by ip injection of *S. aureus* with an infection dose of 5 × 10^6 CFU/mouse (low dose) or 5 × 10^8 CFU/mouse (high dose). [^{18}F]FDG (100~200 μCi) was injected iv 24 hrs post-infection. In **Figure 4.6** are shown the radioactive counts detected in major organs from the control group, low dose infection group and high dose infection group 2 hrs after [^{18}F]FDG administration. Radioactivity in the spleen and liver from the high dose infection are significantly higher than the control group ($P < 0.05$). It is well known that ip inoculation leads to significant levels of bacterial infection in the spleens of infected animals. In out experiments the highest levels of infection were observed in the spleen, which is consistent with the observation that accumulation of [^{18}F]FDG was highest in this organ (~2.5 fold above background). The results presented as a control experiment to validate the animal model, and suggest that the systemic model might be suitable for imaging *S. aureus in vivo* with other probes, such as [^{11}C]PT-119 and [^{11}C]PT-70. The next steps of this project will utilize systemic model to evaluate the [^{11}C]PT-119 and [^{11}C]PT-70 distribution.

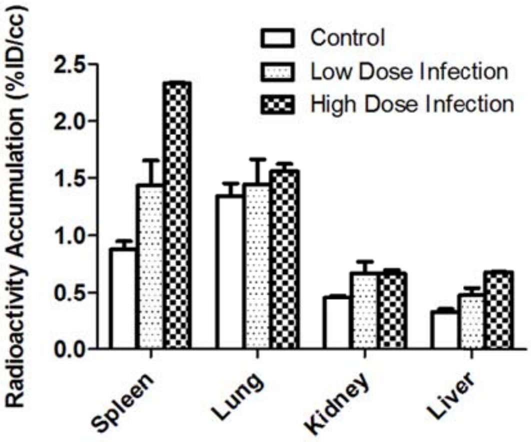

Figure 4.6 Detection of *S. aureus* in systemic infected animal 2 hr after [^{18}F]FDG administration

Experimental Section

Chemicals

[^{18}F]FDG (5-10 mCi) was purchased from Cardinal Health (Plainview, NY) on each day of experiment. [^{11}C]PT-70 and [^{11}C]PT-119 were made in-house according to the method described in **Chapter 3**.

***In vitro* assay for the uptake of radiolabeled compounds by bacteria**

S. aureus RN4220 strain was grown to mid-log phase (OD = 0.8) in Muller-Hilton (MH) broth. 1 ml of culture was centrifuged at 10,00 rpm for 3 min and the cell pellet was resuspended in 1 ml of saline . Radiolabeled compound (~1mCi in 1-2 ml saline, specific activity = 50-200 mCi/μmol at the time of incubation) was subsequently added to the bacterial suspension (20 ml) while "cold" compound was added to the control group. The bacterial suspension was incubated at 37 °C and aliquots (1 ml) were removed at 5 min, 10 min, 20 min, 40 min, 1 hr, 2 hr, centrifuged and washed once with saline to reduce the background signal. An empty tube without bacteria was incorporated as a control for background correction. A well counter (Picker, Cleveland, OH) was used to measure radioactivity in each set of samples. The radioactive counts were decay corrected to the time of that the incubation was initiated.

Animal experiment

All of the animal experiments were approved by the Brookhaven Institutional Animal Care and Use Committee or Stony Brook University Institutional Animal Care and Use Committee. Animals were purchased from Taconic or Charles River.

Thigh infection model[35]

Female ICR mice (Charles River) weighting between 22-28 g (6-8 weeks) were used for experimental infection. The animals were housed in the animal facility for 1 week before the experimental day, and food and water were given *ad libitum*. *S. aureus* RN4220 was striped on Muller-Hilton agar sheep blood plate and incubated at 37 °C. A single colony was picked and cultured in 15 ml MH broth at 37°C to mid log phase (OD = 0.8). Cells were collected by centrifugation (10,000 rpm, 3 min) and washed with saline (1 ml). The cell pellet was resuspended in saline (1 ml) containing 1% BHI media and injected im into the left thigh at doses of 5×10^7 cells/thigh or 5×10^8 cells/thigh. At the same time the right thigh of each animal was injected im with empty vehicle as control.

Systemic infection model[171]

Male Swiss Webster mice (Taconic) weighting between 32-37 g (6-8 weeks) were used for experimental infection. The animals were housed in the animal facility for 1 week before the experimental day, and food and water were given *ad libitum. S. aureus* RN4220 was striped on Muller-Hilton agar sheep blood plates and incubated at 37°C. A single colony was picked and cultured in 15 ml of MH broth at 37°C to mid log phase

(OD = 0.8). Cells were collected by centrifugation (10,000 rpm 3 min) and washed with saline (1 ml). Cell pellets were resuspended in saline (1 ml) containing 1% BHI media and 500 µl was injected ip into mice at 5×10^6 cells/mouse or 5×10^8 cells/mouse.

Detection of *S. aureus* infections in mice

Anesthesia was initiated with 5% isoflurane and maintained with 1-4% isoflurane during the imaging process. Mice were placed on the mPET (MicroPET R4, Siemens) scanner prior to injection of radiolabeled compounds ([^{18}F]FDG, [^{11}C]PT-119, or [^{11}C]PT-70). Data acquisition was started simultaneously with the injection of radiolabeled compound. During the scan, the mice were immobilized with surgical tape and kept warm at 30°C during imaging using a heating lamp. Dynamic PET scans (60-120 min) were performed in 3D mode, and the raw data were reconstructed by 3D filtered-back projection (FBP). Results were analyzed using AMIDE software.

Bacterial CFU counting

Animals were euthanized at the end of experiment and target organs were collected and weighted separately. Each organ was homogenized in 1ml saline and a series of dilutions were performed. 50 µl of each dilution was spread on a Muller-Hilton agar sheep blood plate which was then incubated at 37°C for 24h. CFUs were counted and normalized to weight.

Biodistribution of radiolabeled compound in mice

Female ICR mice weighting between 22-25 g (4-6 weeks) were purchased from Charles River. The animals were housed in the animal facility for 1 week before the experimental day, and food and water were given *ad libitum.* [^{11}C]PT-70 (100-150 µCi, 200-500 µl, specific activity = 7-13 Ci/µmol at the end of bombardment (EOB)) was injected iv into study 1 group while PT-70 (200mg/kg) was administered ip into study 2 group prior to the infection of [^{11}C]PT-70. Mice were euthanized 60 min post administration, and target tissues were obtained by dissection and then weighed, and counted for radioactivity with a well counter (Picker, Cleveland, OH).

Statistical analysis

Statistical comparison between groups was performed using one tail distribution, two sample, unequal variance student t-test in Excel 2010 (Microsoft) and expressed as the Pearson's correlation coefficient.

Chapter 5

Non-invasive PET Imaging of 2-[^{18}F]-Fluoroisonicotinic acid hydrazide in *Mycobacterium tuberculosis* Infected Mice

This chapter is based on the following manuscript:

Weinstein, E.A.* **Liu, L.,*** Wang, H., Ordonez, A.A., Tonge, P.J., & Jain, S.K., Noninvasive Determination of 2-[^{18}F]-Fluoroisonicotinicacid hydrazide Pharmacokinetics by Imaging *Mycobacterium tuberculosis* Infected Mice. *Antimicrob. Agents Chemother.* Manuscript in Preparation

Infected animal experiments were conducted at JHU with Dr. Weinstein in Dr. Jain's lab. Dr. Weinstein and Mr. Wang helped with the preparation of the manuscript.

Introduction

Tuberculosis (TB) is a global health threat, and the choice of treatment of this particular pathogen is driven by the relatively unsophisticated diagnostic methods. The basic methods for diagnosis of active Mtb infection have not changed for decades and generally rely on the availability of clinical samples that contain bacteria, either for acid fast staining and/or culturing, or, more recently, for nucleic acid amplification[172]. In addition, while one focus of development of diagnosis is for active TB, Mtb is primarily found in the body in a latent or non-replicating state. The detection of latent TB relies on the tuberculin skin test using PPD that requires a relatively intact immune system and is negative in approximately 20% of people with known TB[173]. The Quantiferon method which detects the production of interferon-gamma in response to mycobacterial antigens has approximately the same predictive value as the PPD skin test. Thus, in order to combat the spread of TB, an efficient, reliable and rapid method that can not only diagnose infection but that can also differentiate between different bacterial populations in humans is in urgent need.

PET is a well established technique for imaging human brain function and cancer status[20,25-27]. While PET has previously been used to image the distribution of [^{18}F]FDG in patients infected with TB, ^{18}FDG is a monitor of glucose uptake and so many tissues and cells, both normal and abnormal, will take up ^{18}FDG[174]. Although ^{18}FDG may be able to image TB bacteria, this radiotracer has limited diagnostic value since it cannot distinguish TB from other pathological, as well as benign, conditions[175]. [^{125}I]-FIAU has been developed for bacteria imaging, including TB, by targeting thymidine kinase (TK). However, it cannot differentiate bacteria from species and it also requires to externally engineering Mtb strain with chromosomally integrated bacterial TK[176]. Zhang and coworker reported the utility of bioluminescent Mtb reporter stains that enabled monitor bacteria population *in vivo*. Although this technique demonstrates to be valuable in treatment evaluation, its diagnostic value is minimal as patients will not carry this particular strain of TB bacilli[177]. A sensitive detection of nonrecombinant strains that cause TB has been developed by Cirillo and coworkers by utilizing reporter enzyme fluorescence (REF) method, which uses β-lactamase as the reporter enzyme and a specific probe for imaging. Although this method demonstrates potential in animal model, it would be difficult to apply to patient as the limitation of signal penetration of optical imaging[178,179]. Thus, there is a pressing need to develop novel target-specific PET probes that can be readily translated to patient.

Isoniazid (INH) was first recognized as an antitubercular drug back in 1952[180], and it has been the most widely used drug for the treatment of TB since then[121]. Our hypothesis is that the INH will accumulate in infected tissue, enabling bacterial populations to be non-invasively imaged using PET. The mode of action of INH was first reported by Cole and coworkers that INH is a prodrug activated by mycobacterial catalase-peroxidase enzyme KatG as its mutations are discovered in a major fraction of clinical isolated INH resistant strains[119,138,181]. In addition, Jacobs and coworkers identified InhA as the target of INH, which became the general consensus for the antitubercular mechanism of INH, although Barry and Blanchard have identified KasA and DHFR as targets for INH, respectively[182-185]. As there was considerable technical challenge to perform [^{11}C]INH imaging study in TB infected animals, we mitigated the challenge by imaging fluorine-18 labeled INH analog, 2-fluoro-isonicotinic acid hydrazide (2-F-INH).

The antitubercular activity of 2-F-INH, an analog of INH, was first reported by Cordes and coworkers in 1976[186]. Subsequently, Amartey incorporated fluorine-18 into 2-F-INH and reported its localization to the site of infection in *E. coli* infected mice with 3.0 ratio between infected and uninfected thighs[187,188]. However, the mechanism of similarity/difference between 2-F-INH is still poorly understood, and *E. coli* does not carry activation enzyme KatG or its analog.

Here we report a direct comparison of 2-F-INH and INH at the molecular level which suggests 2-F-INH will behave similar to INH for the *in vivo* imaging experiment as the accumulation of INH or 2-F-INH is driven by KatG activation[189]. We also developed a novel injection system to determine the host pharmacokinetic profile of 2-[^{18}F]F-INH and compare tracer accumulation in the lungs, brain, and liver of Mtb infected mice. The data indicates that 2-[^{18}F]F-INH accumulates specifically in the bacterial lesions. The C3HeB/FeJ mice demonstrate foci of signal intensity consistent with granuloma like lesions observed on CT. Although the 2-[^{18}F]F-INH signal is only slightly larger in Mtb infected mice than uninfected mice, the platform we developed here can be used for future development of diagnosis technology.

Results

Radiochemistry

The radiosynthesis of [^{11}C]INH has been published elsewhere[80]. The radiosynthesis of 2-F-INH (**3**) (**Scheme 5.1**) was adopted from the method reported by Dr. Amartey and coworkers[188].

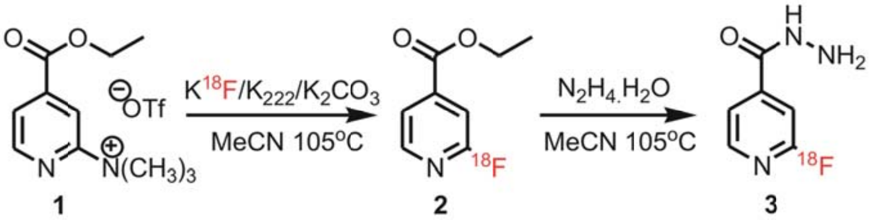

Scheme 5.1. Radiosynthesis of 2-[^{18}F]fluoro-isonicotinic acid hydrazide

The average radiochemical yield of the intermediate **2** was 65-75%, based on TLC, using 2 mg **1** and 2 min reaction time at 105 °C. In addition, the yield decreases with increasing reaction time, reaching below 25% over 5 min. This observation is in contrast to previous reports[181,188] which state that the yield remains the same between 2 and 10 min. The discrepancy could be attributed to the slightly higher reaction temperature compared to the one used previously[188]. The second step was initially carried out according to reported procedure[188]. However, the combination of 5 µl $N_2H_4.H_2O$ and 300 µl EtOH did not lead to a reasonable yield. Several combinations of $N_2H_4.H_2O$ and solvents were evaluated, and 50 µl $N_2H_4.H_2O$ with 300 µl MeCN was found give the highest yield with nearly 100% yield in “cold” reaction and 50%-60% yield in “hot’ reaction. The by-product of the second step is $[^{18}F]F^-$ ion, which is generated through the nucleophilic substitution with N_2H_4. Purging with N_2 gas before quenching removed excess N_2H_4, which otherwise will affect the product elution. Compound **3** was subsequently purified by HPLC using a semipreparative Phenomenex Luna PFP column (250 × 10, 5μm) and eluted around 10 min. In the optimized reaction scheme, the decay-corrected yield (DCY), calculated from eluted $[^{18}F]KF$, was 25-30% in a total synthesis time of 75 min. Analytical HPLC and TLC demonstrated that the radiolabeled product was over 98% radiochemically pure, with a specific activity of 200-300 mCi/μmol at the time of administration to the animal.

Activity of 2-F-INH against wild type $H_{37}R_v$ Mtb and isoniazid resistant mutants.

INH is typically activated by the catalase-peroxidase KatG[119], after which the compound forms a NAD adduct that inhibits the target protein InhA[119,183,190,191]. 2-F-INH has an MIC_{99} of 8 μg/ml against H37Rv, which is similar as first reported by Cordes and coworkers in 1976[90], as opposed to 0.025 μg/ml for INH. In addition, the MIC of 2-F-INH increased to 32 μg/ml with INH-resistant strains of $H_{37}R_v$ with mutations in the *katG* gene in the promoter[192] (M1A,INH MIC_{99} >2 μg/ml) and point mutation W149R (INH MIC_{99} >1 μg/ml). Likewise, a third INH resistant strain with a -8 T→A mutation in the promoter region of *inhA* (INH MIC_{99} 0.1 mg/ml) had an MIC_{99} of >32 μg/ml for F-INH. Thus the fact that MIC of 2-F-INH increases even more in INH resistant strains indicates that 2-F-INH is activated by the same mechanism as INH.

Analysis of 2-F-INH KatG mediated NAD adduct formation, InhA inactivation, and *in vitro* accumulation of 2-F-INH in *Mtb*.

Given a similar pattern of activity between 2-F-INH and INH against drug resistant Mtb. strains, we next determined whether 2-F-INH undergoes a similar pattern of adduct formation with NAD prior to inhibition of InhA. Recombinant, purified Mtb KatG was used to oxidize INH or 2-F-INH. Adduct formation monitored by HPLC demonstrated similar amounts of adduct formation for both INH and 2-F-INH based on UV absorption at 260 nm and 326 nm. Next, the time-dependent inactivation of InhA by INH and 2-F-INH was measured by monitoring the oxidation of NADH *in vitro*. The inactivation followed first order kinetics with a rate constant of 0.0299 and 0.0104 min^{-1} for INH and 2-F-INH, respectively (**Figure 5.1**). Complete inhibition of InhA was achieved within 90 min for INH, whereas 2-F-INH required over 120 min. In the control groups, the inhibition of InhA was negligible(< 10% loss) without addition of KatG or drug(not shown). This decreased InhA activity has been attributed to the slow degradation of InhA *in vitro* or autoxidation of drug[193]. This provided one explanation for the apparent reduced Mtb MIC_{99} of 2-F-INH as compared to INH.

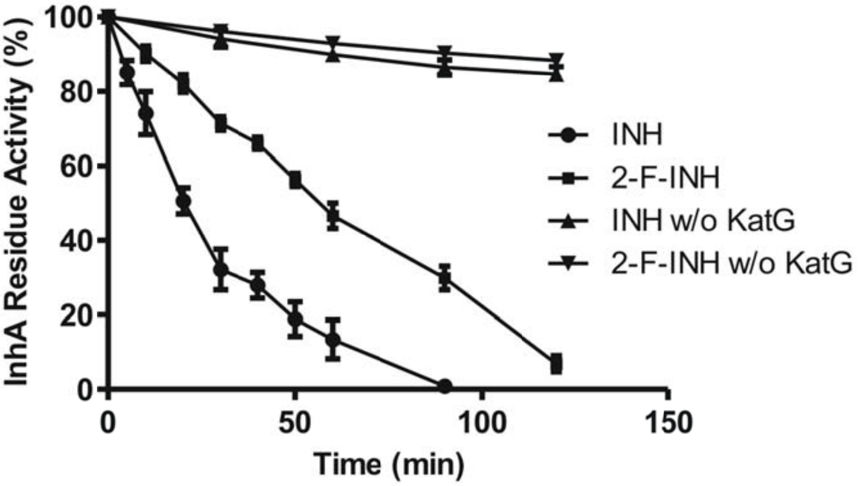

Figure 5.1 Inactivation of InhA with INH and 2-F-INH

The NAD adduct formation assay showed that 2-F-INH was readily oxidized by KatG, but could not determine whether 2-[^{18}F]-INH was appreciably trapped intracellularly. We therefore tested the intracellular accumulation of 2-[^{18}F]-INH in wild type Mtb and INH resistant mutants (**Figure 5.2**). Following an 8 hour incubation, 2-[^{18}F]-INH (198 cpm) readily accumulated within wild type Mtb. Only the most INH resistant strain, *KatG* M1A, demonstrated significantly reduced intracellular accumulation of 2-[^{18}F]-INH (23 cpm). Taken together, these data indicate that the addition of fluorine at the second position significantly decreases activity against InhA and Mtb growth, but the analog generally follows a similar pattern of metabolism, cellular uptake and attenuated activity against isoniazid resistant mutants.

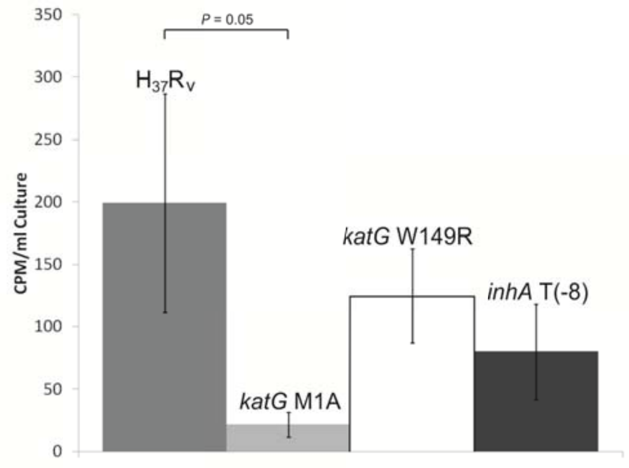

Figure 5.2 Cell associated radioactivity following 8 hour incubation with 2-^{18}F-INH in wild type $H_{37}R_v$ Mtb and isoniazid resistant strains.

PET Imaging of 2-[^{18}F]F-INH in H37Rv Mtb infected mice.

2-[^{18}F]-INH was synthesized and purified by a modified method of Amartey et al [188] with resultant specific activity of 200-300 mCi/µmol at the time of administration to the animal. We hypothesized that the metabolism of isoniazid by the Mtb KatG may result in selective intracellular trapping of the NAD adduct and therefore generate a TB-specific PET signal. C3HeB/FeJ mice were selected for their lack of expression of *Ipr1* within the super-susceptibility to TB 1 (*sst1*) locus, endowing the mice with an intrinsic ability to form granuloma like lesions with central casseous necrosis in response to infection with Mtb[194]. 5-6 week old female C3HeB/FeJ mice were infected with approximately 1 x 10^2 CFU Mtb (H37Rv) by aerosol infection, which at 17 weeks post infection resulted in 5 x 10^6 CFU in the lungs. Mice underwent standard tail vein injection of 200 µCi 2-[^{18}F]-INH in biosafety level 3 conditions with subsequent biocontainment for imaging. Mice were scanned in pairs with infected mice positioned next to uninfected controls in separate biocontainment tubes. Images (**Figure 5.3**) were acquired 60 minutes following injection. Discrete foci of PET activity were noted in the lung fields of infected mice, but not in uninfected animals. Background activity is noted as expected in the liver, kidneys and bladder. Nonspecific PET signal was also noted within the brain field, possibly due to slow washout across the blood brain barrier.

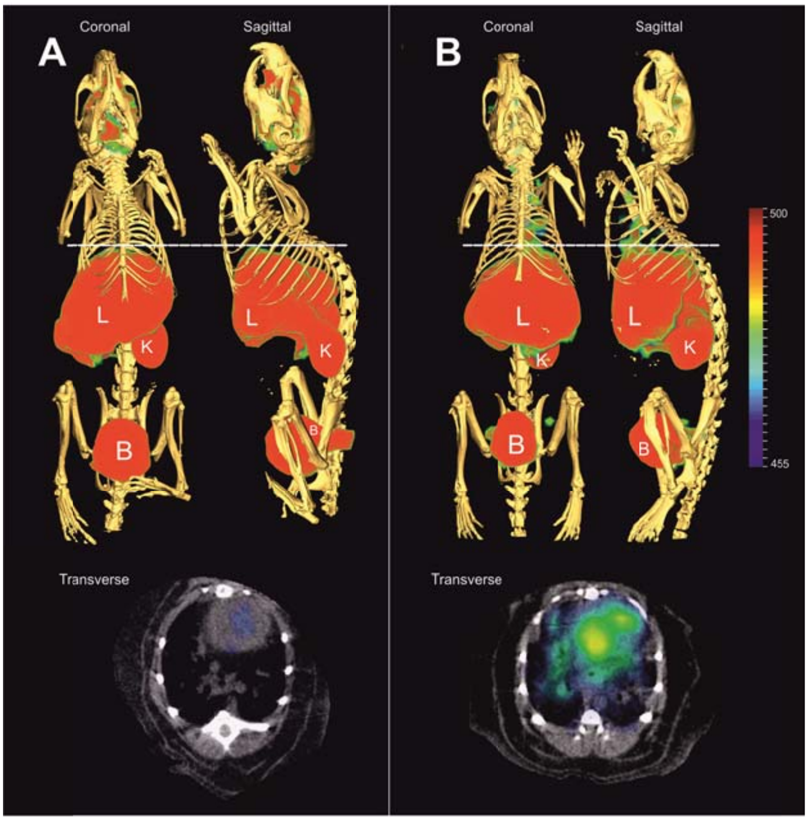

Figure 5.3 Combined PET/CT imaging of C3HeB/FeJ mice at 17 weeks infection with Mtb compared to uninfected control. A) Uninfected mouse imaged with 2-^{18}F-INH, B) Infected mouse imaged with 2-^{18}F-INH. C3HeB/FeJ infected with 10^2 CFU of *M. tuberculosis* by aerosol contained 5 x 10^6 CFU in the lungs at the time of imaging. Mice were injected with 200 µCi of 2-[^{18}F]-INH via the tail vein and imaged in pairs 120

minutes post-injection using the Mosaic HP (Philips) Small Animal PET imager followed by immediately by a CT scan. Whole animal sagittal and transverse sections are displayed as combined PET/CT images with heart (H), liver (L), kidneys (K), and bladder (B) marked

To confirm these results, a second BALB/C mouse model was selected which produces a diffuse, disseminated Mtb infection in response to a similar low dose aerosol infection. Mice were imaged 8 weeks post infection, at which point the initial 10^2 CFU bacterial implantation progressed to 2.7×10^6 CFU in the lungs. The BALB/C animals were younger, and therefore weighed less (20.2 g ± 1.2 g) compared to the C3HeB/FeJ mice (37.1 g ± 6.0 g). There was no significant difference in weight between infected and uninfected animals. Mice underwent standard [^{18}F]FDG PET imaging with anatomical CT co-registration (**Figure 5.4**, **panels A and B**) as previously described [194]. Diffuse FDG-PET activity was noted in the lung fields in infected animals, with minor activity in the abdomen. Typical background FDG uptake was noted in heart, brain, bladder and kidneys, as observed in the uninfected control. Next, imaging was performed with 2-[^{18}F]-INH. Uninfected mice (**Figure 5.4, panel C**) demonstrated background PET activity in the liver, kidneys and bladder. Infected animals (**Figure 5.4, panel D**) produced an additional PET signal in the lung fields and spleen, the expected sites of diffuse TB infection.

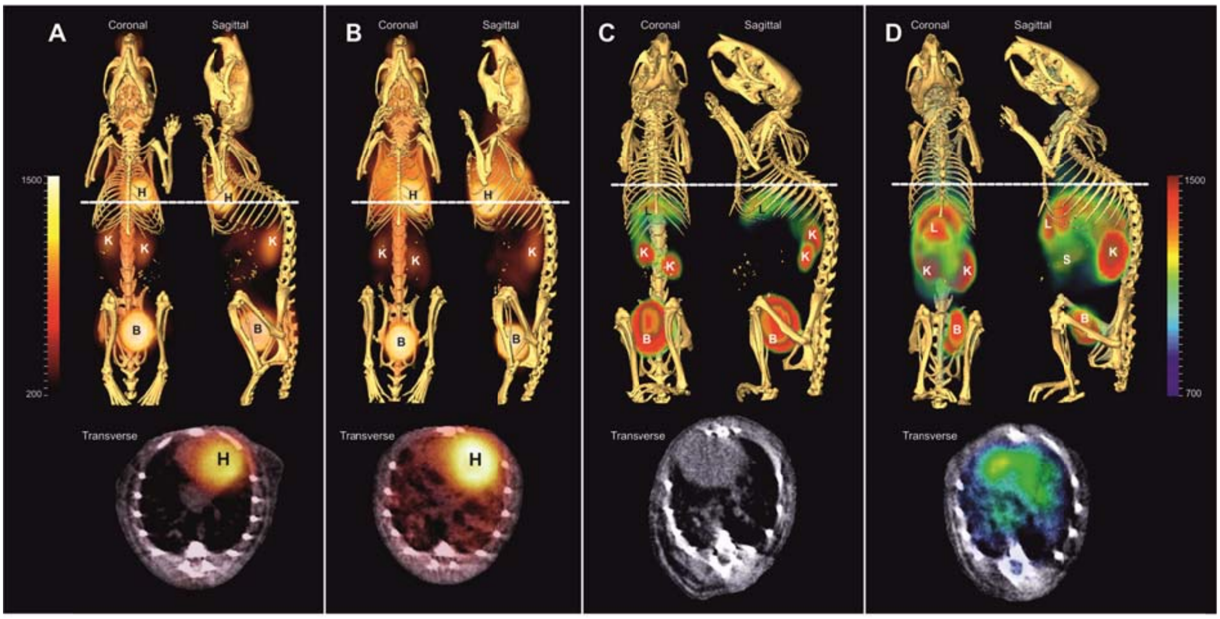

Figure 5.4 Combined PET/CT imaging of BALB/C mice at 8 weeks infection with Mtb compared to uninfected controls. A) Uninfected mouse imaged with ^{18}F-FDG, B) Infected mouse imaged with ^{18}F-FDG, C) Uninfected mouse imaged with 2-^{18}F-INH, D) Infected mouse imaged with 2-^{18}F-INH. BALB/C mice infected with 10^2 CFU of *M. tuberculosis* by aerosol contained 2.7×10^6 CFU in the lungs at the time of imaging. Mice were injected with 260 µCi of 2-[^{18}F]-INH via the tail vein catheter and imaged in pairs 40 minutes post-injection using the Mosaic HP (Philips) Small Animal PET imager followed by immediate CT scan. Whole animal sagittal and transverse sections are displayed as combined PET/CT images with heart (H), liver (L), kidneys (K), spleen (S) and bladder (B) marked

Organ compartment pharmacokinetics of 2-[^{18}F]-INH in Mtb infected and uninfected mice.

Given the qualitative differences in the 2-[^{18}F]-INH PET signal between Mtb infected and uninfected mice we wished to perform a quantitative analysis. To permit on table injection of tracer, we fashioned a tail vein microcatheter within the biosafety 3 biocontainment tube (**Figure 5.6**). Following simultaneous 2-[^{18}F]-INH injection into paired infected/uninfected BALB/C mice, we acquired PET data over time as a series of windows. Using the CT co-registration data, spherical regions of interest were drawn in the lung, brain, and liver fields. Each data point represents the mean intensity of 3 animals. Organ specific regions of interest were drawn spherically based upon CT imaging. For the lungs two regions of interest were drawn to encompass the left and right lung fields**.** There was significantly more 2-[^{18}F]-INH in the lung fields of infected mice versus uninfected controls from 40 minutes post injection to the end of the recording at 60 minutes (**Figure 5.5, panel A**). Presumed restriction of drug passage through the blood brain barrier produced a distinctly different PET activity profile, in which rapid uptake peaked 15 minutes post injection then slowly diffused away (**Figure 5.5, panel B**). While the signal was greater in infected mice, it was not statistically significant. As expected, the liver intensity was not significantly different between the infected and uninfected animals (**Figure 5.5, panel C**), but of overall higher magnitude as this is the site of isoniazid host metabolism.

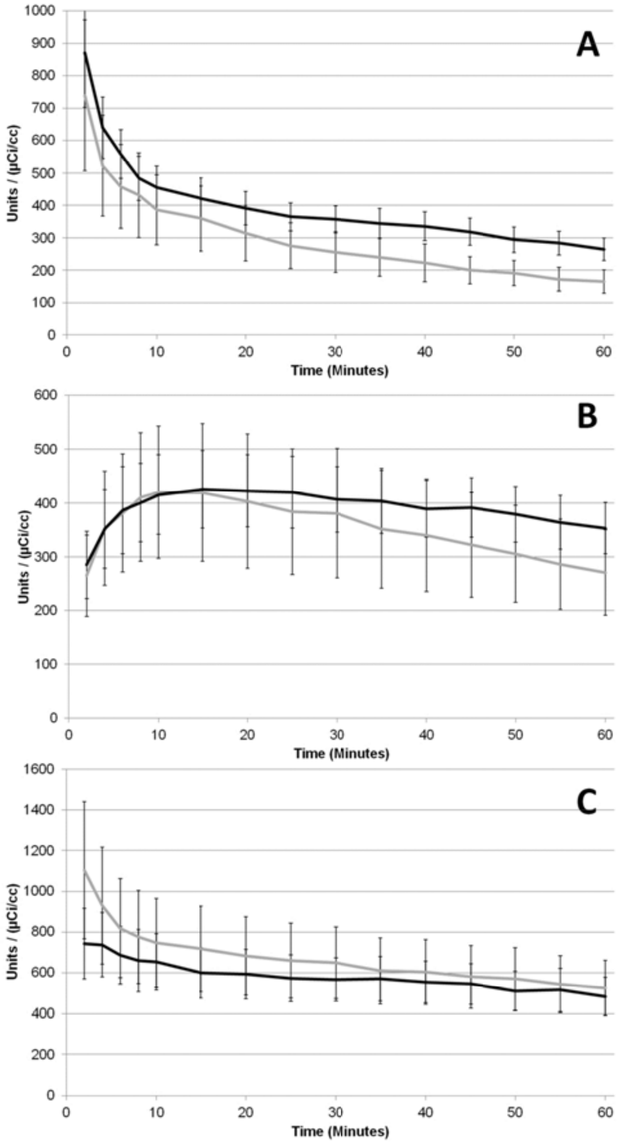

Figure 5.5 Quantitation of mean PET activity in A) Lung, B) Brain and C) Liver organ compartments. On table injection of 2-^{18}F-INH performed on BALB/C mice 8 weeks infected with Mtb (solid line) or uninfected controls (grey line). BALB/C mice were simultaneously scanned as infected / uninfected pairs following on table injection of 260 µCi of 2-[^{18}F]-INH by tail vein catheter. Dynamic windows were selected to acquire PET activity during 2 minute intervals for the first 10 minutes, followed by 5

minute intervals for a total of 60 minutes. Organ specific regions of interest were drawn spherically based upon CT imaging. For the lungs two regions of interest were drawn to encompass the left and right lung fields. Each data point represents the mean intensity of 3 animals with error bars indicating the standard error of the mean. *P* < 0.05 for the lung field signal intensity between infected and uninfected animals from 40 minutes to 60 minutes.

Figure 5.6 Design of PET scan with TB infected animals in BSL2 lab with BSL3 biocontainer

Discussion and Conclusion

Isoniazid has been the mainstay of TB treatment since its introduction in 1952[121,180]. Attempts have been made to synthesize active analogs, and the antitubercular activity of 2-F-INH (MIC = 40 μg/ml) was first reported by Cordes and coworkers in 1976[186]. Subsequently, Amartey incorporated fluorine-18 into 2-F-INH and reported its *in vitro* accumulation in *S. pneumoniae* and its *in vivo* localization to *E. coli* infected mouse thighs with infected/uninfected ratio of ~3.5[187,188]. As neither of these microbes contains the katG oxidase-peroxidase, the mechanism of accumulation was unclear, and perhaps involved a nonspecific oxidation event. While this is known to occur inorganically with MnII or MnIII[195], it remained imperative to establish the mechanistic similarity between 2-F-INH and INH for our studies. Here we report a direct comparison of 2-F-INH and INH with an *in vitro* KatG activation assay. We described a similar activation profile between 2-F-INH and INH, but INH demonstrated faster time-dependent inhibition of InhA. The general consensus for the antitubercular mechanism of INH is the inactivation of InhA, however it is important to note that Barry and Blanchard have identified KasA and DHFR as possible targets of INH[182-185]. Nevertheless, we suggest that the higher MIC_{99} of 2-F-INH is likely due to reduced inactivation of InhA rather than KatG discrimination.

We used the fluorine-18 analog of 2-F-INH to determine a pharmacokinetic profile of drug distribution in infected and uninfected murine models of TB. To our knowledge, this is the first example of on table radiotracer injection for imaging of biosafety level 3 organisms in a biosafety level 2 environment. The simple use of a tail vein catheter can be readily used by others to overcome this technical problem.

The data suggest that 2-[^{18}F]F-INH demonstrates lesion specific PET activity. The C3HeB/FeJ mice demonstrated punctuate foci of signal intensity consistent with granuloma like lesions observed on CT. Our previous work has established that these lesions both contain bacilli and are [^{18}F]FDG avid[194]. We note that the distribution between the 2-[^{18}F]F-INH PET signal and the lesions on CT did not perfectly correlate. As INH is only active against actively dividing bacilli, it is possible that unlabeled lesions may have contained quiescent, or dormant bacilli. It is for this reason that INH is typically administered over the course of several months of treatment. Infected BALB/C mice in contrast do not form granulomas and demonstrated a pattern 2-[^{18}F]F-INH activity consistent with diffuse infection. Given the minor amplitude(1.6:1) of the 2-[^{18}F]F-INH signal in Mtb infected mice, we also recognize that decreased elimination of tracer may be contributing to a nonspecific blood pooling effect. However, the similar pattern of 2-[^{18}F]F-INH activity in the liver between infected and uninfected mice would argue against this as the dominant process.

In the analysis of the brain field, we found that 2-[^{18}F]F-INH activity peaked 15 minutes after administration, consistent with the known rapid transit of INH across the blood brain barrier[80]. In infected animals, 2-[^{18}F]F-INH activity trended towards greater accumulation in the brain. While not specifically assayed, we speculate that the infected animals may have been burdened with TB meningitis, a manifestation of disease that is often difficult to diagnose[89,90].

Inconsistent, or incomplete Mtb treatment has led to the emergence of drug resistant strains[196]. The World Health Organization (WHO) has set a goal for elimination of TB by 2050, but multidrug resistant (MDR) and extensively drug resistant (XDR) strains threaten the ability to effectively treat the infection[197]. With the alarming rise of drug resistant Mtb strains, accounting for up to 20% and 2% respectively of global TB[198], there is significant interest in developing not only new drugs, but novel biomarkers to monitor TB therapy. The TB Trials Consortium (TBTC) has expressed an urgent need for development of validated biomarkers for monitoring TB treatments and for detecting relapse after completion of TB treatments[199]. Jain and coworkers have previously utilized pulmonary [^{18}F]FDG to monitor the response to treatment[194]. FDG is a general, non-specific marker of metabolic activity that cannot discriminate inflammation from infection[200], and furthermore assumes normal leukocyte function for tracer uptake at the site of infection. Bacteria specific imaging tracers are urgently needed that can identify foci of infection regardless of the host immune state. The use of PET technology is therefore not only useful for preclinical pharmacokinetic analysis, but potentially also for the diagnosis and monitoring of antibiotic therapy.

Experimental Section

General

Chemicals used in the study were all purchased from commercial vendors and were used without further purification except where stated. Acetonitrile was stored over molecular sieves in N_2. $[^{18}F]F^-$ was purchased from PETNET Solutions Inc. (Philadelphia, PA) in the form of NaF on ion-exchange resin. Chemical and radiochemical purities were determined by a TLC and an analytical HPLC system equipped with both UV and radioactivity detector. The purities of the intermediate and the final products were > 95%.

Synthesis

Synthesis of ethyl 2-(dimethylamino)pyridine-4-carboxylate[188]

500 mg (3 mmol) 2-(N,N-dimethylamino)pyridine-4-carboxylic acid were dissolved in 25 ml EtOH with 0.5 ml of H_2SO_4. The mixture was heated to 90°C and refluxed for 12 hrs before quenching with 0.1M K_2CO_3. The pH of the solution was adjusted to 8, and then 3 portions of 30 ml ether were added to extract the crude product. The 3 portions of ether were combined together and washed with saturated $NaHCO_3$. The ether was removed by rotary evaporation and the resulting crude product was purified by automated column chromatography with silica gel using a mobile phase of 25% ethyl acetate/75% petroleum ether. The product was a yellow liquid and the yield was 62%. ^1H NMR (300MHz, $CDCl_3$) δ: 8.26 (d, J = 5.1 1H), 7.11 (s, 1H), 7.05 (d, J = 4.8 1H),

4.38 (q, *J* = 7.2 2H), 3.14(s, 6H), 1.40(t, *J* = 6.9 3H). ESI calcd for $[M + H]^+$ m/z = 195, found 195.

Synthesis of ethyl-2-(trimethylammonium)-4-pyridine carboxylate triflate (1)[188]

Compound **1** (350 mg, 1.8 mmol) was dissolved in 5 ml CH_2Cl_2. The temperature of the solution was reduced to -78°C prior to the slow addition of methyl trilfate (296 mg, 1.8mmol). The reaction was warmed to room temperature and kept at RT for 24 hrs. The solvent was removed by rotary evaporation and the resulting yellow solid was washed with cold ether. The crude product was recrystallized in ethyl acetate. The product was a white solid and the yield was 25%. ^1H NMR (300MHz, $CDCl_3$) δ: 8.75 (d, *J* = 4.8 1H), 8.40 (s, 1H), 8.14 (d, *J* = 4.5 1H), 4.49 (q, *J* = 7.2 2H), 3.81(s, 9H), 1.45(t, *J* = 6.9 3H). ESI calcd for $[M \text{ (positive portion)}]^+$ m/z = 209, found 209. ESI calcd for $[M \text{ (negative portion)}]^-$ m/z =149, found 149.

Synthesis of 2-F-INH[201]

1 g (7 mmol) of 2-fluoropyridine-4-carboxylic acid was dissolved in 30 ml of THF, and 1,1'-carbonyldiimidazole (CDI, 8.4 mmol) was added to the solution. The mixture was stirred at RT for 1 hr prior to addition of 336 mg (10.5 mmol) of N_2H_4. After 6 hrs, the solvent was removed by rotary evaporation, and the resulting crude product was purified by automated column chromatography using a mobile phase of 2% MeOH/98% CH_2Cl_2. The product was a white solid and the yield was 70%. ^1H NMR (300MHz, $CDCl_3$)

δ: 8.35 (d, *J* = 5.2 1H), 7.65 (d, *J* = 5.6 1H), 7.42 (s, 1H), 4.62 (s, 1H). ESI calcd for $[M+H]^+$ m/z = 156, found 156

Radiosynthesis of 2-$[^{18}F]$F-INH (3)[188]

The development of radiosynthesis was started at Dr. Hooker's lab (Harvard Medical School), and finalized at Dr. Fowler's lab (BNL). The radiosynthesis for imaging studies were done at Dr. Pomper's lab (Johns Hopkins Medical Center). Aqueous $[^{18}F]$KF was eluted from the resin with 1 ml K_2CO_3 (1mg) in MeCN/H_2O solution (900 μl/100 μl) into a Reacti-Vial preloaded with 5 mg Kryptofix 2.2.2.. The solution was azeotropically dried with additional aliquots of MeCN at 105°C. 2mg of **1** was dissolved in 300 μl MeCN and the whole solution was added to the Reacti-Vial. The sealed Reacti-Vial was heated at 105°C for 2 min before it was quenched by addition of 3 ml cold H_2O. The mixture contained the intermediate **2** was loaded on C-18 Sep-Pak and the Sep-Pak was flushed with additional 5 ml H_2O, followed by 5 min helium blow. The resulting dried **2** was eluted into a reaction vial preloaded with 50 μl of $N_2H_4 \cdot H_2O$ with 300μl MeCN. The mixture was heated for 6 min and purged with N_2 for 2 min prior to quenching with 1.5 ml H_2O. The resulting solution was loaded onto a semipreparative HPLC column (Phenomenex, Luna PFP 250 × 10, 5 μm) operated at a 5 ml/min flow rate with a mobile phase consisting of 5% MeCN/95% H_2O. The product was collected at the expected retention time (10 min) and the solvent was removed by rotary evaporation. After dilution with 1-2 ml of saline, the solution was filtered through an Acrodisc 13 mm syringe filter equipped with a 0.2 μm Supor membrane (Pall Corporation, Ann Arbor, MI) into a sterile vial. Radiochemical purity was determined by reverse-phase analytical HPLC using a Phenomenex, PFP, 250 × 4.6, 5 μm column operated at 1 ml/min flow rate using a mobile phase of 5% MeCN/95% H_2O. In addition, the radiochemically purity was verified using TLC (10% MeOH/90%CH_2Cl_2) by cospotting the labeled product with a standard.

Inactivation of InhA by INH or 2-F-INH

The Mtb enoyl-ACP reductase (InhA) was expressed and purified as previously described[202] and catalase-peroxidase (KatG) was kindly obtained as a gift from Dr. Magliozzo (CUNY, Brooklyn College). *Trans*-2-dodecenoyl-CoA (DD-CoA) was synthesized from *trans*-dodecenoic acid by using the mixed anhydride method as previously described[203]. Aliquots of the substrate were flash frozen in liquid N_2 and stored at - 80 °C. All solutions of INH, F-INH, β-NADH, and β- NAD^+ were prepared daily and stored on ice. InhA (0.5 μM) was incubated with 0.5 μM KatG, 50 μM NAD^+, 50 μM INH (or 2-F-INH), and 2 mM EDTA in a total volume of 1.0 mL at 25 °C in InhA buffer (30 mM PIPES, 150 mM NaCl, pH 6.8). The enzyme was stabilized by the addition of glycerol (8%, v/v). Aliquots (60 μl) were taken at defined time points, and residual InhA activity was measured. Enzyme kinetic assays were performed on a Cary 100 Bio spectrophotometer (Varian) in InhA buffer by following the oxidation of NADH to NAD^+ at 340 nm. InhA activity was monitored by adding DDCoA (20 μM) to assay mixtures containing NADH (250 μM) and aliquots from the inactivation reaction. The residual InhA activity at each time point was normalized to 100%, using the value measured at time zero[193].

Adduct formation between NAD and INH or 2-F-INH

A mixture of 0.5 μM KatG, 50 μM NAD^+ and 50 μM INH (or 2-F-INH) was incubated in a total volume of 1.0 ml at 25 °C in InhA buffer (30 mM PIPES, 150 mM NaCl, pH 6.8). Aliquots of solution were taken at 30 min and 1 hr, and each aliquot was filtered through centricon (10,000 NMWL) prior to injection onto the HPLC. Peaks were monitored by reverse-phase analytical HPLC using a Phenomenex, Luna C-18, 250 × 4.6, 5 μm column operated at 1 ml/min flow rate using gradient: 0-20 min, from 100% water to 20% MeCN/80% water and dual channel UV detection at 260 nm and 326 nm. Peaks eluted around 12-15 min with UV absorption ratio between 260 and 326 is 3.2-3.8 were selected as adduct.

In vitro 2-[^{18}F]-INH uptake

2-[^{18}F]-INH uptake *in vitro* was measured using wild-type Mtb ($H_{37}R_v$) from -80°C frozen stock as well as INH-resistant strains *katG* W149R, *katG* M1A and *inhA* T(-8) kindly provided by Dr. Eric Nuermberger [192]. Five independent cultures of each strain and heat killed controls were grown in Middlebrook 7H9 broth supplemented with 10% oleic acid-albumin-dextrose-catalase (Difco, Detroit, MI) and 0.05% Tween 80 (Sigma). Each culture was grown at 37°C with rapid agitation to a OD600 of at 0.3. F-INH (20 μCi) were placed in each culture at time 0. At each time point 0.5 ml of culture was sampled, pelleted by centrifugation and washed twice with PBS, resuspended in 0.5 ml of PBS and transferred to culture tubes for heat inactivation (90°C for 20 min). Radioactivity Measurements were done at time 0, 60, 120, 240, 360 and 480 min. Samples were transferred to the gamma counter (1282 Compugamma CS, LKB Wallac Instruments) for measurement. Background counts were subtracted from sample counts. Heat killed negative controls of each culture were generated by exposure to the 90°C water bath for 20 min. Positive controls used ^{18}F-FDG as tracer on the same cultures at the same time points. In order to determine CFUs, samples from time 0 and 480 minutes for each strain were plated on 7H11 plates. Plates were incubated for 4 weeks at 37°C in a 5% CO_2 environment before CFU counts were determined. MIC_{99} values were determined for each strain with INH and F-INH by the broth macro-dilution method (National Committee for Clinical Laboratory Standards M07-A8).

Animal experiments

Protocols were approved by the Johns Hopkins Biosafety, Radiation Safety and Animal Care and Use Committees.

In vivo aerosol infection

Five- to six-week-old female BALB/c (Charles River) or C3HeB/FeJ (Jackson Laboratory) mice were aerosol infected with 2.5×10^2 CFU of Mtb H37Rv, using the

Middlebrook inhalation exposure system (Glas-Col) with a log-phase broth culture. Three mice were sacrificed at 1 day, 6 weeks, 8 weeks (BALB/c) or 17 weeks (C3HeB/FeJ) after infection to determine the number of bacilli implanted in the lungs and the bacillary burden at the time of imaging. The entire lungs were homogenized in PBS and plated onto Middlebrook 7H11 selective plates (Becton Dickinson). All plates were incubated at 37°C for 4 weeks before the colonies were counted. A separate group of identically infected mice were used for imaging studies.

Bio-containment and anesthesia

All live Mtb infected animals were imaged within a sealed **Minerve** small-animal environment System (Bioscan). Two 0.22 μm 60 mm disc VACU-GUARD (Whatman) filters were used in series at both the inlet and the outlet to contain the bacteria within the device. A standard small animal anesthesia machine was used to deliver a mixture of Isoflurane (Henry Schein) and oxygen during transport and imaging. Animals were anesthetized, a 30 gauge needle (BD Bioscience) was attached to polyethylene-10 tubing (Braintree Scientific) was inserted into the lateral tail vein of BALB/c mice as a catheter for tracer delivery. Animals were sealed inside the bio-containment device in the biosafety level 3 facility and the external surfaces of the bio-containment device was decontaminated and transported to the imaging suite. During prolonged anesthesia (> 20 min), an infrared thermometer and a heat-lamp were used to measure and maintain ambient air temperature inside the bio-containment device.

[^{18}F]-FDG-PET/CT imaging

The night before each imaging time-point, mice were fasted for 12 hrs. Water was provided *ad libitum*. On the day of imaging, each mouse was weighed, injected with 200 µCi of [^{18}F]FDG via the tail vein and imaged 45 min post-injection using the Mosaic HP (Philips) Small Animal PET imager with 15 min static acquisition. A CT scan was also performed at the same time using the NanoSPECT/CT (BIOSCAN) *in vivo* animal imager. PET images were reconstructed and co-registered with CT images. Three mice were used for each group.

2-[^{18}F]-INH-PET/CT imaging

One week after PET scan with [^{18}F]-FDG, the same C3HeB/FeJ mice were weighed, injected with 200 µCi of 2-[^{18}F]-INH via the tail vein and imaged 20 min post-injection using the Mosaic HP (Philips) Small Animal PET images with 10 minute dynamic acquisition windows for 120 min. Infected and uninfected controls were scanned two at a time as matched pairs. BALB/C mice were likewise weighed, anesthetized and sealed in biosafety level 3 biocontainer, but were injected with 200 µCi of 2-[^{18}F]F-INH via the tail vein catheter at the start of image acquisition, and dynamic windows were set for 5 2-minute windows, followed by 10 5-minute windows for a total scan time of 60 minutes. CT scans were immediately performed subsequent to PET imaging using the NanoSPECT/CT (BIOSCAN) *in vivo* animal imager. PET data were reconstructed and co-registered with CT images. Images were automatically coregistered and presented using Amira version 5.4.2 (http://www.amira.com), with a resulting 1:1 correspondence.

For semiquantitative analysis, animals were analyzed in groups of three. Each animal CT had two spherical (3 mm diameter) regions of interest (ROI) drawn manually in the lung fields making sure not to overlap the PET-active liver while but single ROIs were outlined for liver and brain. The standard uptake values (SUV) were computed by normalizing the ROI activity for each mouse to the injected dose and animal weight using Amide version 0.9.1. For each group, the mean lung 2-[^{18}F]-INH-PET activity at each time-point was calculated by averaging the normalized lung SUV of all the ROIs in that group. Mean lung 2-[^{18}F]-INH-PET activity at each time-point was also calculated similarly for three uninfected animals used as controls and imaged at the same time.

Statistical analysis.

Statistical comparison between groups was performed using one tail distribution, two sample, unequal variance t-test in Excel 2010 (Microsoft). Data are presented on a linear scale as mean ± standard error for the mean PET activities and on a logarithmic scale as mean ± standard deviation for CFU counts.

Bibliography

(1) Bosch, F.; Rosich, L.: The contributions of Paul Ehrlich to pharmacology: a tribute on the occasion of the centenary of his Nobel Prize. *Pharmacology* **2008**, *82*, 171-179.

(2) Fleming, A.: Penicillin. *Brit Med J* **1941**, *1941*, 386-386.

(3) Wright, G. D.: The antibiotic resistome: the nexus of chemical and genetic diversity. *Nat. Rev. Microbiol.* **2007**, *5*, 175-186.

(4) WHO: Tuberculosis. *WHO Fact Sheets* **2012**.

(5) Paul, S. M.; Mytelka, D. S.; Dunwiddie, C. T.; Persinger, C. C.; Munos, B. H.; Lindborg, S. R.; Schacht, A. L.: How to improve R&D productivity: the pharmaceutical industry's grand challenge. *Nat. Rev. Drug Discov.* **2010**, *9*, 203-214.

(6) Scannell, J. W.; Blanckley, A.; Boldon, H.; Warrington, B.: Diagnosing the decline in pharmaceutical R&D efficiency. *Nat. Rev. Drug Discov.* **2012**, *11*, 191-200.

(7) Langer, O.; Muller, M.: Methods to assess tissue-specific distribution and metabolism of drugs. *Curr. Drug. Metab.* **2004**, *5*, 463-481.

(8) Muller, M.; dela Pena, A.; Derendorf, H.: Issues in pharmacokinetics and pharmacodynamics of anti-infective agents: distribution in tissue. *Antimicrob. Agents Chemother.* **2004**, *48*, 1441-1453.

(9) Derendorf, H.: Pharmacokinetic evaluation of beta-lactam antibiotics. *J. Antimicrob. Chemother.* **1989**, *24*, 407-413.

(10) Parham, F. M.; Kohn, M. C.; Matthews, H. B.; DeRosa, C.; Portier, C. J.: Using structural information to create physiologically based pharmacokinetic models for all polychlorinated biphenyls. *Toxicol. Appl. Pharmacol.* **1997**, *144*, 340-347.

(11) Eichler, H. G.; Muller, M.: Drug distribution. The forgotten relative in clinical pharmacokinetics. *Clin. Pharmacokinet.* **1998**, *34*, 95-99.

(12) Wise, R.: Methods for evaluating the penetration of beta-lactam antibiotics into tissues. *Rev. Infect. Dis.* **1986**, *8 Suppl 3*, S325-32.

(13) Elmquist, W. F.; Sawchuk, R. J.: Application of microdialysis in pharmacokinetic studies. *Pharm. Res.* **1997**, *14*, 267-288.

(14) Westerink, B. H.; Damsma, G.; Rollema, H.; De Vries, J. B.; Horn, A. S.: Scope and limitations of in vivo brain dialysis: a comparison of its application to various neurotransmitter systems. *Life Sci.* **1987**, *41*, 1763-1776.

(15) Fischman, A. J.; Alpert, N. M.; Babich, J. W.; Rubin, R. H.: The role of positron emission tomography in pharmacokinetic analysis. *Drug Metab. Rev.* **1997**, *29*, 923-956.

(16) Bleeker-Rovers, C. P.; Boerman, O. C.; Rennen, H. J.; Corstens, F. H.; Oyen, W. J.: Radiolabeled compounds in diagnosis of infectious and inflammatory disease. *Current pharmaceutical design* **2004**, *10*, 2935-50.

(17) K.J., R.; Ray, C. G.: Sherris Medical Microbiology. *McGraw Hill* **2004**.

(18) Gotthardt, M.; Bleeker-Rovers, C. P.; Boerman, O. C.; Oyen, W. J.: Imaging of inflammation by PET, conventional scintigraphy, and other imaging techniques. *J. Nucl. Med.* **2010**, *51*, 1937-1949.

(19) Ohnishi, K.: Cerebral malaria. *Brain and nerve = Shinkei kenkyu no shinpo* **2009**, *61*, 122-128.

(20) Boss, D. S.; Olmos, R. V.; Sinaasappel, M.; Beijnen, J. H.; Schellens, J. H.: Application of PET/CT in the development of novel anticancer drugs. *The oncologist* **2008**, *13*, 25-38.

(21) Signore, A.; Mather, S. J.; Piaggio, G.; Malviya, G.; Dierckx, R. A.: Molecular imaging of inflammation/infection: nuclear medicine and optical imaging agents and methods. *Chem. Rev.* **2010**, *110*, 3112-3145.

(22) Weissleder, R.; Mahmood, U.: Molecular imaging. *Radiology* **2001**, *219*, 316-333.

(23) Rajagopalan, K. N.; DeBerardinis, R. J.: Role of glutamine in cancer: therapeutic and imaging implications. *J. Nucl. Med.* **2011**, *52*, 1005-1008.

(24) Qu, W.; Oya, S.; Lieberman, B. P.; Ploessl, K.; Wang, L.; Wise, D. R.; Divgi, C. R.; Chodosh, L. A.; Thompson, C. B.; Kung, H. F.: Preparation and characterization of L-[5-11C]-glutamine for metabolic imaging of tumors. *J. Nucl. Med.* **2012**, *53*, 98-105.

(25) Herrmann, K.; Benz, M. R.; Krause, B. J.; Pomykala, K. L.; Buck, A. K.; Czernin, J.: (18)F-FDG-PET/CT in evaluating response to therapy in solid tumors: where we are and where we can go. *Q. J. Nucl. Med. Mol. Imaging* **2011**, *55*, 620-632.

(26) Fowler, J. S.; Logan, J.; Wang, G. J.; Volkow, N. D.; Telang, F.; Zhu, W.; Franceschi, D.; Pappas, N.; Ferrieri, R.; Shea, C.; Garza, V.; Xu, Y.; Schlyer, D.; Gatley, S. J.; Ding, Y. S.; Alexoff, D.; Warner, D.; Netusil, N.; Carter, P.; Jayne, M.; King, P.; Vaska, P.: Low monoamine oxidase B in peripheral organs in smokers. *Proc. Natl. Acad. Sci. U S A* **2003**, *100*, 11600-11605.

(27) Fowler, J. S.; Logan, J.; Wang, G. J.; Franceschi, D.; Volkow, N. D.; Telang, F.; Pappas, N.; Ferrieri, R.; Shea, C.; Garza, V.; Xu, Y.; King, P.; Schlyer, D.; Gatley, S. J.; Ding, Y. S.; Warner, D.; Netusil, N.; Carter, P.; Jayne, M.; Alexoff, D.; Zhu, W.; Vaska, P.: Monoamine oxidase A imaging in peripheral organs in healthy human subjects. *Synapse* **2003**, *49*, 178-187.

(28) Kung, H. F.; Kung, M. P.; Choi, S. R.: Radiopharmaceuticals for single-photon emission computed tomography brain imaging. *Semin. Nucl. Med.* **2003**, *33*, 2-13.

(29) Lister-James, J.; Pontecorvo, M. J.; Clark, C.; Joshi, A. D.; Mintun, M. A.; Zhang, W.; Lim, N.; Zhuang, Z.; Golding, G.; Choi, S. R.; Benedum, T. E.; Kennedy, P.; Hefti, F.; Carpenter, A. P.; Kung, H. F.; Skovronsky, D. M.: Florbetapir f-18: a histopathologically validated Beta-amyloid positron emission tomography imaging agent. *Semin. Nucl. Med.* **2011**, *41*, 300-304.

(30) Clark, C. M.; Schneider, J. A.; Bedell, B. J.; Beach, T. G.; Bilker, W. B.; Mintun, M. A.; Pontecorvo, M. J.; Hefti, F.; Carpenter, A. P.; Flitter, M. L.; Krautkramer, M. J.; Kung, H. F.; Coleman, R. E.; Doraiswamy, P. M.; Fleisher, A. S.; Sabbagh, M. N.; Sadowsky, C. H.; Reiman, E. P.; Zehntner, S. P.; Skovronsky, D. M.; Group, A. A. S.: Use of florbetapir-PET for imaging beta-amyloid pathology. *JAMA : the journal of the American Medical Association* **2011**, *305*, 275-283.

(31) Schuster, A.; Makowski, M. R.; Jansen, C. H.; Gawaz, M.; Botnar, R. M.; Nagel, E.; Bigalke, B.: Platelets in Cardiovascular Imaging. *Curr. Vasc. Pharmacol.* **2012**.

(32) Botnar, R. M.; Makowski, M. R.: Cardiovascular magnetic resonance imaging in small animals. *Prog. Mol. Biol. Transl. Sci.* **2012**, *105*, 227-261.

(33) Roitt, I. M.: Essential immunology. 9th ed. *Blackwell Scientific* **1997**.

(34) Proud, D.; Kaplan, A. P.: Kinin formation: mechanisms and role in inflammatory disorders. *Annu. Rev. Immunol.* **1988**, *6*, 49-83.

(35) Welling, M. M.; Alberto, R.: Performance of a 99mTc-labelled 1-thio-beta-D-glucose 2,3,4,6-tetra-acetate analogue in the detection of infections and tumours in mice: a comparison with [18F]FDG. *Nucl. Med. Commun.* **2010**, *31*, 239-248.

(36) Kosterink, J. G.: Positron emission tomography in the diagnosis and treatment management of tuberculosis. *Curr. Pharm. Des.* **2011**, *17*, 2875-2880.

(37) Kubota, R.; Yamada, S.; Kubota, K.; Ishiwata, K.; Tamahashi, N.; Ido, T.: Intratumoral distribution of fluorine-18-fluorodeoxyglucose in vivo: high accumulation in macrophages and granulation tissues studied by microautoradiography. *J. Nucl. Med.* **1992**, *33*, 1972-1980.

(38) Solanki, K. K.; Mather, S. J.; Janabi, M. A.; Britton, K. E.: A rapid method for the preparation of 99Tcm hexametazime-labelled leucocytes. *Nucl. Med. Commun.* **1988**, *9*, 753-761.

(39) Tewson, T. J.; Yang, D.; Wong, G.; Macy, D.; DeJesus, O. J.; Nickles, R. J.; Perlman, S. B.; Taylor, M.; Frank, P.: The synthesis of fluorine-18 lomefloxacin and its preliminary use in human studies. *Nucl. Med. Biol.* **1996**, *23*, 767-772.

(40) Fayad, Z. A.; Amirbekian, V.; Toussaint, J. F.; Fuster, V.: Identification of interleukin-2 for imaging atherosclerotic inflammation. *Eur. J. Nucl. Med. Mol. Imaging* **2006**, *33*, 111-116.

(41) Signore, A.; Capriotti, G.; Scopinaro, F.; Bonanno, E.; Modesti, A.: Radiolabelled lymphokines and growth factors for in vivo imaging of inflammation, infection and cancer. *Trends in immunology* **2003**, *24*, 395-402.

(42) Britton, K. E.; Wareham, D. W.; Das, S. S.; Solanki, K. K.; Amaral, H.; Bhatnagar, A.; Katamihardja, A. H.; Malamitsi, J.; Moustafa, H. M.; Soroa, V. E.; Sundram, F. X.; Padhy, A. K.: Imaging bacterial infection with (99m)Tc-ciprofloxacin (Infecton). *J. Clin. Pathol.* **2002**, *55*, 817-823.

(43) Dumarey, N.; Blocklet, D.; Appelboom, T.; Tant, L.; Schoutens, A.: Infecton is not specific for bacterial osteo-articular infective pathology. *Eur. J. Nucl. Med. Mol. Imaging* **2002**, *29*, 530-535.

(44) Babich, J. W.; Rubin, R. H.; Graham, W. A.; Wilkinson, R. A.; Vincent, J.; Fischman, A. J.: 18F-labeling and biodistribution of the novel fluoro-quinolone antimicrobial agent, trovafloxacin (CP 99,219). *Nucl. Med. Biol.* **1996**, *23*, 995-998.

(45) Fischman, A. J.; Babich, J. W.; Alpert, N. M.; Vincent, J.; Wilkinson, R. A.; Callahan, R. J.; Correia; Ja; Rubin, R. H.: Pharmacokinetics of 18F-labeled trovafloxacin in normal and Escherichia coli-infected rats and rabbits studied with positron emission tomography. *Clin. Microbiol. Infect.* **1997**, *3*, 379.

(46) Fischman, A. J.; Livni, E.; Babich, J.; Alpert, N. M.; Liu, Y. Y.; Thom, E.; Cleeland, R.; Prosser, B. L.; Callahan, R. J.; Correia, J. A.; et al.: Pharmacokinetics of 18F-labeled fleroxacin in rabbits with Escherichia coli infections, studied with positron emission tomography. *Antimicrobial agents and chemotherapy* **1992**, *36*, 2286-92.

(47) Welling, M. M.; Hiemstra, P. S.; van den Barselaar, M. T.; Paulusma-Annema, A.; Nibbering, P. H.; Pauwels, E. K.; Calame, W.: Antibacterial activity of human neutrophil defensins in experimental infections in mice is accompanied by increased leukocyte accumulation. *J. Clin. Invest.* **1998**, *102*, 1583-1590.

(48) Welling, M. M.; Nibbering, P. H.; Paulusma-Annema, A.; Hiemstra, P. S.; Pauwels, E. K.; Calame, W.: Imaging of bacterial infections with 99mTc-labeled human neutrophil peptide-1. *J. Nucl. Med.* **1999**, *40*, 2073-2080.

(49) Lupetti, A.; Welling, M. M.; Pauwels, E. K.; Nibbering, P. H.: Radiolabelled antimicrobial peptides for infection detection. *Lancet Infect. Dis.* **2003**, *3*, 223-229.

(50) Welling, M. M.; Lupetti, A.; Balter, H. S.; Lanzzeri, S.; Souto, B.; Rey, A. M.; Savio, E. O.; Paulusma-Annema, A.; Pauwels, E. K.; Nibbering, P. H.: 99mTc-labeled

antimicrobial peptides for detection of bacterial and Candida albicans infections. *J. Nucl. Med.* **2001**, *42*, 788-794.

(51) Welling, M. M.; Paulusma-Annema, A.; Balter, H. S.; Pauwels, E. K.; Nibbering, P. H.: Technetium-99m labelled antimicrobial peptides discriminate between bacterial infections and sterile inflammations. *Eur. J. Nucl. Med.* **2000**, *27*, 292-301.

(52) Akhtar, M. S.; Khan, M. E.; Khan, B.; Irfanullah, J.; Afzal, M. S.; Khan, M. A.; Nadeem, M. A.; Jehangir, M.; Imran, M. B.: An imaging analysis of (99m)Tc-UBI (29-41) uptake in S. aureus infected thighs of rabbits on ciprofloxacin treatment. *Eur. J. Nucl. Med. Mol. Imaging* **2008**, *35*, 1056-1064.

(53) Bettegowda, C.; Foss, C. A.; Cheong, I.; Wang, Y.; Diaz, L.; Agrawal, N.; Fox, J.; Dick, J.; Dang, L. H.; Zhou, S.; Kinzler, K. W.; Vogelstein, B.; Pomper, M. G.: Imaging bacterial infections with radiolabeled 1-(2'-deoxy-2'-fluoro-beta-D-arabinofuranosyl)-5-iodouracil. *Proc. Natl. Acad. Sci. U S A* **2005**, *102*, 1145-1150.

(54) Eriksson, S.; Munch-Petersen, B.; Johansson, K.; Eklund, H.: Structure and function of cellular deoxyribonucleoside kinases. *Cell Mol. Life Sci.* **2002**, *59*, 1327-1346.

(55) Blasberg, R. G.; Tjuvajev, J. G.: Molecular-genetic imaging: current and future perspectives. *J. Clin. Invest.* **2003**, *111*, 1620-1629.

(56) Langer, O.; Brunner, M.; Zeitlinger, M.; Ziegler, S.; Muller, U.; Dobrozemsky, G.; Lackner, E.; Joukhadar, C.; Mitterhauser, M.; Wadsak, W.; Minar, E.; Dudczak, R.; Kletter, K.; Muller, M.: In vitro and in vivo evaluation of [18F]ciprofloxacin for the imaging of bacterial infections with PET. *Eur. J. Nucl. Med. Mol. Imaging* **2005**, *32*, 143-150.

(57) Siaens, R. H.; Rennen, H. J.; Boerman, O. C.; Dierckx, R.; Slegers, G.: Synthesis and comparison of 99mTc-enrofloxacin and 99mTc-ciprofloxacin. *J. Nucl. Med.* **2004**, *45*, 2088-2094.

(58) Singh, N.; Bhatnagar, A.: Clinical Evaluation of Efficacy of (99m)TC - Ethambutol in Tubercular Lesion Imaging. *Tuberc. Res. Treat.* **2010**, *2010*, 618051.

(59) Singh, A.; Bhatnagar; . Tc-99m-Isoniazid (INH): A specific mycobacterial lesion imaging agent. *J. Nucl. Med.* **2008**, *49*, 309P.

(60) Koukourakis, G.; Maravelis, G.; Koukouraki, S.; Padelakos, P.; Kouloulias, V.: Overview of positron emission tomography chemistry: clinical and technical considerations and combination with computed tomography. *J. BUON.* **2009**, *14*, 575-580.

(61) Bonte, F. J.: Nuclear Medicine Pioneer Citation, 1976: David E. Kuhl, M.D. *J. Nucl. Med.* **1976**, *17*, 518-519.

(62) Karp, J. S.; Muehllehner, G.; Mankof, F. D.; Ordonez, C. E.; Ollinger, J. M.; Daube-Witherspoon, M. E.; Haigh, A. T.; Beerbohm, D. J.: Continuous-slice PENN-PET: a positron tomograph with volume imaging capability. *J. Nucl. Med.* **1990**, *31*, 617-627.

(63) Ter-Pogossian, M. M.; Phelps, M. E.; Hoffman, E. J.; Mullani, N. A.: A positron-emission transaxial tomograph for nuclear imaging (PETT). *Radiology* **1975**, *114*, 89-98.

(64) Phelps, M. E.; Hoffman, E. J.; Mullani, N. A.; Ter-Pogossian, M. M.: Application of annihilation coincidence detection to transaxial reconstruction tomography. *J. Nucl. Med.* **1975**, *16*, 210-224.

(65) A Vital Legacy: Biological and Environmental Research in the Atomic Age. *U.S. Department of Energy, The Office of Biological and Environmental Research* **2010**, 25-26.

(66) Ido, T.; Wan, C. N.; Casella, V.; Fowler, J. S.; Wolf, A. P.; Reivich, M.; Kuhl, D. E.: Labeled 2-Deoxy-D-Glucose Analogs - F-18-Labeled 2-Deoxy-2-Fluoro-D-Glucose, 2-Deoxy-2-Fluoro-D-Mannose and C-14-2-Deoxy-2-Fluoro-D-Glucose. *J. Labelled. Compd. Rad.* **1978**, *14*, 175-183.

(67) Miller, P. W.; Long, N. J.; Vilar, R.; Gee, A. D.: Synthesis of 11C, 18F, 15O, and 13N radiolabels for positron emission tomography. *Angew. Chem. Int. Ed. Engl.* **2008**, *47*, 8998-9033.

(68) Turkington, T. G.: Introduction to PET instrumentation. *J. Nucl. Med. Technol.* **2001**, *29*, 4-11.

(69) Bida, G. T.; T.J., R.; A.P., W.: Experimental determined thick target yilds for the 14N(p,α)11C reaction. *Radiochimica Acta* **1980**, *27*, 181-185.

(70) Langstrom, B.; Antoni, G.; Gullberg, P.; Halldin, C.; Malmborg, P.; Nagren, K.; Rimland, A.; Svard, H.: Synthesis of L- and D-[methyl-11C]methionine. *J. Nucl. Med.* **1987**, *28*, 1037-1040.

(71) Link, J. M.; Krohn, K. A.; Clark, J. C.: Production of [11C]CH3I by single pass reaction of [11C]CH4 with I2. *Nucl. Med. Biol.* **1997**, *24*, 93-7.

(72) Jewett, D. M.: A simple synthesis of [11C]methyl triflate. *Int. J. Rad. Appl. Instrum. A* **1992**, *43*, 1383-1385.

(73) Iwata, R.; Ido, T.; Takahashi, T.; Nakanishi, H.; Iida, S.: Optimization of [11C]HCN production and no-carrier-added [1-11C]amino acid synthesis. *Int. J. Rad. Appl. Instrum. A* **1987**, *38*, 97-102.

(74) Nishijima, K.; Kuge, Y.; Seki, K.; Ohkura, K.; Motoki, N.; Nagatsu, K.; Tanaka, A.; Tsukamoto, E.; Tamaki, N.: A simplified and improved synthesis of [11C]phosgene with iron and iron (III) oxide. *Nucl. Med. Biol.* **2002**, *29*, 345-350.

(75) Hooker, J. M.; Schonberger, M.; Schieferstein, H.; Fowler, J. S.: A simple, rapid method for the preparation of [11C]formaldehyde. *Angew. Chem. Int. Ed. Engl.* **2008**, *47*, 5989-5992.

(76) Casella, V.; Ido, T.; Wolf, A. P.; Fowler, J. S.; MacGregor, R. R.; Ruth, T. J.: Anhydrous F-18 labeled eslemental flurine for radiopharmaceutical preparation. *J. Nucl. Med.* **1980**, *21*, 750-7.

(77) Wilson, A. A.; Garcia, A.; Jin, L.; Houle, S.: Radiotracer synthesis from [(11)C]-iodomethane: a remarkably simple captive solvent method. *Nucl. Med. Biol.* **2000**, *27*, 529-532.

(78) Hamill, T. G.; Krause, S.; Ryan, C.; Bonnefous, C.; Govek, S.; Seiders, T. J.; Cosford, N. D.; Roppe, J.; Kamenecka, T.; Patel, S.; Gibson, R. E.; Sanabria, S.; Riffel, K.; Eng, W.; King, C.; Yang, X.; Green, M. D.; O'Malley, S. S.; Hargreaves, R.; Burns, H. D.: Synthesis, characterization, and first successful monkey imaging studies of metabotropic glutamate receptor subtype 5 (mGluR5) PET radiotracers. *Synapse* **2005**, *56*, 205-216.

(79) Roeda, D.; Tavitian, B.; Coulon, C.; David, F.; Dolle, F.; Fuseau, C.; Jobert, A.; Crouzel, C.: Synthesis of [11C]RPR-72840A and its evaluation as a radioligand for the serotonin reuptake site in positron emission tomography. *Bioorg. Med. Chem.* **1997**, *5*, 397-403.

(80) Liu, L.; Xu, Y.; Shea, C.; Fowler, J. S.; Hooker, J. M.; Tonge, P. J.: Radiosynthesis and bioimaging of the tuberculosis chemotherapeutics isoniazid, rifampicin and pyrazinamide in baboons. *J. Med. Chem.* **2010**, *53*, 2882-2891.

(81) Hooker, J. M.; Reibel, A. T.; Hill, S. M.; Schueller, M. J.; Fowler, J. S.: One-pot, direct incorporation of [11C]CO2 into carbamates. *Angew. Chem. Int. Ed. Engl.* **2009**, *48*, 3482-5.

(82) Kilbourn, M. R.; Welch, M. J.; Dence, C. S.; Tewson, T. J.; Saji, H.; Maeda, M.: Carrier-added and no-carrier-added syntheses of [18F]spiroperidol and [18F]haloperidol. *Int. J. Appl. Radiat. Isot.* **1984**, *35*, 591-598.

(83) Hamacher, K.; Coenen, H. H.; Stocklin, G.: Efficient stereospecific synthesis of no-carrier-added 2-[18F]-fluoro-2-deoxy-D-glucose using aminopolyether supported nucleophilic substitution. *J. Nucl. Med.* **1986**, *27*, 235-238.

(84) Bloom, B. R.; Murray, C. J.: Tuberculosis: commentary on a reemergent killer. *Science* **1992**, *257*, 1055-1064.

(85) Kochi, A.: The global tuberculosis situation and the new control strategy of the World Health Organization. *Tubercle* **1991**, *72*, 1-6.

(86) Rattan, A.; Kalia, A.; Ahmad, N.: Multidrug-resistant *Mycobacterium tuberculosis*: molecular perspectives. *Emerg. Infect. Dis.* **1998**, *4*, 195-209.

(87) Bass, J. B., Jr.; Farer, L. S.; Hopewell, P. C.; O'Brien, R.; Jacobs, R. F.; Ruben, F.; Snider, D. E., Jr.; Thornton, G.: Treatment of tuberculosis and tuberculosis infection in adults and children. American Thoracic Society and The Centers for Disease Control and Prevention. *Am. J. Respir. Crit. Care Med.* **1994**, *149*, 1359-1374.

(88) American Thoracic Society. Medical Section of the American Lung Association: Treatment of tuberculosis and tuberculosis infection in adults and children. *Am. Rev. Respir. Dis.* **1986**, *134*, 355-363.

(89) Thwaites, G.; Fisher, M.; Hemingway, C.; Scott, G.; Solomon, T.; Innes, J.: British Infection Society guidelines for the diagnosis and treatment of tuberculosis of the central nervous system in adults and children. *J. Infect.* **2009**, *59*, 167-187.

(90) Thwaites, G. E.; Tran, T. H.: Tuberculous meningitis: many questions, too few answers. *Lancet Neurol.* **2005**, *4*, 160-170.

(91) Nau, R.; Sorgel, F.; Prange, H. W.: Pharmacokinetic optimisation of the treatment of bacterial central nervous system infections. *Clin. Pharmacokinet.* **1998**, *35*, 223-246.

(92) Kniess, T.; Rode, K.; Wuest, F.: Practical experiences with the synthesis of $[^{11}C]CH_3I$ through gas phase iodination reaction using a $TRACERlabFX_C$ synthesis module. *Appl. Radiat. Isot.* **2008**, *66*, 482-488.

(93) Andersson, I.; Bergstroem, M.; Laanstroem, B.: Synthesis of ^{11}C-labelled benzamide compounds as potential tracers for poly(ADP-ribose) synthetase. *Appl. Radiat. Isot.* **1994**, *45*, 707-714.

(94) Milic, D. R.; Opsenica, D. M.; Adnadevic, B.; Solaja, B. A.: NaY zeolite: A useful catalyst for nitrile hydrolysis. *Molecules* **2000**, *5*, 118-126.

(95) Elias, G.; Bauer, W. F.: Hydrazine determination in sludge samples by high-performance liquid chromatography. *J. Sep. Sci.* **2006**, *29*, 460-464.

(96) Woo, J.; Cheung, W.; Chan, R.; Chan, H. S.; Cheng, A.; Chan, K.: In vitro protein binding characteristics of isoniazid, rifampicin, and pyrazinamide to whole plasma, albumin, and α-1-acid glycoprotein. *Clin. Biochem.* **1996**, *29*, 175-177.

(97) Nguyen, D. T.; Guillarme, D.; Rudaz, S.; Veuthey, J. L.: Validation of an ultra-fast UPLC-UV method for the separation of antituberculosis tablets. *J. Sep. Sci.* **2008**, *31*, 1050-1056.

(98) Nau, R.; Prange, H. W.; Menck, S.; Kolenda, H.; Visser, K.; Seydel, J. K.: Penetration of rifampicin into the cerebrospinal fluid of adults with uninflamed meninges. *J. Antimicrob. Chemother.* **1992**, *29*, 719-724.

(99) McDougall, A. C.; Rose, J. A.; Grahame-Smith, D. G.: Penetration of C^{14}-labelled rifampicin into primate peripheral nerve. *Experientia* **1975**, *31*, 1068-1069.

(100) Mindermann, T.; Landolt, H.; Zimmerli, W.; Rajacic, Z.; Gratzl, O.: Penetration of rifampicin into the brain tissue and cerebral extracellular space of rats. *J. Antimicrob. Chemother.* **1993**, *31*, 731-737.

(101) Mindermann, T.; Zimmerli, W.; Gratzl, O.: Rifampin concentrations in various compartments of the human brain: a novel method for determining drug levels in the cerebral extracellular space. *Antimicrob. Agents Chemother.* **1998**, *42*, 2626-2629.

(102) Barclay, W. R.; Ebert, R. H.; Le Roy, G. V.; Manthei, R. W.; Roth, L. J.: Distribution and excretion of radioactive isoniazid in tuberculous patients. *J. Am. Med. Assoc.* **1953**, *151*, 1384-1388.

(103) Barling, R. W.; Selkon, J. B.: The penetration of antibiotics into cerebrospinal fluid and brain tissue. *J. Antimicrob. Chemother.* **1978**, *4*, 203-227.

(104) Rouse, D. A.; Li, Z.; Bai, G. H.; Morris, S. L.: Characterization of the katG and inhA genes of isoniazid-resistant clinical isolates of *Mycobacterium tuberculosis*. *Antimicrob. Agents Chemother.* **1995**, *39*, 2472-2477.

(105) Roth, L. J.; Manthel, R. W.: The distribution of C^{14} labeled isonicotinic acid hydrazide in normal mice. *Proc. Soc. Exp. Biol. Med.* **1952**, *81*, 566-569.

(106) Barlow, C. F.; Schoolar, J. C.; Roth, L. J.: Distribution of carbon-14 labeled isoniazid in brain. *Neurology* **1957**, *7*, 820-824.

(107) Schoolar, J. C.; Barlow, C. F.; Roth, L. J.: Autoradiography of carbon-14 labeled isoniazid in brain. *Proc. Soc. Exp. Biol. Med.* **1956**, *91*, 347-349.

(108) Ellard, G. A.; Humphries, M. J.; Allen, B. W.: Cerebrospinal fluid drug concentrations and the treatment of tuberculous meningitis. *Am. Rev. Respir. Dis.* **1993**, *148*, 650-655.

(109) Forgan-Smith, R.; Ellard, G. A.; Newton, D.; Mitchison, D. A.: Pyrazinamide and other drugs in tuberculous meningitis. *Lancet* **1973**, *2*, 374.

(110) Wu, J.-W.; Shih, H.-H.; Wang, S.-C.; Tsai, T.-H.: Determination and pharmacokinetic profile of pyrazinamide in rat blood, brain and bile using microdialysis coupled with high-performance liquid chromatography and verified by tandem mass spectrometry. *Anal. Chim. Acta* **2004**, *522*, 231-239.

(111) Nitti, V.; Virgilio, R.; Patricolo, M. R.; Iuliano, A.: Pharmacokinetic study of intravenous rifampicin. *Chemotherapy* **1977**, *23*, 1-6.

(112) Furesz, S.; Scotti, R.; Pallanza, R.; Mapelli, E.: Rifampicin: a new rifamycin. 3. Absorption, distribution, and elimination in man. *Arzneimittelforschung* **1967**, *17*, 534-537.

(113) Boman, G.: Tissue distribution of ^{14}C-rifampicin II. Accumulation in melanin-containing structures. *Acta Pharmacol. Toxicol. (Copenh)* **1975**, *36*, 267-283.

(114) Verma, R. K.; Kaur, J.; Kumar, K.; Yadav, A. B.; Misra, A.: Intracellular time course, pharmacokinetics, and biodistribution of isoniazid and rifabutin following pulmonary delivery of inhalable microparticles to mice. *Antimicrob. Agents Chemother.* **2008**, *52*, 3195-3201.

(115) Roohi, S.; Mushtaq, A.; Jehangir, M.; Malik, S. A.: Direct labeling of isoniazid with technetium-99m for diagnosis of tuberculosis. *Radiochim. Acta* **2006**, *94*, 147-152.

(116) Stottmeier, K. D.; Beam, R. E.; Kubica, G. P.: The absorption and excretion of pyrazinamide. I. Preliminary study in laboratory animals and in man. *Am. Rev. Respir. Dis.* **1968**, *98*, 70-74.

(117) Peloquin, C. A.; Jaresko, G. S.; Yong, C. L.; Keung, A. C.; Bulpitt, A. E.; Jelliffe, R. W.: Population pharmacokinetic modeling of isoniazid, rifampin, and pyrazinamide. *Antimicrob. Agents Chemother.* **1997**, *41*, 2670-2679.

(118) Lacroix, C.; Hoang, T. P.; Nouveau, J.; Guyonnaud, C.; Laine, G.; Duwoos, H.; Lafont, O.: Pharmacokinetics of pyrazinamide and its metabolites in healthy subjects. *Eur. J. Clin. Pharmacol.* **1989**, *36*, 395-400.

(119) Zhang, Y.; Heym, B.; Allen, B.; Young, D.; Cole, S.: The catalase-peroxidase gene and isoniazid resistance of Mycobacterium tuberculosis. *Nature* **1992**, *358*, 591-593.

(120) Blanchard, J. S.: Molecular mechanisms of drug resistance in *Mycobacterium tuberculosis*. *Annu. Rev. Biochem.* **1996**, *65*, 215-239.

(121) Rawat, R.; Whitty, A.; Tonge, P. J.: The isoniazid-NAD adduct is a slow, tight-binding inhibitor of InhA, the *Mycobacterium tuberculosis* enoyl reductase: adduct affinity and drug resistance. *Proc. Natl. Acad. Sci. U. S. A.* **2003**, *100*, 13881-13886.

(122) Yarbrough, L. R.; Wu, F. Y.; Wu, C. W.: Molecular mechanism of the rifampicin -RNA polymerase interaction. *Biochemistry* **1976**, *15*, 2669-2676.

(123) Mao, J.; Wang, Y.; Wan, B.; Kozikowski, A. P.; Franzblau, S. G.: Design, synthesis, and pharmacological evaluation of mefloquine-based ligands as novel antituberculosis agents. *ChemMedChem* **2007**, *2*, 1624-1630.

(124) Glamkowski, E. J.; Reitano, P. A.; Woodward, D. L.: Synthesis of 3-(4-acylaminopiperazin-1-ylalkyl)indoles as potential antihypertensive agents. *J. Med. Chem.* **1977**, *20*, 1485-1489.

(125) Loening, A. M.; Gambhir, S. S.: AMIDE: a free software tool for multimodality medical image analysis. *Mol. Imaging* **2003**, *2*, 131-137.

(126) Balemans, W.; Lounis, N.; Gilissen, R.; Guillemont, J.; Simmen, K.; Andries, K.; Koul, A.: Essentiality of FASII pathway for Staphylococcus aureus. *Nature* **2010**, *463*, E3; discussion E4.

(127) Escaich, S.; Prouvensier, L.; Saccomani, M.; Durant, L.; Oxoby, M.; Gerusz, V.; Moreau, F.; Vongsouthi, V.; Maher, K.; Morrissey, I.; Soulama-Mouze, C.: The MUT056399 inhibitor of FabI is a new antistaphylococcal compound. *Antimicrob. Agents Chemother.* **2011**, *55*, 4692-4697.

(128) Luckner, S. R.; Liu, N.; am Ende, C. W.; Tonge, P. J.; Kisker, C.: A slow, tight binding inhibitor of InhA, the enoyl-acyl carrier protein reductase from Mycobacterium tuberculosis. *J. Biol. Chem.* **2010**, *285*, 14330-14337.

(129) Kluytmans, J.; van Belkum, A.; Verbrugh, H.: Nasal carriage of Staphylococcus aureus: epidemiology, underlying mechanisms, and associated risks. *Clin. Microbiol. Rev.* **1997**, *10*, 505-520.

(130) Klein, E.; Smith, D. L.; Laxminarayan, R.: Hospitalizations and deaths caused by methicillin-resistant Staphylococcus aureus, United States, 1999-2005. *Emerg. Infect. Dis.* **2007**, *13*, 1840-1846.

(131) Wang, A.: Recent progress in the understanding of infective endocarditis. *Curr. Treat. Options Cardiovasc. Med.* **2011**, *13*, 586-594.

(132) Lee, J. I.; Kim, K. S.; Oh, B. C.; Kim, N. A.; Kim, I. H.; Park, C. G.; Kim, S. J.: Acute necrotic stomatitis (noma) associated with methicillin-resistant Staphylococcus aureus infection in a newly acquired rhesus macaque (Macaca mulatta). *J. Med. Primatol.* **2011**, *40*, 1188-93.

(133) van Rijen, M. M.; Kluytmans, J. A.: New approaches to prevention of staphylococcal infection in surgery. *Curr. Opin. Infect. Dis.* **2008**, *21*, 380-384.

(134) Nassisi, D.; Oishi, M. L.: Evidence-based guidelines for evaluation and antimicrobial therapy for common emergency department infections. *Emerg. Med. Pract.* **2012**, *14*, 1-28; quiz 28-9.

(135) Que, Y. A.; Moreillon, P.: Infective endocarditis. *Nat. Rev. Cardiol.* **2011**, *8*, 322-336.

(136) Sipahi, O. R.; Bardak, S.; Turhan, T.; Arda, B.; Pullukcu, H.; Ruksen, M.; Aydemir, S.; Dalbasti, T.; Yurtseven, T.; Zileli, M.; Ulusoy, S.: Linezolid in the treatment of methicillin-resistant staphylococcal post-neurosurgical meningitis: a series of 17 cases. *Scand. J. Infect. Dis.* **2011**, *43*, 757-764.

(137) Quintiliani, R.; Cooper, B. W.: Current concepts in the treatment of staphylococcal meningitis. *J. Antimicrob. Chemother.* **1988**, *21 Suppl C*, 107-114.

(138) Ramaswamy, S. V.; Reich, R.; Dou, S. J.; Jasperse, L.; Pan, X.; Wanger, A.; Quitugua, T.; Graviss, E. A.: Single nucleotide polymorphisms in genes associated with isoniazid resistance in Mycobacterium tuberculosis. *Antimicrob. Agents Chemother.* **2003**, *47*, 1241-1250.

(139) Sullivan, T. J.; Truglio, J. J.; Boyne, M. E.; Novichenok, P.; Zhang, X.; Stratton, C. F.; Li, H.-J.; Kaur, T.; Amin, A.; Johnson, F.; Slayden, R. A.; Kisker, C.; Tonge, P. J.: High

Affinity InhA Inhibitors With Activity Against Drug Resistant Strains of *Mycobacterium Tuberculosis*. *ACS Chem. Biol.* **2006**, *1*, 43-53.

(140) Pan, P.; Tonge, P. J.: Targeting InhA, the FASII enoyl-ACP reductase: SAR studies on novel inhibitor scaffolds. *Curr. Top. Med. Chem.* **2012**, *12*, 672-693.

(141) am Ende, C. W.; Knudson, S. E.; Liu, N.; Childs, J.; Sullivan, T. J.; Boyne, M.; Xu, H.; Gegina, Y.; Knudson, D. L.; Johnson, F.; Peloquin, C. A.; Slayden, R. A.; Tonge, P. J.: Synthesis and in vitro anti-mycobacterial activity of B-ring modified diaryl ether InhA inhibitors. *Bioorg. Med. Chem. Lett.* **2008**, *18*, 3029-33.

(142) Lu, H.; Tonge, P. J.: Inhibitors of FabI, an Enzyme Drug Target in the Bacterial Fatty Acid Biosynthesis Pathway. *Acc. Chem. Res.* **2008**, *41*, 11-20.

(143) Xu, H.; Sullivan, T. J.; Sekiguchi, J.; Kirikae, T.; Ojima, I.; Stratton, C. F.; Mao, W.; Rock, F. L.; Alley, M. R.; Johnson, F.; Walker, S. G.; Tonge, P. J.: Mechanism and inhibition of saFabI, the enoyl reductase from Staphylococcus aureus. *Biochemistry* **2008**, *47*, 4228-4236.

(144) Lu, H.; England, K.; am Ende, C.; Truglio, J. J.; Luckner, S.; Reddy, B. G.; Marlenee, N. L.; Knudson, S. E.; Knudson, D. L.; Bowen, R. A.; Kisker, C.; Slayden, R. A.; Tonge, P. J.: Slow-onset inhibition of the FabI enoyl reductase from francisella tularensis: residence time and in vivo activity. *ACS Chem. Biol.* **2009**, *4*, 221-231.

(145) Sullivan, T. J.; Truglio, J. J.; Boyne, M. E.; Novichenok, P.; Zhang, X.; Stratton, C. F.; Li, H. J.; Kaur, T.; Amin, A.; Johnson, F.; Slayden, R. A.; Kisker, C.; Tonge, P. J.: High affinity InhA inhibitors with activity against drug-resistant strains of Mycobacterium tuberculosis. *ACS Chem. Biol.* **2006**, *1*, 43-53.

(146) Hodgson, H. H.: The Sandmeyer reaction. *Chem. Rev.* **1947**, *40*, 251-277.

(147) Pfausler, B.; Haring, H. P.; Kampfl, A.; Wissel, J.; Schober, M.; Schmutzhard, E.: Cerebrospinal fluid (CSF) pharmacokinetics of intraventricular vancomycin in patients with staphylococcal ventriculitis associated with external CSF drainage. *Clin. Infect. Dis.* **1997**, *25*, 733-735.

(148) Ricard, J. D.; Wolff, M.; Lacherade, J. C.; Mourvillier, B.; Hidri, N.; Barnaud, G.; Chevrel, G.; Bouadma, L.; Dreyfuss, D.: Levels of vancomycin in cerebrospinal fluid of adult patients receiving adjunctive corticosteroids to treat pneumococcal meningitis: a prospective multicenter observational study. *Clin. Infect. Dis.* **2007**, *44*, 250-255.

(149) Albanese, J.; Leone, M.; Bruguerolle, B.; Ayem, M. L.; Lacarelle, B.; Martin, C.: Cerebrospinal fluid penetration and pharmacokinetics of vancomycin administered by continuous infusion to mechanically ventilated patients in an intensive care unit. *Antimicrob. Agents Chemother.* **2000**, *44*, 1356-1358.

(150) Estes, K. S.; Derendorf, H.: Comparison of the pharmacokinetic properties of vancomycin, linezolid, tigecyclin, and daptomycin. *Eur. J. Med. Res.* **2010**, *15*, 533-543.

(151) Di Paolo, A.; Malacarne, P.; Guidotti, E.; Danesi, R.; Del Tacca, M.: Pharmacological issues of linezolid: an updated critical review. *Clin. Pharmacokinet.* **2010**, *49*, 439-447.

(152) England, K.; am Ende, C.; Lu, H.; Sullivan, T. J.; Marlenee, N. L.; Bowen, R. A.; Knudson, S. E.; Knudson, D. L.; Tonge, P. J.; Slayden, R. A.: Substituted diphenyl ethers as a broad-spectrum platform for the development of chemotherapeutics for the treatment of tularaemia. *J. Antimicrob. Chemother.* **2009**, *64*, 1052-1061.

(153) Petchmanee, T.; Ploypradith, P.; Ruchirawat, S.: Solid-supported acids for debenzylation of aryl benzyl ethers. *J. Org. Chem.* **2006**, *71*, 2892-2895.

(154) Perales, J. B.; Makino, N. F.; Van Vranken, D. L.: Convergent stereocontrol in peterson olefinations. Application to the synthesis of (+/-)-3-hydroxybakuchiol and corylifolin. *J. Org. Chem.* **2002**, *67*, 6711-6717.

(155) Agoston, G. S., Jamshed H.; Hunsucker, Kimberly A.; Treston, Anthony M.; Pribluda, Victor S.: Nonsteroidal analogs of 2-methoxyestradiol for treatment of diseases characterized by undesirable angiogenesis and proliferative activity. *PCT Int. Appl.* **2003**, *WO 2003063791 A2 20030807*.

(156) am Ende, C. W.; Knudson, S. E.; Liu, N.; Childs, J.; Sullivan, T. J.; Boyne, M.; Xu, H.; Gegina, Y.; Knudson, D. L.; Johnson, F.; Peloquin, C. A.; Slayden, R. A.; Tonge, P. J.: Synthesis and in vitro antimycobacterial activity of B-ring modified diaryl ether InhA inhibitors. *Bioorg. Med. Chem. Lett.* **2008**, *18*, 3029-3033.

(157) Pan, P.: Lead Optimization and Slow-Onset Inhibition of the Enoyl-ACP Reductase (InhA) from Mycobacterium tuberculosis *Ph.D. Dissertation, Stony Brook University* **2012**.

(158) Panizzi, P.; Nahrendorf, M.; Figueiredo, J. L.; Panizzi, J.; Marinelli, B.; Iwamoto, Y.; Keliher, E.; Maddur, A. A.; Waterman, P.; Kroh, H. K.; Leuschner, F.; Aikawa, E.; Swirski, F. K.; Pittet, M. J.; Hackeng, T. M.; Fuentes-Prior, P.; Schneewind, O.; Bock, P. E.; Weissleder, R.: In vivo detection of Staphylococcus aureus endocarditis by targeting pathogen-specific prothrombin activation. *Nat. Med.* **2011**, *17*, 1142-1146.

(159) Xiong, Y. Q.; Willard, J.; Kadurugamuwa, J. L.; Yu, J.; Francis, K. P.; Bayer, A. S.: Real-time in vivo bioluminescent imaging for evaluating the efficacy of antibiotics in a rat Staphylococcus aureus endocarditis model. *Antimicrob. Agents Chemother.* **2005**, *49*, 380-387.

(160) White, A. G.; Fu, N.; Leevy, W. M.; Lee, J. J.; Blasco, M. A.; Smith, B. D.: Optical imaging of bacterial infection in living mice using deep-red fluorescent squaraine rotaxane probes. *Bioconjug. Chem.* **2010**, *21*, 1297-1304.

(161) Halaweish, I.; Harth, K.; Broome, A. M.; Voskerician, G.; Jacobs, M. R.; Rosen, M. J.: Novel in vitro model for assessing susceptibility of synthetic hernia repair meshes to Staphylococcus aureus infection using green fluorescent protein-labeled bacteria and modern imaging techniques. *Surg. Infect. (Larchmt)* **2010**, *11*, 449-454.

(162) Leevy, W. M.; Gammon, S. T.; Johnson, J. R.; Lampkins, A. J.; Jiang, H.; Marquez, M.; Piwnica-Worms, D.; Suckow, M. A.; Smith, B. D.: Noninvasive optical imaging of staphylococcus aureus bacterial infection in living mice using a Bis-dipicolylamine-Zinc(II) affinity group conjugated to a near-infrared fluorophore. *Bioconjug. Chem.* **2008**, *19*, 686-692.

(163) Hertlein, T.; Sturm, V.; Kircher, S.; Basse-Lusebrink, T.; Haddad, D.; Ohlsen, K.; Jakob, P.: Visualization of abscess formation in a murine thigh infection model of Staphylococcus aureus by 19F-magnetic resonance imaging (MRI). *PloS one* **2011**, *6*, e18246.

(164) Browne, L. P.; Guillerman, R. P.; Orth, R. C.; Patel, J.; Mason, E. O.; Kaplan, S. L.: Community-acquired staphylococcal musculoskeletal infection in infants and young children: necessity of contrast-enhanced MRI for the diagnosis of growth cartilage involvement. *AJR. American journal of roentgenology* **2012**, *198*, 194-199.

(165) Kumar, V.; Boddeti, D. K.; Evans, S. G.; Roesch, F.; Howman-Giles, R.: Potential use of 68Ga-apo-transferrin as a PET imaging agent for detecting Staphylococcus aureus infection. *Nucl. Med. Biol.* **2011**, *38*, 393-398.

(166) Erba, P. A.; Cataldi, A. G.; Tascini, C.; Leonildi, A.; Manfredi, C.; Mariani, G.; Lazzeri, E.: 111In-DTPA-Biotin uptake by Staphylococcus aureus. *Nucl. Med. Commun.* **2010**, *31*, 994-997.

(167) Brouwer, C. P.; Gemmel, F. F.; Welling, M. M.: Evaluation of 99mTc-UBI 29-41 scintigraphy for specific detection of experimental multidrug-resistant Staphylococcus aureus bacterial endocarditis. *Q. J. Nucl. Med. Mol. Imaging* **2010**, *54*, 442-450.

(168) Wong, D. W.; Dhawan, V. K.; Tanaka, T.; Mishkin, F. S.; Reese, I. C.; Thadepalli, H.: Imaging endocarditis with Tc-99m-labeled antibody--an experimental study: concise communication. *J. Nucl. Med.* **1982**, *23*, 229-234.

(169) Lu, H.; Tonge, P. J.: Drug-target residence time: critical information for lead optimization. *Curr. Opin. Chem. Biol.* **2010**, *14*, 467-474.

(170) Leevy, W. M.; Gammon, S. T.; Jiang, H.; Johnson, J. R.; Maxwell, D. J.; Jackson, E. N.; Marquez, M.; Piwnica-Worms, D.; Smith, B. D.: Optical imaging of bacterial infection in living mice using a fluorescent near-infrared molecular probe. *J. Am. Chem. Soc.* **2006**, *128*, 16476-16477.

(171) Piper, C.; Casey, P. G.; Hill, C.; Cotter, P. D.; Ross, R. P.: The Lantibiotic Lacticin 3147 Prevents Systemic Spread of Staphylococcus aureus in a Murine Infection Model. *Int. J. Microbiol.* **2012**, *2012*, 806230.

(172) Barnes, P. F.: Rapid diagnostic tests for tuberculosis: progress but no gold standard. *Am. J. Respir. Crit. Care Med.* **1997**, *155*, 1497-8.

(173) Nash, D. R.; Douglass, J. E.: Anergy in active pulmonary tuberculosis. A comparison between positive and negative reactors and an evaluation of 5 TU and 250 TU skin test doses. *Chest* **1980**, *77*, 32-7.

(174) Davis, S. L.; Nuermberger, E. L.; Um, P. K.; Vidal, C.; Jedynak, B.; Pomper, M. G.; Bishai, W. R.; Jain, S. K.: Noninvasive pulmonary [18F]-2-fluoro-deoxy-D-glucose positron emission tomography correlates with bactericidal activity of tuberculosis drug treatment. *Antimicrob. Agents Chemother.* **2009**, *53*, 4879-84.

(175) Ataergin, S.; Arslan, N.; Ozet, A.; Ozguven, M. A.: Abnormal FDG uptake on 18F-fluorodeoxyglucose positron emission tomography in patients with cancer diagnosis: case reports of tuberculous lymphadenitis. *Intern. Med.* **2009**, *48*, 115-9.

(176) Davis, S. L.; Be, N. A.; Lamichhane, G.; Nimmagadda, S.; Pomper, M. G.; Bishai, W. R.; Jain, S. K.: Bacterial thymidine kinase as a non-invasive imaging reporter for Mycobacterium tuberculosis in live animals. *PloS one* **2009**, *4*, e6297.

(177) Zhang, T.; Li, S. Y.; Nuermberger, E. L.: Autoluminescent Mycobacterium tuberculosis for rapid, real-time, non-invasive assessment of drug and vaccine efficacy. *PloS one* **2012**, *7*, e29774.

(178) Kong, Y.; Yao, H.; Ren, H.; Subbian, S.; Cirillo, S. L.; Sacchettini, J. C.; Rao, J.; Cirillo, J. D.: Imaging tuberculosis with endogenous beta-lactamase reporter enzyme fluorescence in live mice. *Proc. Natl. Acad. Sci. U. S. A.* **2010**, *107*, 12239-12244.

(179) Kong, Y.; Cirillo, J. D.: Reporter enzyme fluorescence (REF) imaging and quantification of tuberculosis in live animals. *Virulence* **2010**, *1*, 558-562.

(180) Bernstein, J.; Lott, W. A.; Steinberg, B. A.; Yale, H. L.: Chemotherapy of experimental tuberculosis. V. Isonicotinic acid hydrazide (nydrazid) and related compounds. *Am. Rev. Tuberc.* **1952**, *65*, 357-364.

(181) Musser, J. M.; Kapur, V.; Williams, D. L.; Kreiswirth, B. N.; van Soolingen, D.; van Embden, J. D.: Characterization of the catalase-peroxidase gene (katG) and inhA locus in

isoniazid-resistant and -susceptible strains of Mycobacterium tuberculosis by automated DNA sequencing: restricted array of mutations associated with drug resistance. *J. Infect. Dis.* **1996**, *173*, 196-202.

(182) Argyrou, A.; Vetting, M. W.; Aladegbami, B.; Blanchard, J. S.: Mycobacterium tuberculosis dihydrofolate reductase is a target for isoniazid. *Nat. Struct. Mol. Biol.* **2006**, *13*, 408-413.

(183) Banerjee, A.; Dubnau, E.; Quemard, A.; Balasubramanian, V.; Um, K. S.; Wilson, T.; Collins, D.; de Lisle, G.; Jacobs, W. R., Jr.: inhA, a gene encoding a target for isoniazid and ethionamide in Mycobacterium tuberculosis. *Science* **1994**, *263*, 227-230.

(184) Dessen, A.; Quemard, A.; Blanchard, J. S.; Jacobs, W. R., Jr.; Sacchettini, J. C.: Crystal structure and function of the isoniazid target of Mycobacterium tuberculosis. *Science* **1995**, *267*, 1638-1641.

(185) Mdluli, K.; Slayden, R. A.; Zhu, Y.; Ramaswamy, S.; Pan, X.; Mead, D.; Crane, D. D.; Musser, J. M.; Barry, C. E., 3rd: Inhibition of a Mycobacterium tuberculosis beta-ketoacyl ACP synthase by isoniazid. *Science* **1998**, *280*, 1607-1610.

(186) Seydel, J. K.; Schaper, K. J.; Wempe, E.; Cordes, H. P.: Mode of action and quantitative structure-activity correlations of tuberculostatic drugs of the isonicotinic acid hydrazide type. *J. Med. Chem.* **1976**, *19*, 483-492.

(187) Amartey, J. K.; Esguerra, C.; Al-Otaibi, B.; Parhar, R. S.; Al-Jammaz, I.: 2-[(18)F]-fluoroisonicotinic acid hydrazide: biological evaluation in an acute infection model. *Appl. Radiat. Isot.* **2004**, *60*, 839-843.

(188) Amartey, J. K.; Al-Jammaz, I.; Al-Otaibi, B.; Esguerra, C.: Novel synthesis of 2-[18F]-fluoroisonicotinic acid hydrazide and initial biological evaluation. *Nucl. Med. Biol.* **2002**, *29*, 817-823.

(189) Bardou, F.; Raynaud, C.; Ramos, C.; Laneelle, M. A.; Laneelle, G.: Mechanism of isoniazid uptake in Mycobacterium tuberculosis. *Microbiology* **1998**, *144 (Pt 9)*, 2539-2544.

(190) Rouse, D. A.; DeVito, J. A.; Li, Z.; Byer, H.; Morris, S. L.: Site-directed mutagenesis of the katG gene of Mycobacterium tuberculosis: effects on catalase-peroxidase activities and isoniazid resistance. *Mol Microbiol* **1996**, *22*, 583-92.

(191) Musser, J. M.; Kapur, V.; Williams, D. L.; Kreiswirth, B. N.; van Soolingen, D.; van Embden, J. D.: Characterization of the catalase-peroxidase gene (katG) and inhA locus in isoniazid-resistant and -susceptible strains of Mycobacterium tuberculosis by automated DNA sequencing: restricted array of mutations associated with drug resistance. *J Infect Dis* **1996**, *173*, 196-202.

(192) Almeida, D.; Nuermberger, E.; Tasneen, R.; Rosenthal, I.; Tyagi, S.; Williams, K.; Peloquin, C.; Grosset, J.: Paradoxical effect of isoniazid on the activity of rifampin-pyrazinamide combination in a mouse model of tuberculosis. *Antimicrob Agents Chemother* **2009**, *53*, 4178-84.

(193) Zhao, X.; Yu, H.; Yu, S.; Wang, F.; Sacchettini, J. C.; Magliozzo, R. S.: Hydrogen peroxide-mediated isoniazid activation catalyzed by Mycobacterium tuberculosis catalase-peroxidase (KatG) and its S315T mutant. *Biochemistry* **2006**, *45*, 4131-4140.

(194) Davis, S. L.; Nuermberger, E. L.; Um, P. K.; Vidal, C.; Jedynak, B.; Pomper, M. G.; Bishai, W. R.; Jain, S. K.: Noninvasive pulmonary [18F]-2-fluoro-deoxy-D-glucose positron emission tomography correlates with bactericidal activity of tuberculosis drug treatment. *Antimicrob Agents Chemother* **2009**, *53*, 4879-84.

(195) Nguyen, M.; Quemard, A.; Broussy, S.; Bernadou, J.; Meunier, B.: Mn(III) pyrophosphate as an efficient tool for studying the mode of action of isoniazid on the InhA protein of Mycobacterium tuberculosis. *Antimicrob Agents Chemother* **2002**, *46*, 2137-44.

(196) Wright, A.; Zignol, M.; Van Deun, A.; Falzon, D.; Gerdes, S. R.; Feldman, K.; Hoffner, S.; Drobniewski, F.; Barrera, L.; van Soolingen, D.; Boulabhal, F.; Paramasivan, C. N.; Kam, K. M.; Mitarai, S.; Nunn, P.; Raviglione, M.: Epidemiology of antituberculosis drug resistance 2002-07: an updated analysis of the Global Project on Anti-Tuberculosis Drug Resistance Surveillance. *Lancet* **2009**, *373*, 1861-73.

(197) Dye, C.; Williams, B. G.: Eliminating human tuberculosis in the twenty-first century. *J R Soc Interface* **2008**, *5*, 653-62.

(198) Emergence of Mycobacterium tuberculosis with extensive resistance to second-line drugs--worldwide, 2000-2004. *MMWR Morb Mortal Wkly Rep* **2006**, *55*, 301-5.

(199) Schluger, N. W.: Tuberculosis Clinical Trials: Past, Present and Future. In *Tuberculosis: From Lab Research to Field Trials*; Kaufmann, S. H., Smith, I., Nathan, C. F., Eds.; Keystone Symposia: Vancouver, Brisitsh Columbia, Canada, 2007.

(200) Signore, A.; Glaudemans, A. W.: The molecular imaging approach to image infections and inflammation by nuclear medicine techniques. *Ann Nucl Med* **2011**, *25*, 681-700.

(201) Sato, T.; Ashizawa, N.; Matsumoto, K.; Iwanaga, T.; Nakamura, H.; Inoue, T.; Nagata, O.: Discovery of 3-(2-cyano-4-pyridyl)-5-(4-pyridyl)-1,2,4-triazole, FYX-051 - a xanthine oxidoreductase inhibitor for the treatment of hyperuricemia [corrected]. *Bioorg. Med. Chem. Lett.* **2009**, *19*, 6225-6229.

(202) Luckner, S. R.; Liu, N.; am Ende, C. W.; Tonge, P. J.; Kisker, C.: A slow, tight binding inhibitor of InhA, the enoyl-acyl carrier protein reductase from Mycobacterium tuberculosis. *J Biol Chem* **2010**, *285*, 14330-7.

(203) Parikh, S.; Moynihan, D. P.; Xiao, G.; Tonge, P. J.: Roles of tyrosine 158 and lysine 165 in the catalytic mechanism of InhA, the enoyl-ACP reductase from Mycobacterium tuberculosis. *Biochemistry* **1999**, *38*, 13623-34.